UNIVERSITÀ DI PARMA

UNIVERSITÀ DEGLI STUDI DI PARMA

Dottorato di Ricerca in Tecnologie dell'Informazione

XXXVII Ciclo

Self-Commissioning and Estimation Techniques for Sustainable Synchronous Reluctance Motor Drives in Industrial Applications

Coordinatore:

Chiar.mo Prof. Marco Locatelli

Tutor:

Chiar.mo Prof. Alessandro Soldati

Dottorando: *Hossein SadeghLafmejani*

2022/2025

To my wife and family,
for your
love, support, and inspiration

Abstract

The global push for sustainable and energy-efficient industrial practices has necessitated advancements in electric motor drive systems. This thesis focuses on the development of self-commissioning and estimation techniques for Synchronous Reluctance Motors (SynRM), a promising alternative to traditional Induction Motors (IM) and Permanent Magnet Synchronous Motors (PMSM). SynRMs are gaining significant attention due to their high efficiency, cost-effectiveness, and lack of reliance on rare-earth materials, making them a sustainable choice for industrial applications.

This research introduces robust self-commissioning algorithms for three-phase two-level inverters and SynRMs. These algorithms effectively address critical challenges such as inverter nonlinearity, dead-time effects, voltage drop compensation, and parameter estimation. One notable contribution of this research is development of a Phase-Locked Loop (PLL)-based observer, which enables accurate rotor position and flux estimation for sensor-less control. This eliminates the need for costly mechanical sensors while maintaining system reliability and precision.

The proposed self-commissioning methods simplify the initial setup of SynRM drives, enabling a plug-and-play operation. Experimental validations and simulations have demonstrated significant improvements in motor control performance, energy efficiency, and overall system robustness. By mitigating the effects of inverter nonlinearities and accurately identifying motor parameters at standstill, the developed methods provide a reliable solution for industrial applications.

The contributions of this work are significant for industries seeking greener, energy-efficient alternatives to traditional IMs and PMSMs without compromising performance. The findings highlight the potential of SynRM drives to replace IMs and PMSMs in various applications, such as HVAC systems, pumps, and renewable energy systems. This research lays a solid foundation for future advancements, including integrating advanced control strategies, optimizing motor designs, and expanding the use of SynRM technology in high-power and renewable energy applications.

Keywords: Energy efficiency, Industrial applications, Inverter nonlinearity, Phase-locked loop observer, Self-commissioning, Sensor-less control, Synchronous reluctance motor.

Contents

List of Figures

List of Tables

Chapter 1

Introduction

1.1 Role of Electric Machines in Sustainability

Electric machines are the backbone of industrial automation, responsible for driving a wide range of machinery in manufacturing, transportation, and energy sectors. Their widespread usage accounts for approximately 45% of global electricity consumption, making them a prime target for efficiency improvements in efforts toward sustainability [1]. While current industrial motor drives have achieved significant efficiency improvements, further advancements could lead to even greater reductions in energy use and greenhouse gas emissions, particularly in high-demand applications. As industries strive to meet environmental regulations, the adoption of energy-efficient motor drives is critical for achieving sustainability goals.

AC electric machines, particularly three-phase machines, have been fundamental to industrial applications due to their robustness, reliability, and scalability [2, 3]. However, the efficiency of conventional AC machines, such as induction motors (IMs), can be relatively low compared to modern high-efficiency motor technologies, especially under partial load conditions in variable-load applications like pumps, fans, and conveyors. In this context, enhancing motor efficiency directly contributes to sustainability by reducing both energy consumption and carbon emissions [1, 4].

Different motor types offer varying degrees of efficiency and cost-effectiveness.

IMs are widely used but suffer from rotor losses, and lower efficiency compared to synchronous machines. These rotor losses are primarily due to induced currents in the rotor, which generate additional heat, reducing overall motor efficiency, especially at light loads. In contrast, synchronous machines reduce rotor losses during steady-state operation, which helps improve both efficiency and thermal performance. However, some losses can still arise during dynamic conditions. [5].

Permanent Magnet Synchronous Motors (PMSMs) are widely recognized for their high efficiency and power density, owing to the use of rare-earth magnets. These machines are particularly well-suited for high-performance applications, such as electric vehicles and industrial drives [6]. However, the reliance on rare-earth materials poses challenges related to cost and sustainability, prompting the exploration of alternative motor technologies [7].

Switched Reluctance Motors (SRMs) are cost-effective but suffer from torque ripple and complex control requirements [8]. In contrast, Synchronous Reluctance Motors (SynRMs) have emerged as a highly efficient and sustainable alternative, offering excellent performance without the need for expensive materials like rare-earth magnets.

1.2 Synchronous Reluctance Motors: A Sustainable Choice

SynRMs provide a compelling alternative to both IMs and PMSMs due to their unique design. As shown in Table 1.1, from a sustainability perspective, SynRMs offer several advantages over IMs and PMSMs [5, 9, 10, 11]. SynRMs do not rely on rare-earth materials, unlike PMSMs, which reduces the environmental impact associated with the extraction and processing of these scarce resources [11]. Additionally, SynRMs demonstrate high efficiency, especially at partial loads, which can significantly reduce energy consumption in industrial applications such as fans, pumps, and HVAC (Heating, Ventilation, and Air Conditioning) systems. This energy efficiency directly supports sustainability goals by lowering operational carbon footprints. Compared to IMs, which experience efficiency drops under partial loads and require more maintenance, SynRMs are more durable as well, reducing the need for frequent re-

placements and the associated environmental costs [12, 13]. Moreover, they operate without the use of magnets or rotor windings, eliminating rotor losses and reducing thermal issues. This design results in highly efficient machines with a lower cost of production and maintenance, making them more economically viable for widespread adoption [8, 14]. These factors make SynRMs a compelling choice for industries focused on sustainability and energy efficiency.

Table 1.1: Comparison of key characteristics among SynRM, IM, and PMSM

Feature	SynRM	IM	PMSM
Efficiency	High	Moderate	Very high
Torque Density	Moderate	Moderate	High
Cost	Low	Moderate	High
Relative Control Complexity (Application-Dependent)	High	Simple	High
Material	No rare earth magnets	Copper/Iron	Rare-earth magnets
Applications	HVAC, Pumps, Fans	Industrial, Pumps, Fans	EVs, Robotics

1.3 Problem Description and Motivation

The efficiency and performance of AC motors depend not only on the motor design but also on the precision of the drive algorithm and control system. Following the discussions in previous sections and according to Table 1.1, to replace general-purpose IMs and PMSMs with SynRMs in different industrial applications, the drive system must be highly efficient, cost-competitive, and sensorless. Achieving this requires a comprehensive machine model that accounts for factors such as magnetic saturation and parameter variation. In industrial environments, ease of deployment is a critical factor. To facilitate the adoption of SynRMs, a self-commissioning mechanism

is essential. Self-commissioning algorithms allow the motor and drive to calibrate themselves during the initial setup, reducing the need for manual intervention and enabling plug-and-play functionality.

Additionally, modern drives, particularly three-phase, two-level voltage source inverters, introduce nonlinearities due to various factors, such as the dead-time effect and switching device characteristics. These nonlinearities can distort the output voltage, leading to performance degradation, torque ripple, and an increase in energy losses [15]. Therefore, modeling and self-commissioning of these nonlinearities are crucial for effective compensation and for achieving accurate machine identification and control performance, especially in high-precision applications.

Another important aspect of the self-commissioning phase of the machine and inverter is the status of the rotor shaft during the procedure. In most applications, the rotor shaft is already connected to a mechanical load. While identifying motor parameters with a rotating rotor may yield accurate results and can serve as a reference method, it may also introduce risks, including potential mechanical damage due to unknown conditions [16, 17, 18]. Moreover, it requires an appropriate test setup. Therefore, there is a necessity for a parameter identification method at a standstill rotor condition. One possible solution is to mechanically lock the rotor; however, this requires external fixtures or equipment [19]. An alternative approach would be to perform parameter identification in a free standstill rotor condition, which represents the most challenging scenario in the self-commissioning process.

The next step is the concern of sensorless closed-loop control for the machine. Sensorless control relies on a highly accurate and fast position/speed observer, which eliminates the need for costly sensors, such as encoders and resolvers, thereby reducing system cost and complexity. This approach also enhances reliability in challenging environmental conditions.

1.4 Objectives

To replace general-purpose IM and PMSM drives in practical applications, the control and drive system of SynRMs must be enhanced. Thus, transitioning from a con-

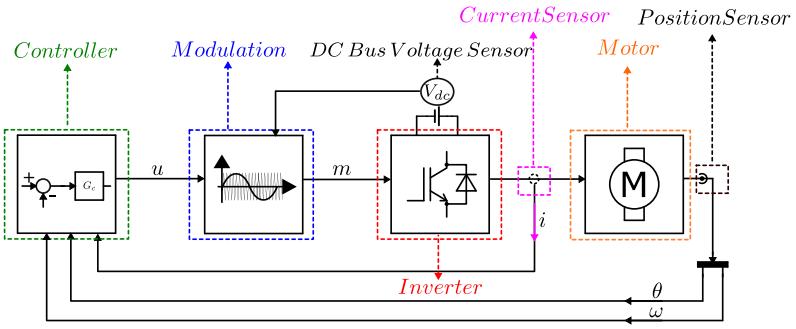

Figure 1.1: A typical inverter fed AC machine drive.

ventional control and drive system to an enhanced smart machine drive presents a promising solution. A typical schematic for an inverter-fed control and drive system of AC machines is illustrated in Figure 1.1, which includes the controller, sensors, inverter, modulation unit, and the machine itself. The objective of this study is to contribute to the development of a simple and accurate method for identifying inverter nonlinearity and self-commissioning the SynRM model at standstill, without measuring the actual inverter output voltage. Instead, it uses an estimated look-up table of voltage drops, which removes the need for voltage sensors, a key advantage over other the available methods like TI's InstaSPIN design [20] that rely on voltage measurements. Moreover, a fast dynamic Phase-Locked Loop (PLL)-based position and speed observer is proposed for sensorless operation of the machine. Utilizing the model extracted during the identification phase and applying the proposed observer can enable optimal closed-loop control of the machine. These procedures enable plug-and-play functionality, which is highly desirable in industrial applications. The general schematic of the proposed smart drive for the SynRM is shown in Figure 1.2. In this diagram, the red dashed-line paths are active only during the self-commissioning phase, while the green solid-line paths are enabled during the control phase.

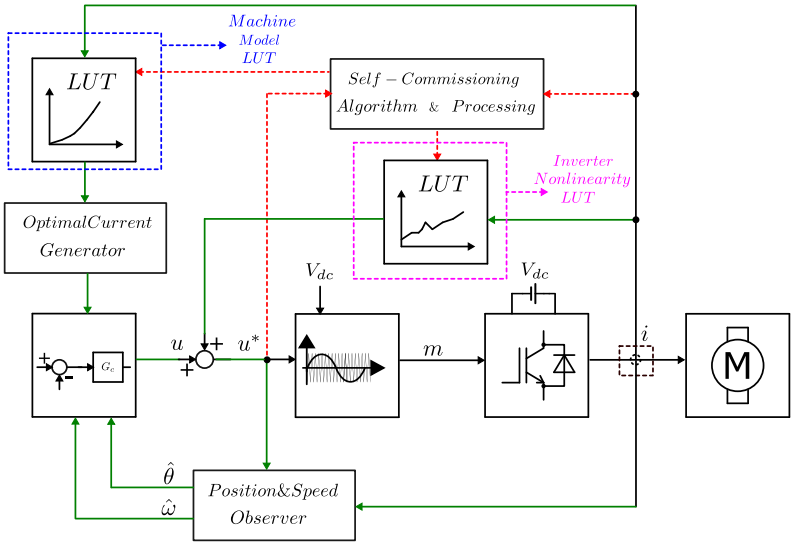

Figure 1.2: Topology of the proposed SynRM smart drive. The phase current and DC bus voltage sensors are the only measurement component used in the drive.

1.5 Overview of the Thesis

The thesis is organized as follows:

Chapter 2 provides an overview of the current methods for modeling and self-commissioning of the three-phase two-level inverter, which is the main machine driver in this project. It begins with a review of the sine pulse-width modulation (SPWM) method and its role in inverter control. The chapter then reviews how to model and analyze the inverter, considering different sources of voltage distortion, and presents a model which describes the nonlinear behavior of the system. A modified version of the typical inverter nonlinearity self-commissioning method is proposed, and its performance is investigated through experimental testing. The equivalent parameters of the inverter are estimated using an optimal model fitting process and compared with available values from the datasheet and measurements.

Chapter 3 begins with an overview of the current techniques used for modeling and self-commissioning of synchronous reluctance machines, highlighting re-

cent advancements in the field. It then presents the mathematical modeling of the synchronous reluctance motor. Following this, simulations of some existing self-commissioning methods are performed. The chapter concludes by proposing a new self-commissioning method, comparing the simulation results with the established methods to demonstrate the correctness, improvements, and advantages of the new approach. Finally, the proposed method is implemented in an experimental setup to investigate its performance in a real environment.

Chapter 4 examines the current methods for designing observers used in sensorless control of synchronous reluctance motors. It begins with an overview of existing techniques to provide a better understanding of how sensorless control works. The chapter then explains the PLL-based flux and back electromotive force (EMF) observer using mathematical models. Next, a new fast dynamic PLL observer is introduced. Finally, the chapter presents simulation and experimental implementation results of the new observer, evaluating its performance in accurately tracking rotor position and speed.

The last chapter summarizes the key findings and contributions of the research. It reviews the development and implementation of the proposed self-commissioning method and the designed PLL-based observer, highlighting their effectiveness in improving the performance of the synchronous reluctance motor. The chapter also analyzes the results of the experimental validations and simulations, emphasizing how the proposed methods provide better performance than existing techniques in terms of accuracy. Finally, it discusses the potential applications of the research and proposes future research directions for continued advancement in the field.

Chapter 2

Three-Phase Two-Level Inverter Self-Commissioning

2.1 State of the Art

Numerous papers have extensively studied inverter modeling and analysis, focusing on describing and compensating for the difference between the commanded and actual output voltage [21, 22, 23, 24, 25, 26, 27].

Inverter nonlinearity and the resulting voltage errors are among the prominent challenges in achieving precise control of AC machine drives, including SynRMs. Various modeling and compensation techniques have been proposed to address these nonlinearities. A notable approach is the development of error compensation models based on least-squares estimation, as discussed in [28], which proposes a nonlinear voltage error model to account for voltage drops in voltage source inverters (VSIs). Similarly, advanced compensation methods, including dead-time elimination and high-frequency switching adjustments, have been explored to improve accuracy in PMSM drive systems [29].

For three-level inverters, the use of resonant controllers has been shown to effectively mitigate voltage distortion by addressing harmonic content and reducing even-order harmonics, especially in systems that require low current distortion [30, 15].

However, since resonant controllers are primarily designed for steady-state operation, their performance may be less effective during transient conditions. Some researchers have also integrated fixed-time adaptive laws into super-twisting resonant controllers, which allow for dynamic adjustments to inverter nonlinearity under changing load conditions [31]. In [32], the authors present an alternative self-commissioning algorithm suitable for synchronous reluctance drives, using self-tuning techniques to compensate for nonlinearities caused by dead-time effects.

The self-commissioning approach has gained considerable attention, as seen in [33], where multiple linear regression methods based on physical models are employed to estimate parameters of the nonlinear system without the need for additional sensors. This strategy has been applied to both PMSMs and IMs [34, 35]. In high-performance motor drive applications, a repetitive control-based self-commissioning procedure is proposed to continuously adapt the inverter model to account for voltage errors at different operating points [36].

Another innovative solution includes the use of lookup tables (LUTs) for real-time error compensation, especially in systems with significant DC-link voltage variations [37]. Additionally, numerical fitting-based approaches have shown effectiveness in interior PMSM drives, providing accurate torque estimation by correction for inverter-induced voltage errors [38]. Meanwhile, Shang et al. introduce a dual-three-phase PMSM drive compensation method that utilizes current injection to identify inverter nonlinearities, taking into account the impact of zero-axis voltage [39].

Finally, some studies incorporate advanced self-learning algorithms and artificial neural networks (ANNs) to model and compensate the inverter nonlinearities in a data-driven manner [40]. These approaches are particularly better in applications requiring high-precision control, such as those utilizing IPMSMs and multilevel cascaded H-bridge inverters [41, 15]. Overall, these studies emphasize the effectiveness of various modeling and compensation techniques for enhancing the accuracy and robustness of the inverter-fed motor systems, each method offering unique benefits depending on the system requirements and implementation complexity.

2.2 Three-Phase Two-Level Inverter

The typical three-phase, two-level inverter is illustrated in Figure 2.1. It is a power conversion device designed to generate a three-phase AC voltage from a DC supply. This type of inverter is widely used in industrial applications, such as motor drives, renewable energy systems, and power distribution, due to its simplicity and cost-effectiveness.

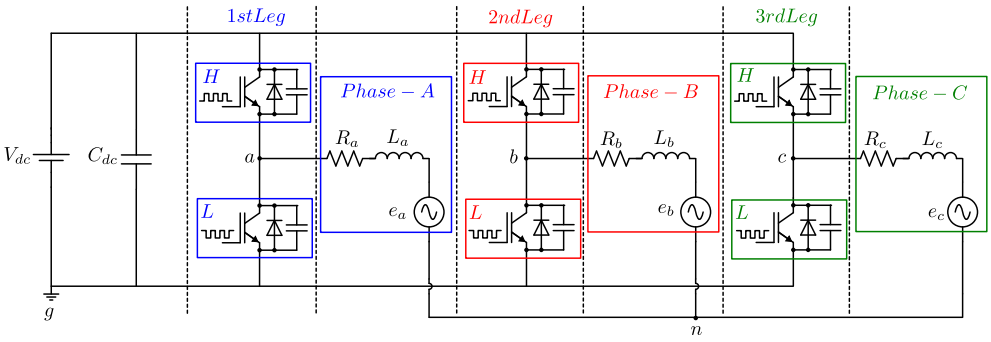

Figure 2.1: Typical schematic of a three-phase, two-level inverter.

The inverter consists of three legs, each corresponding to one phase of the output (A, B, and C). Each leg has two semiconductor switching devices: one on the high side and one on the low side. Typically, insulated-gate bipolar transistors (IGBTs) or metal-oxide-semiconductor field-effect transistors (MOSFETs) are used as switching devices. Each switch also has an associated anti-parallel diode to allow freewheeling current to flow when the switch is turned off. Additionally, each switching device has an inherent output parasitic capacitance. This capacitance plays a crucial role in switching behavior, affecting switching losses and voltage transients.

Each leg operates in a complementary switching mode as shown in Figure 2.2. This means that, when the high-side switch is on, the low-side switch is off, and conversely, when the low-side switch is on, the high-side switch is off. This ensures that the output phase voltages are either at the positive or negative DC bus voltage, creating the two-level output.

The three-phase load connected to the inverter can be inductive (L) or a combi-

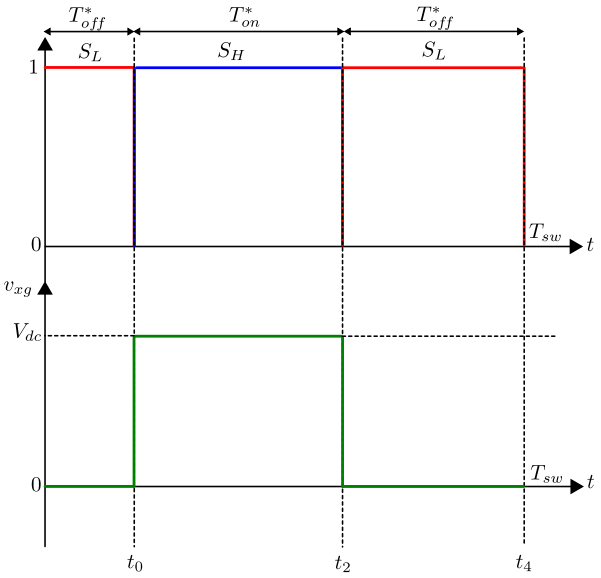

Figure 2.2: Ideal switching behavior in a two-level inverter leg.

nation of resistive and inductive (RL), such as a motor. In the case of a motor, the load introduces a back-EMF due to the rotation of the motor shaft. Depending on the operating conditions, this back-EMF can either oppose or align with the applied voltage, influencing the current flowing through each phase.

2.3 Sinusoidal Pulse-Width Modulation

The switching devices are operated using Pulse-Width Modulation (PWM), a method that adjusts the on- and off-times of the switches to approximate a sinusoidal fundamental voltage output from the DC input. In a three-phase inverter, the role of the PWM modulator is to convert the reference voltage signal, generated by the controller, into the appropriate switching commands for each individual switch in the inverter. Among the various modulation techniques, sinusoidal PWM (SPWM), often combined with third-harmonic injection, and Space Vector Modulation (SVM) are widely used strategies for two-level inverters in industrial applications. These

techniques allow for a higher modulation index, improving DC bus utilization by approximately 15%. According to Figure 2.3, SPWM operates by comparing a sinusoidal reference signal (which represents the desired output) with a high-frequency triangular carrier signal. When the reference signal is greater than the carrier signal, the corresponding high-side switch in the inverter is turned on, and when it is lower, the low-side switch is turned on. This results in a pulse-width-modulated signal where the width of the pulses corresponds to the amplitude of the sinusoidal reference signal at that moment.

2.4 Inverter Nonlinearity Modeling and Analysis

Inverter nonlinearity arises from various factors that can cause distortion in the output voltage waveform, leading to performance degradation. One major source of distortion is the dead-time, which refers to a chosen delay considered between switching transitions to prevent simultaneous conduction of both high-side and low-side devices. Although it is necessary, dead-time can result in a voltage drop and harmonic distortion in the output waveform. Additionally, the turn-on and turn-off delays of switching devices, due to their finite switching speeds, contribute to deviations from the ideal waveform.

The voltage drop across switching devices, especially during conduction, is another factor that affects the output voltage because of the real switches, such as IGBTs, exhibit a non-zero saturation voltage. Moreover, the output parasitic capacitance of switching devices causes charge storage, which influences the timing and smoothness of the switching transitions, leading to waveform distortion.

These effects create distortion and voltage drops that are particularly significant in high-performance applications requiring precise control over the output waveform. According to the ideal switching characteristic shown in Figure 2.2, the average output phase-to-ground voltage is:

$$v_{xg}^{*} = \frac{T_{on}^{*}}{T_{sw}} V_{dc} \tag{2.1}$$

This equation represents the ideal voltage v_{xg}^{*}, which serves as a reference for

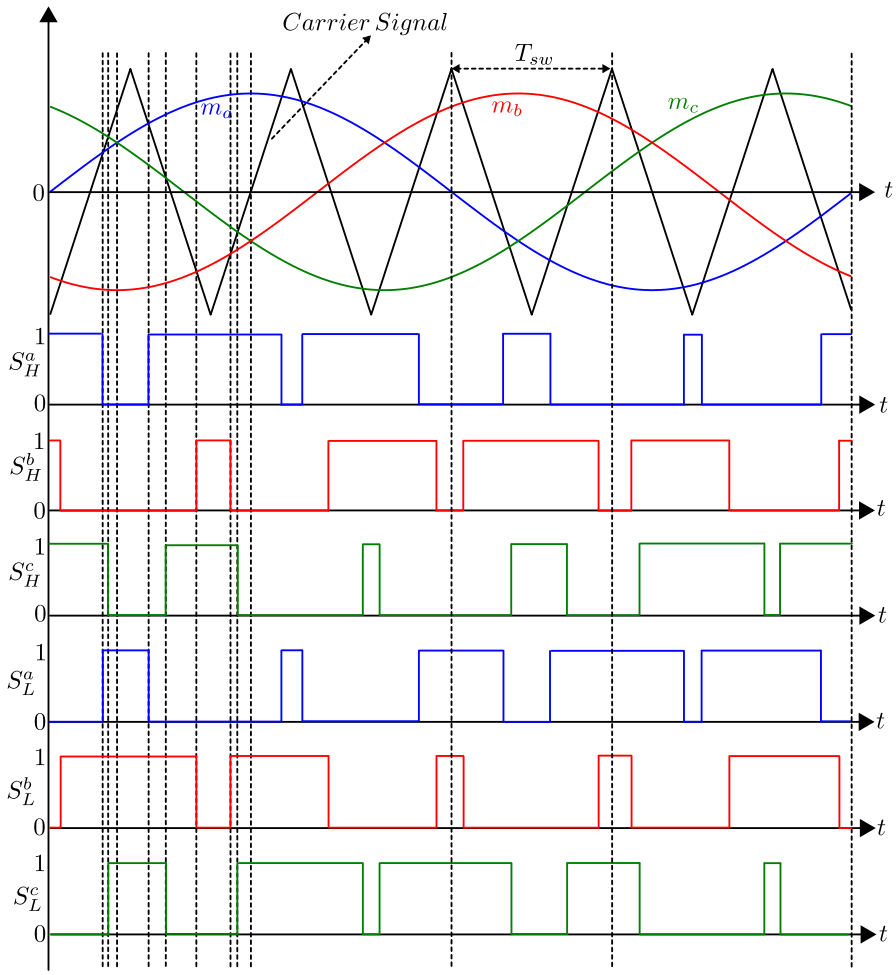

Figure 2.3: General concept of sinusoidal pulse-width modulation (SPWM).

comparison with the actual, distorted inverter output voltage. T^*_{on} is the on-time duration of the switch in one switching period T_{sw}, and V_{dc} is the inverter DC bus voltage. In the subsequent sections, the mathematical model of the output voltage of the inverter will be reviewed and analyzed by introducing various sources of voltage drops step by step. It should be noted that in this analysis, the sign of the current flowing from inverter to load is considered as positive.

2.4.1 Dead-Time Insertion

In a voltage source inverter, dead-time refers to the delay inserted between the switching events of the complementary transistors in each inverter leg to prevent short circuits, also known as "shoot-through," that could occur if both switches in a leg are turned on simultaneously. Although dead-time is necessary to protect the power devices, it also affects the output voltage of the inverter and causes distortions, especially at low voltages.

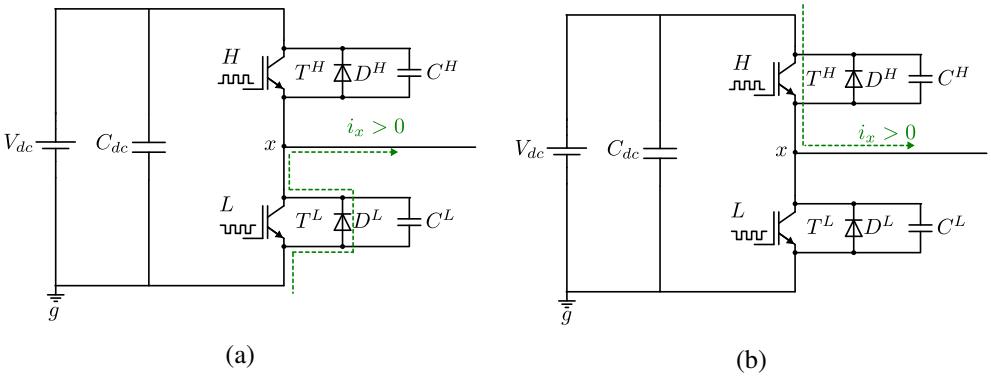

Figure 2.4: Current conduction paths for $i_x > 0$: (a) S_H*: off,* S_L*: off* or S_H*: off,* S_L*: on*, (b) S_H*: on,* S_L*: off*.

According to Figure 2.4 and Fig. 2.6a, when the current flows in the positive direction, the phase-to-ground voltage level varies between zero and the DC bus voltage depending on the conduction of the components in different states for one switching period. When the low-side switch is on and the high-side switch is off, and the current

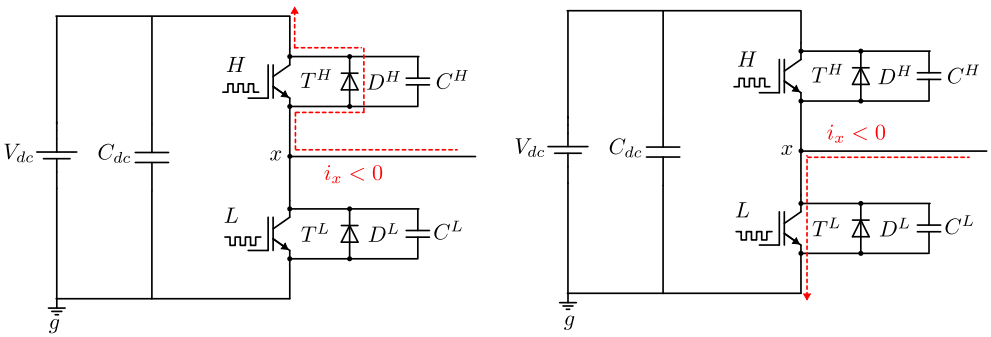

Figure 2.5: Current conduction paths for $i_x < 0$: (a) S_H*: off,* S_L*: off* or S_H*: on,* S_L*: off*, (b) S_H*: off,* S_L*: on*.

is flowing from the inverter to the load as shown in Fig. 2.4a, the low-side freewheeling diode conducts, and the output voltage of the inverter leg is near the negative DC bus voltage. Additionally, if both the low-side and high-side switches are off, meaning that the inverter is in the dead-time period t_d and the current direction is still positive, the low-side freewheeling diode will still conduct. According to Fig. 2.4b, when the high-side switch is on while the low-side switch is off, the high-side transistor will conduct and the output voltage is near the positive DC bus voltage. Therefore, the phase-to-ground average voltage in one switching cycle for positive current is:

$$v_{xg}^{+} = \frac{T_{on}^{*} - t_d}{T_{sw}} V_{dc}, \quad i_x > 0 \tag{2.2}$$

A similar analysis holds for the negative current direction, considering Figure 2.5 and Fig. 2.6b. When the low-side is on and the high-side is off, current flows through the low-side transistor, and the output voltage is near zero according to Fig. 2.5b. In the case of the low-side switch being off, regardless of whether the high-side switch is on or off, the current flows through the high-side freewheeling diode as shown in Fig. 2.5a, resulting in an output voltage near the DC bus voltage. Thus, the average phase-to-ground voltage in one switching cycle for the negative current direction is:

$$v_{xg}^{-} = \frac{T_{on}^{*} + t_d}{T_{sw}} V_{dc}, \quad i_x < 0 \tag{2.3}$$

Combining (2.2) and (2.3), using the sign function, we obtain:

$$v_{xg} = \frac{T_{on}^{*} - t_d \, sgn(i_x)}{T_{sw}} V_{dc} \tag{2.4}$$

Comparing this equation with the ideal output voltage in (2.1), the voltage drop is defined as follows:

$$\delta v_{xg} = v_{xg}^{*} - v_{xg} = \frac{t_d}{T_{sw}} V_{dc} \, sgn(i_x) \tag{2.5}$$

The voltage waveform deviation caused by dead-time is illustrated in Figure 2.6. The region highlighted in light red shows a decrease in voltage relative to the reference in one switching cycle, while the green-shaded region shows an increase in voltage relative to the reference in one switching cycle. Considering $V_{dc} = 320V$, $f_{sw} = 10kHz$, and $t_d = 2\mu s$ as the base values for analysis, Figure 2.7 shows that the voltage distortion has a directly proportional relationship with changes in these parameters.

2.4.2 Turn-on and Turn-off Delays

The turn-on and turn-off delays of switching devices in an inverter can affect the output voltage quality. These delays arise from the inherent switching characteristics of power electronic devices, such as MOSFETs or IGBTs, which take a finite amount of time to transition between the on and off states.

During the turn-on delay t_{on}, the device does not begin conducting immediately after the gate signal is applied, resulting in a temporary gap where the expected output voltage is not reached. Similarly, the turn-off delay t_{off} occurs when the device continues to conduct for a short period after the gate signal is removed, resulting in an unintended extension of the output voltage pulse. These delays can cause distortions in the output voltage waveform, particularly in high-speed switching applications, as the waveform deviates from its intended form. For analytical simplicity, a fixed delay value is assumed.

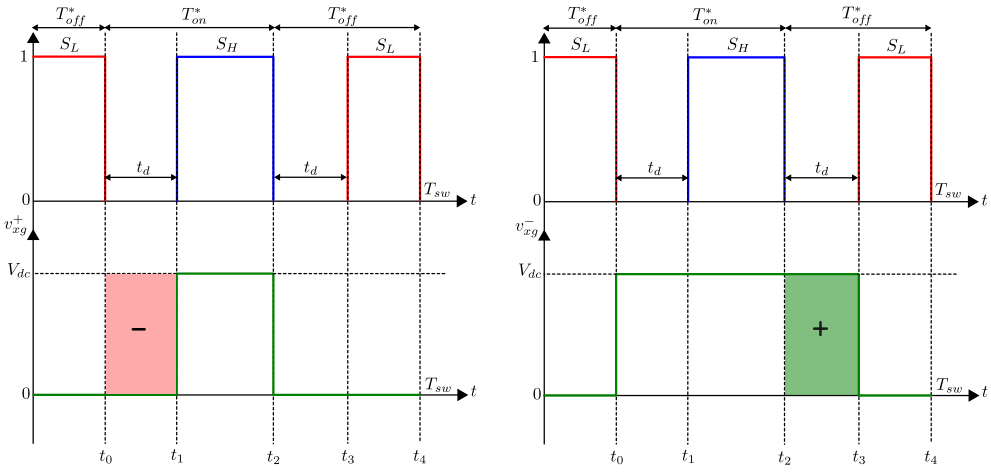

(a) (b)

Figure 2.6: Phase-to-ground output voltage of the inverter during one switching cycle, considering dead-time insertion: (a) $i_x > 0$, (b) $i_x < 0$.

According to Figure 2.4 and Figure 2.8, using the same analytical approach as in the previous section for positive and negative current flow, the average output voltages considering turn-on and turn-off delays are:

$$v^+_{xg} = \frac{T^*_{on} - t_d - (t_{on} - t_{off})}{T_{sw}} V_{dc}, \quad i_x > 0 \tag{2.6}$$

$$v^-_{xg} = \frac{T^*_{on} + t_d - (t_{on} - t_{off})}{T_{sw}} V_{dc}, \quad i_x < 0 \tag{2.7}$$

Combining (2.6) and (2.7), using the sign function, we obtain:

$$v_{xg} = \frac{T^*_{on} - t_d \; sgn(i_x) - (t_{on} - t_{off})}{T_{sw}} V_{dc} \tag{2.8}$$

Comparing this equation with the ideal output voltage in (2.1), the voltage drop is defined as follows:

$$\delta v_{xg} = v^*_{xg} - v_{xg} = \frac{t_d \; sgn(i_x) + (t_{on} - t_{off})}{T_{sw}} V_{dc} \tag{2.9}$$

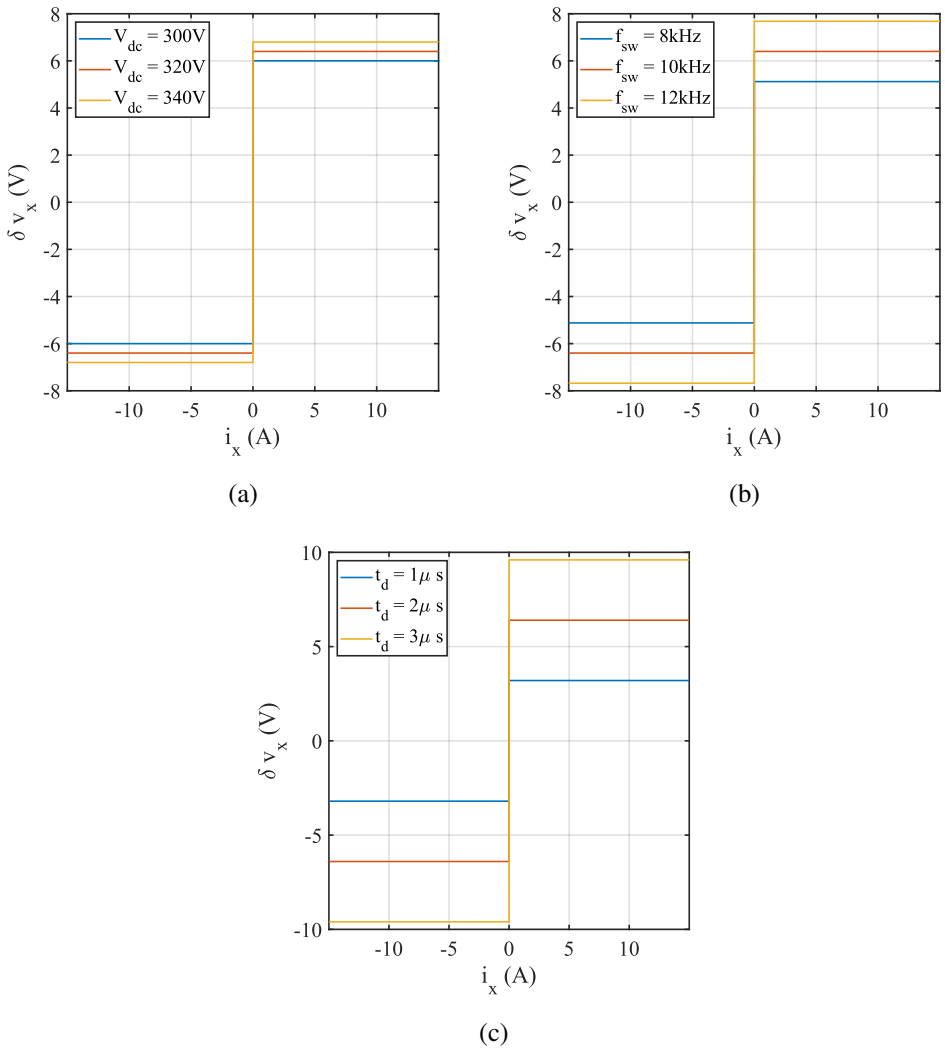

Figure 2.7: Voltage drop sensitivity due to dead-time insertion under variations in DC bus voltage, switching frequency, and dead-time duration:(a) V_{dc}, (b) f_{sw}, (b) t_d.

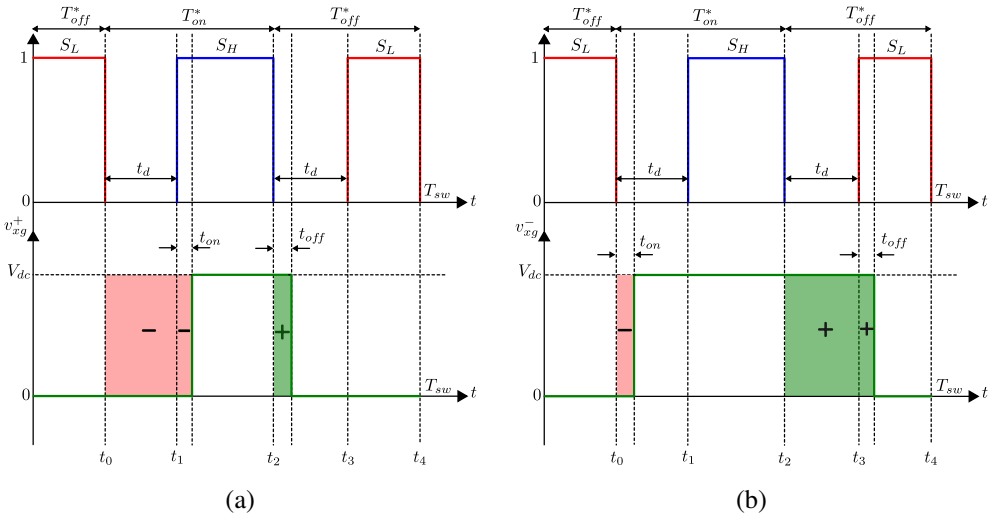

Figure 2.8: Phase-to-ground output voltage of the inverter during one switching cycle, considering dead-time insertion and switching device turn-on/off delays: (a) $i_x > 0$, (b) $i_x < 0$.

According to Figure 2.8 and Figure 2.9, turn-on and turn-off delays contribute to a shift in the average voltage, introducing asymmetry in the voltage drop model. Although these delays are independent of i_x, they introduce an imbalance between the positive and negative voltage drop regions. In a three-phase Y-connected load, this shift cancels out over a full switching cycle. However, the asymmetry persists and can impact inverter self-commissioning, affecting voltage estimation and control accuracy.

2.4.3 Switching Device Characteristic Effects

The switching devices in an inverter, including transistors and their anti-parallel diodes, exhibit specific characteristics that influence the output voltage. These devices, typically diodes, MOSFETs, and IGBTs, each have unique electrical properties that impact inverter performance. For instance, turn-on voltage $v_{on,t}$ of the transistor is the minimum voltage required to activate it and a higher value results in a

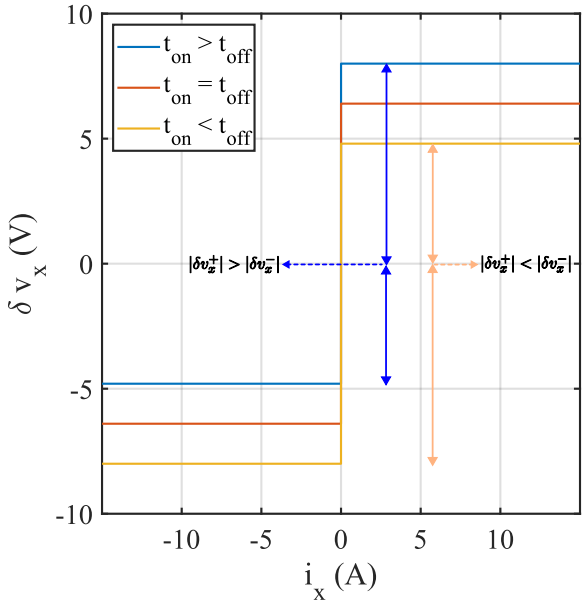

Figure 2.9: Voltage drop sensitivity due to turn-on and turn-off delay characteristics.

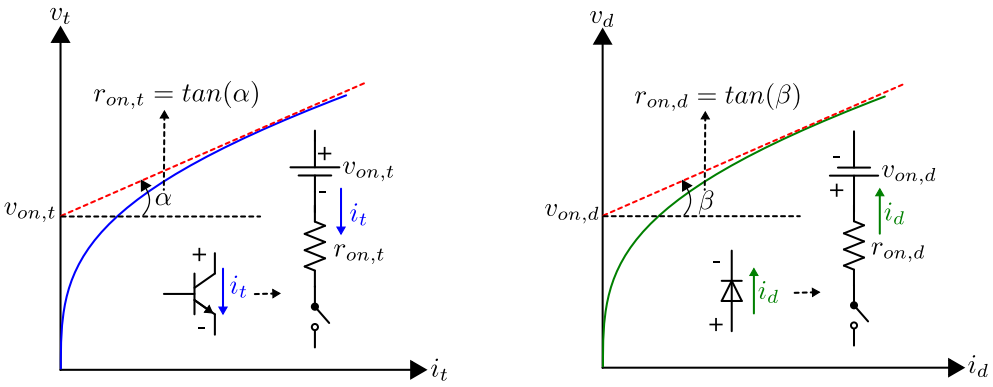

Figure 2.10: Typical output characteristics of switching devices: (a) *transistor*, (b) *diode*.

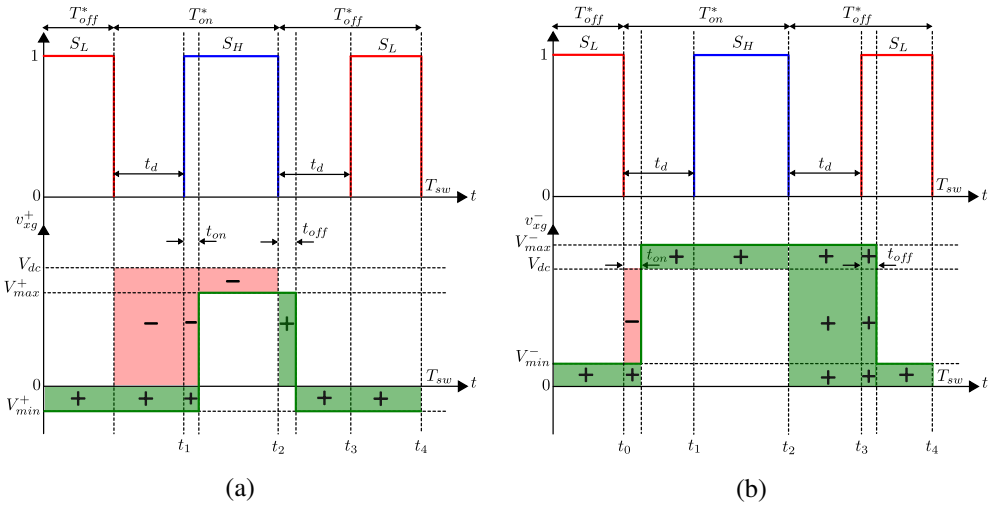

(a) (b)

Figure 2.11: Phase-to-ground output voltage of the inverter during one switching cycle, considering dead-time, switching delays, and device characteristics: (a) $i_x > 0$, (b) $i_x < 0$.

reduced output voltage. Similarly, the on-state resistance $r_{on,t}$ of the transistor introduces a voltage drop proportional to the current, contributing to power losses, particularly under high-load conditions. On the diode side, the forward voltage drop $v_{on,t}$ and its on-state resistance $r_{on,t}$ similarly reduce output voltage and add conduction losses, especially during freewheeling phases. While these characteristics are generally present in all switching devices, their magnitudes vary. For example, MOSFETs operate based on a field effect and do not have a distinct threshold voltage, effectively making $v_{on,t} = 0$ in ideal cases. These variations among device types contribute to the waveform distortion and the power losses in the inverter. The typical characteristics of these components are illustrated in Figure 2.10, and the voltage drop during conduction is approximated using a two-parameter model defined as follows:

$$v_t = v_{on,t} + r_{on,t}\, i_t \tag{2.10}$$

$$v_d = v_{on,d} + r_{on,d}\, i_d \tag{2.11}$$

This simplified model uses a threshold voltage and on-state resistance to represent the key behavior. Although it does not capture all the nonlinear effects, it is commonly used because it is easy to implement and accurate enough for most practical applications.

Applying the same analysis as in previous sections, for positive current flow, considering Figure 2.4 and Fig. 2.11a, the average output voltage is given by:

$$v_{xg}^{+} = \frac{T_{on}^{*} - t_d - (t_{on} - t_{off})}{T_{sw}} (v_{max}^{+} - v_{min}^{+}) + v_{min}^{+}, \quad i_x > 0 \tag{2.12}$$

where,

$$v_{max}^{+} = V_{dc} - (v_{on,t}^{H} + r_{on,t}^{H} |i_x|) \tag{2.13}$$

$$v_{min}^{+} = -(v_{on,d}^{L} + r_{on,d}^{L} |i_x|) \tag{2.14}$$

For negative current flow, considering Figure 2.5 and Fig. 2.11b, the output voltage is:

$$v_{xg}^{-} = \frac{T_{on}^{*} + t_d - (t_{on} - t_{off})}{T_{sw}} (v_{max}^{-} - v_{min}^{-}) + v_{min}^{-}, \quad i_x < 0 \tag{2.15}$$

where,

$$v_{max}^{-} = V_{dc} + (v_{on,d}^{H} + r_{on,d}^{H} |i_x|) \tag{2.16}$$

$$v_{min}^{-} = (v_{on,t}^{L} + r_{on,t}^{L} |i_x|) \tag{2.17}$$

Compared to the ideal output voltage in (2.1), the voltage drops for positive and negative current directions are defined as:

$$\begin{aligned}
\delta v_{xg}^{+} &= v_{xg}^{*} - v_{xg}^{+} \\
&= \frac{(t_d + t_{on} - t_{off})}{T_{sw}} V_{dc} \\
&+ \frac{(T_{on}^{*} - t_d - t_{on} + t_{off})}{T_{sw}} (v_{on,t}^{H} - v_{on,d}^{L}) \\
&+ \frac{(T_{on}^{*} - t_d - t_{on} + t_{off})}{T_{sw}} (r_{on,t}^{H} - r_{on,d}^{L}) |i_x| \\
&+ v_{on,d}^{L} + r_{on,d}^{L} |i_x|
\end{aligned} \tag{2.18}$$

$$\begin{aligned}
\delta v_{xg}^{-} &= v_{xg}^{*} - v_{xg}^{-} \\
&= \frac{-(t_d - t_{on} + t_{off})}{T_{sw}} V_{dc} \\
&+ \frac{(T_{on}^{*} + t_d - t_{on} + t_{off})}{T_{sw}} (v_{on,t}^{L} - v_{on,d}^{H}) \\
&+ \frac{(T_{on}^{*} + t_d - t_{on} + t_{off})}{T_{sw}} (r_{on,t}^{L} - r_{on,d}^{H}) |i_x| \\
&- v_{on,t}^{L} - r_{on,t}^{L} |i_x|
\end{aligned} \tag{2.19}$$

Figure 2.11 illustrates how component characteristics affect the average output voltage by reducing the positive voltage and increasing the negative voltage in one switching cycle, as highlighted in light red and green. In Figure 2.12, the amplitude of the voltage drop when using the same switching devices on high and low sides in different turn-on and turn-off delay states is illustrated. Asymmetry in the voltage drop was expected due to unequal turn-on and turn-off delays. In another case, shown in Figure 2.13, it is found that different characteristics of the low- and high-side components also caused asymmetry.

2.4.4 Parasitic Capacitance

In an inverter driving an inductive load, the parasitic capacitances of switching devices play a critical role in the switching process, particularly during the dead-time

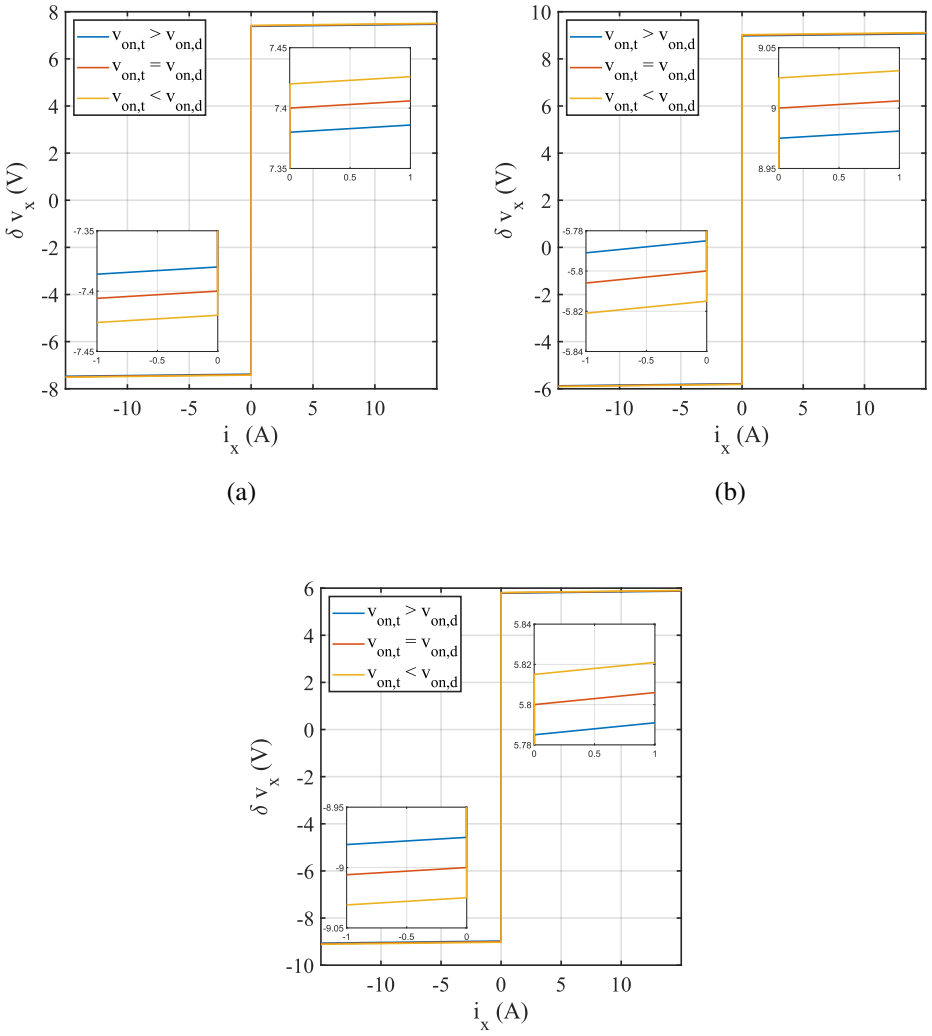

Figure 2.12: Voltage drop sensitivity to switching device delay configurations:: (a) $t_{on} = t_{off}$, (b) $t_{on} > t_{off}$, (c) $t_{on} < t_{off}$.

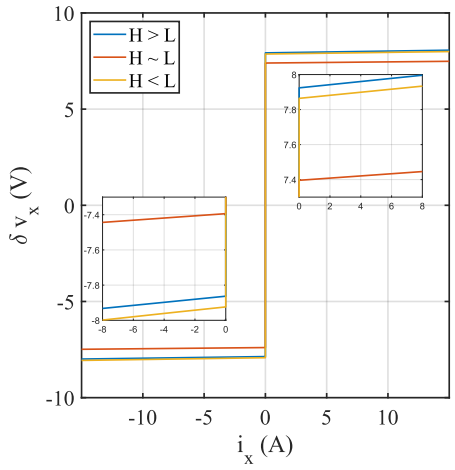

Figure 2.13: Voltage drop sensitivity due to differences between high- and low-side inverter leg components, comparing cases where high-side parameters are greater, less, or equal to those of the low side.

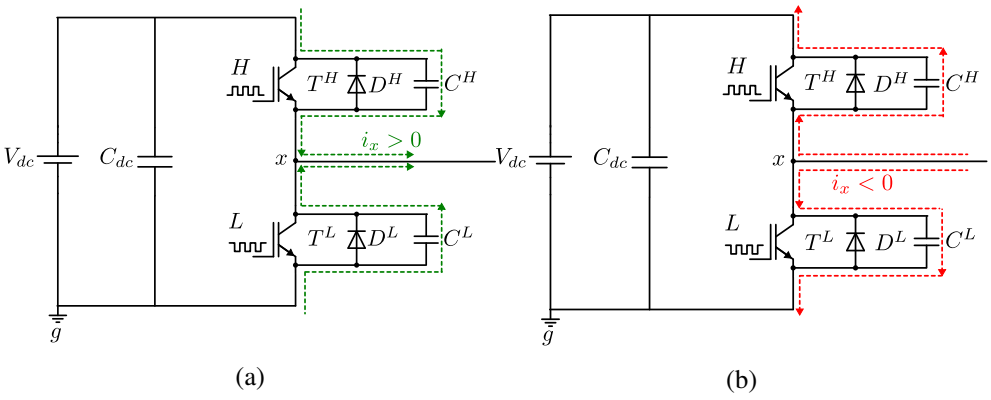

Figure 2.14: Transient current paths during dead-time due to parasitic capacitances: (a) $S_H : on \rightarrow off$, (b) $S_H : off \rightarrow on$.

period. During this interval, the parasitic capacitances of the switches charge and discharge, influencing the voltage transitions and causing additional delays. This effect behaves differently depending on the direction of the current (positive or negative) flowing through the inverter phase.

A key assumption in this analysis is that the parasitic capacitances of the high-side (C^H) and low-side (C^L) switches are linear, meaning their capacitance values remain constant irrespective of the applied voltage. However, in practice, C^H and C^L are nonlinear and vary as a function of voltage, which can lead to deviations from the idealized model. Despite this nonlinearity, assuming linear C^H and C^L allows for a simplified mathematical representation of the system, making it easier to analyze the switching behavior.

Furthermore, if both C^H and C^L are assumed linear and the DC supply is considered ideal, the capacitances are effectively in parallel during certain switching transitions. This assumption can be used to simplify the voltage equations and predict the expected charge/discharge dynamics more easily.

Moreover, this analysis assumes a constant current during the transition, which simplifies the explanation of the switching behavior. However, in real systems, particularly at low current levels or in the presence of an output filter, the voltage transition can exhibit damped resonant behavior due to the interaction of parasitic capacitances and inductances. This introduces deviations from the idealized case presented in our study and represents a limitation of this simplified model.

Considering a constant positive phase current direction $i_x > 0$, flowing from the inverter to the load, the dead-time begins when the high-side switch of the phase leg is turned off. At the start of the dead-time, the output voltage v_{xg}^+ is initially close to the positive DC bus voltage. The lower parasitic capacitance C^L of the switch is fully charged, while the upper parasitic capacitance C^H is discharged. Since the current i_x is positive assuming to flow through a (partly) inductive load, it attempts to maintain its direction even during dead-time. To maintain this current path, i_x must discharge C^L and simultaneously charge C^H. This current path through the parasitic capacitances is provided by other phases via the DC bus, as shown in Fig. 2.14a. As the phase current discharges C^L and charges C^H, the voltage at the output node v_{xg}^+

begins to transition from near the positive DC bus voltage downward to the negative DC bus voltage. This transition is not instantaneous; the time it takes depends on the capacitance values and the magnitude of i_x. Only after C^L is fully discharged and C^H is sufficiently charged, the voltage v_{xg}^+ reaches the negative DC bus voltage, allowing the lower diode to conduct and maintain the current flow. This process ensures that the current can continue flowing through the load despite the switches being off, but it introduces a delay in the effective voltage transition due to the time needed to charge and discharge the parasitic capacitances.

For the negative phase current direction $i_x < 0$, flowing into the inverter from the load, the switching dynamics and the behavior of the parasitic capacitance change. In this case, assuming that the lower switch was conducting before dead-time began, the high-side parasitic capacitance C^H of the switch is fully charged, and C^L is discharged. At the beginning of the dead-time, the voltage v_{xg}^- is initially near the negative DC bus voltage since the lower switch was conducting. The negative phase current now needs to maintain its direction, which requires charging C^L and discharging C^H. To achieve this, i_x flows through the DC bus and charges C^L while simultaneously discharging C^H, as shown in Fig. 2.14b. As C^H discharges and C^L charges, the voltage at v_{xg}^- begins to rise from zero toward the DC bus voltage. The time required to complete this voltage transition depends on the capacitance values and the magnitude of the current. Once C^H is fully discharged and C^L is adequately charged, the upper diode can start conducting, allowing the current to flow through this path and maintain current continuity during dead-time. While this transition causes a delay similar to the positive current case, it is important to note that the associated switching event is relatively "soft". Since the load current naturally charges and discharges the parasitic capacitances, the energy is not abruptly dissipated, and switching losses during this transition are minimal. In contrast, hard switching events, where the device turns on while the capacitors are still charged, can result in significant energy dissipation (approximately $2 \times \frac{1}{2}CV^2$).

It is worth mentioning that the behavior during dead-time differs between MOSFETs and IGBTs, primarily due to their inherent structural and operational characteristics. MOSFETs, with their lower parasitic capacitance and unipolar conduc-

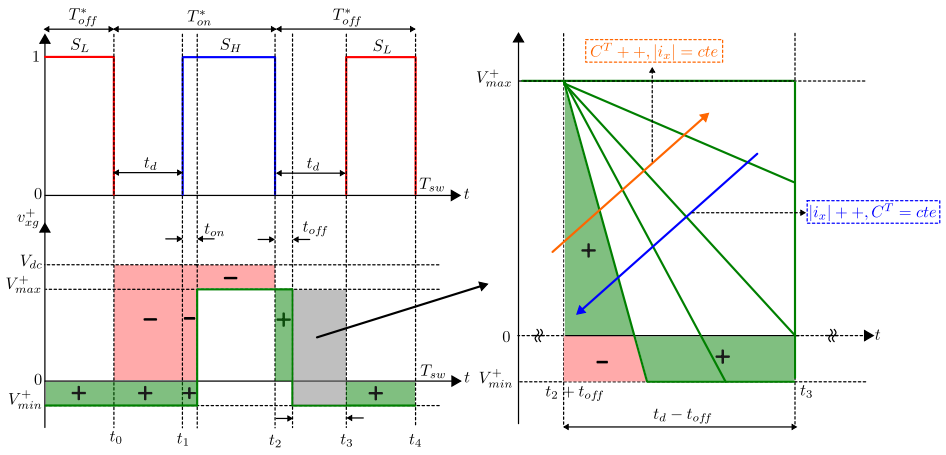

(a)

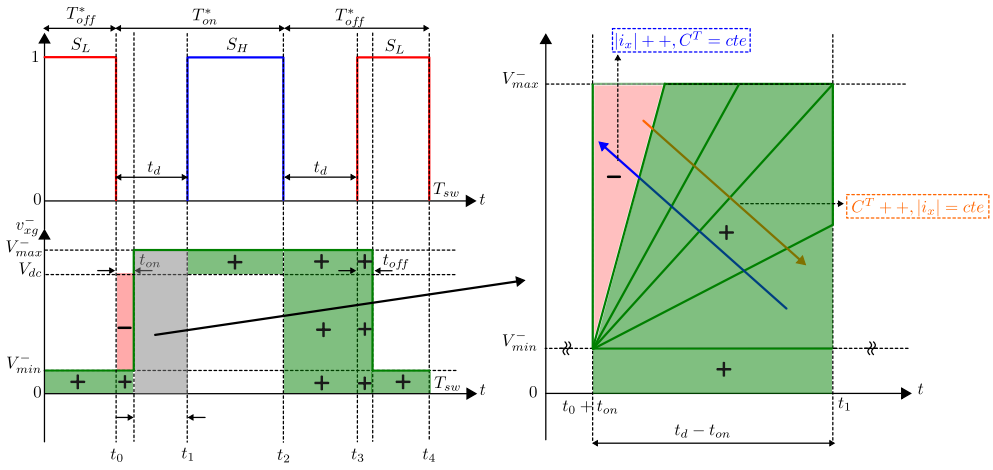

(b)

Figure 2.15: Phase-to-ground output voltage of the inverter during one switching cycle, including parasitic capacitance effects: (a) $i_x > 0$, (b) $i_x < 0$.

tion, enable faster voltage transitions and reduced switching losses. This makes them particularly well-suited for high-speed switching applications, especially when synchronous rectification is employed to further enhance efficiency by minimizing body diode conduction losses. Conversely, IGBTs, with higher parasitic capacitance and bipolar conduction, exhibit slower transitions and cause increment on the switching losses, limiting their efficiency gains with synchronous rectification. These distinctions emphasize on the importance of considering device selection in optimizing dead-time behavior and overall system performance.

To extract the output average voltage model considering the parasitic capacitance, it is necessary to separate the parasitic capacitance effect region from other contributions, as shown in Figure 2.15, highlighted in gray. For the positive current direction, using the same analytical procedure as in the previous sections, the output average voltage is given by:

$$v_{xg}^{+} = \frac{T_{on}^{*} - t_d - (t_{on} - t_{off})}{T_{sw}} (v_{max}^{+} - v_{min}^{+}) + v_{min}^{+} - \frac{(t_d - t_{off})}{T_{sw}} v_{min}^{+} + \frac{F^{+}}{T_{sw}} \quad i_x > 0 \tag{2.20}$$

For the negative current direction, we have:

$$v_{xg}^{-} = \frac{T_{on}^{*} + t_d - (t_{on} - t_{off})}{T_{sw}} (v_{max}^{-} - v_{min}^{-}) + v_{min}^{-} - \frac{(t_d - t_{on})}{T_{sw}} v_{max}^{-} + \frac{F^{-}}{T_{sw}}, \quad i_x < 0 \tag{2.21}$$

where F^{+} and F^{-} describe the regions affected by parasitic capacitance which should be analyzed to determine the relevant model.

In the following section, different scenarios occurring in these regions, based on the charging time of the capacitors, are studied with reference to Figure 2.16 and Figure 2.17. In the figures and analysis, the auxiliary parameter t_{cut} represents the time at which the voltage crosses zero in a switching cycle.

For the positive current direction, five different situations can occur depending on different values of the capacitance charging time, as shown in Figure 2.16. Using the triangle similarity theorem, the following values for F^{+} are calculated:

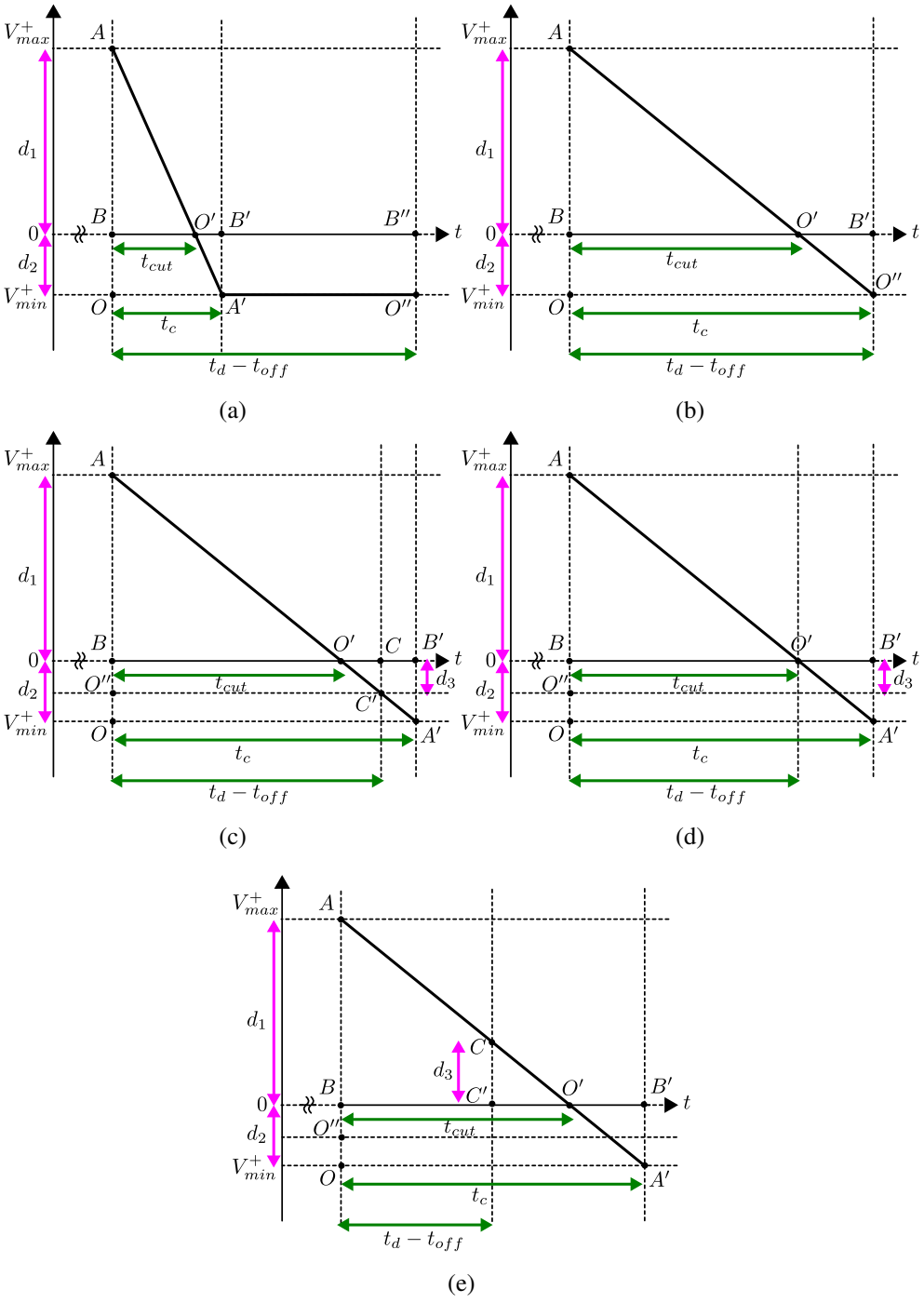

Figure 2.16: Different scenarios arising from parasitic capacitance for positive current direction ($i_x > 0$): (a) $t_{cut} < t_c^+ < t_d - t_{off}$, (b) $t_{cut} < t_c^+ = t_d - t_{off}$, (c) $t_{cut} < t_d - t_{off} < t_c^+$, (d) $t_{cut} = t_d - t_{off} < t_c^+$, (e) $t_d - t_{off} < t_{cut} < t_c^+$.

- Fig. 2.16a : $(t_{cut} < t_c^+ < t_d - t_{off})$
  $\Delta O'BA \sim \Delta A'OA \rightarrow F^+ = \frac{1}{2}(d_1 + d_2)t_c^+ - d_2(t_d - t_{off})$
  $F^+ = \frac{1}{2}(v_{max}^+ - v_{min}^+)t_c^+ + v_{min}^+(t_d - t_{off})$

- Fig. 2.16b : $(t_{cut} < t_c^+ = t_d - t_{off})$
  $\Delta O'BA \sim \Delta A'OA \rightarrow F^+ = \frac{1}{2}(d_1 - d_2)t_c^+$
  $F^+ = \frac{1}{2}(v_{max}^+ + v_{min}^+)t_c^+$

- Fig. 2.16c : $(t_{cut} < t_d - t_{off} < t_c^+)$
  $\Delta O'BA \sim \Delta A'OA, \Delta O'BA \sim \Delta C'O''A \rightarrow F^+ = \frac{1}{2}(2(td - t_{off})d_1 - \frac{(t_d - t_{off})^2}{t_c^+}(d_1 + d_2))$
  $F^+ = \frac{1}{2}(2(t_d - t_{off})v_{max}^+ - \frac{(t_d - t_{off})^2}{t_c^+}(v_{max}^+ - v_{min}^+))$

- Fig. 2.16d : $(t_{cut} = t_d - t_{off} < t_c^+)$
  $\Delta O'BA \sim \Delta A'OA \rightarrow F^+ = \frac{1}{2}d_1(t_d - t_{off})$
  $F^+ = \frac{1}{2}(t_d - t_{off})v_{max}^+$

- Fig. 2.16e : $(t_d - t_{off} < t_{cut} < t_c^+)$
  $\Delta O'BA \sim \Delta A'OA, \Delta O'BA \sim \Delta O'C'C \rightarrow F^+ = \frac{1}{2}(2(td - t_{off})d_1 - \frac{(t_d - t_{off})^2}{t_c^+}(d_1 + d_2))$
  $F^+ = \frac{1}{2}(2(t_d - t_{off})v_{max}^+ - \frac{(t_d - t_{off})^2}{t_c^+}(v_{max}^+ - v_{min}^+))$

Combining all the equations extracted from the analysis in different states for the positive current direction, we have:

$$F^+ = \begin{cases} \frac{1}{2}(v_{max}^+ - v_{min}^+)t_c^+ + v_{min}^+(t_d - t_{off}) & t_c^+ < t_d - t_{off} \\ \frac{1}{2}(v_{max}^+ + v_{min}^+)t_c^+ & t_c^+ = t_d - t_{off} \\ \frac{1}{2}(2(t_d - t_{off})v_{max}^+ - \frac{(t_d - t_{off})^2}{t_c^+}(v_{max}^+ - v_{min}^+)) & t_c^+ > t_d - t_{off} \end{cases} \tag{2.22}$$

where t_c^+ is defined as follows by applying Kirchhoff's Current Law (KCL) in Fig. 2.14a:

$$t_c^+ = (C^H + C^L)\left(\frac{V_{dc} - v_{on,t}^H + v_{on,d}^L}{|i_x|} + r_{on,d}^L - r_{on,t}^H\right) \tag{2.23}$$

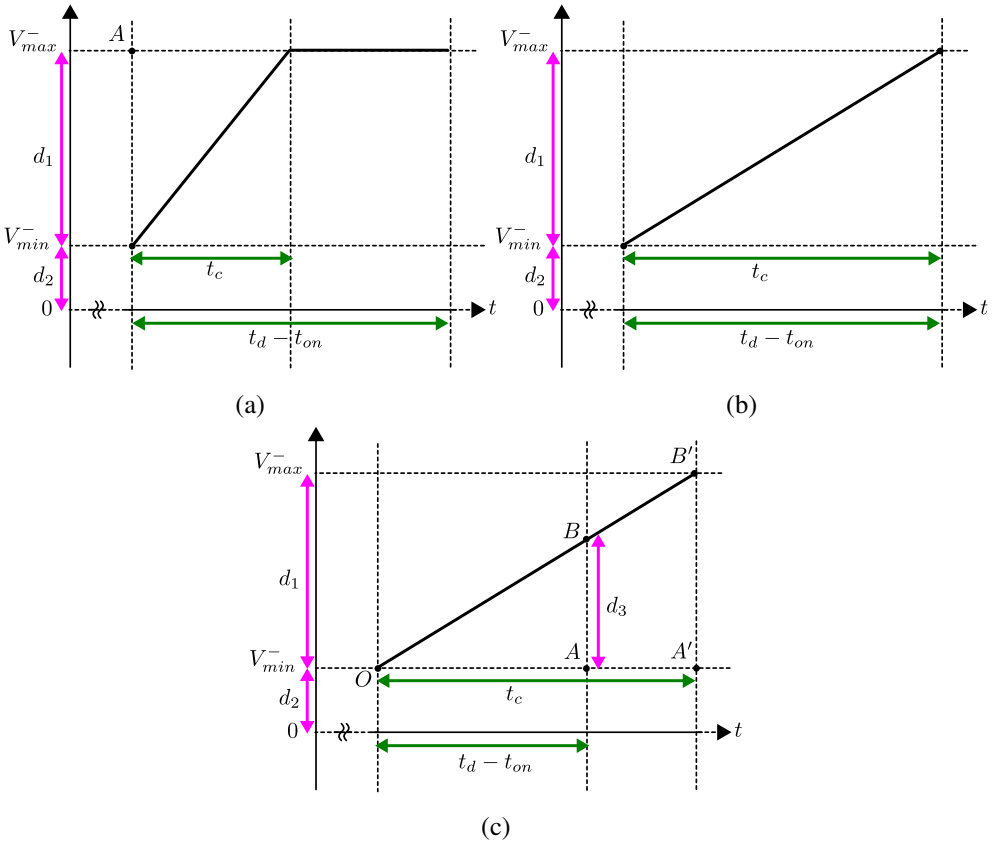

Figure 2.17: Different scenarios arising from parasitic capacitance for negative current direction ($i_x < 0$): (a) $t_c^- < t_d - t_{on}$, (b) $t_c^- = t_d - t_{on}$, (c) $t_d - t_{on} < t_c^-$.

Similarly, for the negative current direction, three different situations might occur depending on different values of the capacitance charging time, as shown in Figure 2.17. Using the simple triangle similarity theorem, the following values for F^- are calculated:

- Fig. 2.17a : $(t_c^- < t_d - t_{on})$
  $F^- = \frac{-1}{2} d_1 t_c^- + (d_1 + d_2)(t_d - t_{on})$
  $F^- = \frac{-1}{2}(v_{max}^- - v_{min}^-)t_c^- + v_{max}^-(t_d - t_{on})$
- Fig. 2.17b : $(t_c^- = t_d - t_{on})$
  $F^- = \frac{1}{2}(2d_2 + d_1)t_c^-$
  $F^- = \frac{1}{2}(v_{max}^- + v_{min}^-)t_c^-$
- Fig. 2.17c : $(t_d - t_{on} < t_c^-)$
  $\Delta OAB \sim \Delta OA'B' \rightarrow F^- = \frac{1}{2}(2(t_d - t_{on})d_2 + \frac{(t_d - t_{on})^2}{t_c^-} d_1)$
  $F^- = \frac{1}{2}(2(t_d - t_{on})v_{min}^- + \frac{(t_d - t_{on})^2}{t_c^-}(v_{max}^- - v_{min}^-))$

Combining all the equations extracted from the analysis in different states for the negative current direction, we have:

$$F^- = \begin{cases} \frac{-1}{2}(v_{max}^- - v_{min}^-)t_c^- + v_{max}^-(t_d - t_{on}) & t_c^- < t_d - t_{on} \\ \frac{1}{2}(v_{max}^- + v_{min}^-)t_c^- & t_c^- = t_d - t_{on} \\ \frac{1}{2}(2(t_d - t_{on})v_{min}^- + \frac{(t_d - t_{on})^2}{t_c^-}(v_{max}^- - v_{min}^-)) & t_c^- > t_d - t_{on} \end{cases} \tag{2.24}$$

where t_c^- is defined as follows by applying Kirchhoff's Current Law (KCL) in Fig. 2.14b:

$$t_c^- = (C^H + C^L)\left(\frac{V_{dc} + v_{on,d}^H - v_{on,t}^L}{|i_x|} + r_{on,d}^H - r_{on,t}^L\right) \tag{2.25}$$

Considering the critical charging time as $t_c^+ = t_d - t_{off}$ and $t_c^- = t_d - t_{on}$ for the positive and negative current directions respectively, the critical current is defined as follows:

$$\begin{cases} I_{cr}^{+} = \dfrac{(V_{dc}-v_{on,t}^{H}+v_{on,d}^{L})(C^{H}+C^{L})}{(t_d-t_{off})-(r_{on,d}^{L}-r_{on,t}^{H})(C^{H}+C^{L})} & i_x > 0 \\ I_{cr}^{-} = -\dfrac{(V_{dc}+v_{on,d}^{H}-v_{on,t}^{L})(C^{H}+C^{L})}{(t_d-t_{on})-(r_{on,d}^{H}-r_{on,t}^{L})(C^{H}+C^{L})} & i_x < 0 \end{cases} \tag{2.26}$$

According to Figure 2.18, it is clear that parasitic capacitance affects the output voltage drop, introducing additional nonlinearity that must be accurately identified for drive applications, particularly at lower currents where the voltage drop due to resistive components is small, making the capacitive effects more prominent by comparison.

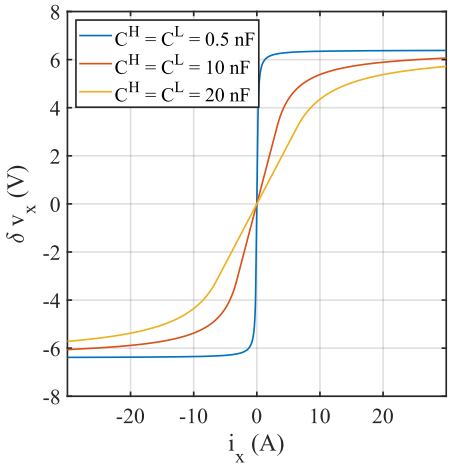

Figure 2.18: Sensitivity of voltage drop to variations in parasitic capacitance.

2.5 Inverter Model Verification

To validate the provided analytical model, it has been simulated in Plecs software using a C-script and compared with the output voltage of the built-in Plecs inverter model and blocks using the same parameters in Table 2.1. The schematic of the verification procedure is illustrated in Figure 2.19 and Figure 2.20. In the Plecs simulation schematic, a reference voltage V_{ref} and reference frequency f_{ref} are set as inputs to

Table 2.1: Simulation parameters for model verification in PLECS.

Parameter	V_{dc}	f_{sw}	t_d	t_{on}	t_{off}	$r_{t,on}$	$r_{d,on}$	$v_{t,on}$	$v_{d,on}$
Value	320	10	2	0.25	0.5	0.07	0.06	0.7	0.6
Unit	V	kHz	μs	μs	μs	Ω	Ω	V	V

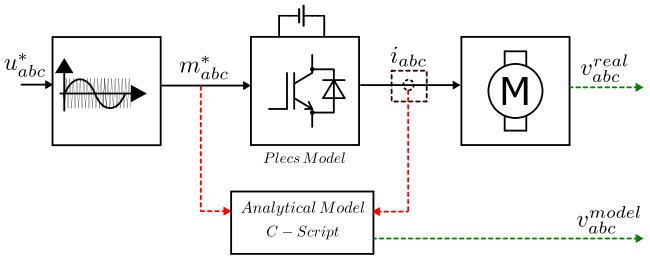

Figure 2.19: Diagram of the inverter model verification procedure.

the voltage generator block, which processes these values and converts them into appropriate three-phase voltage references v_{an}^{ref}, v_{bn}^{ref}, v_{cn}^{ref}. These references are then fed into the SPWM block, which generates the corresponding PWM switching signals for the Plecs Inverter. The inverter applies these switching patterns to produce the three-phase AC output voltage that drives the motor. Additionally, a torque measurement block is included, though it has been set to zero, suggesting that the motor operates in an unloaded condition. The entire system functions to validate the analytical model and examine the nonlinear behavior of the inverter under different operating conditions. This procedure was repeated for four different scenarios. The input reference voltage, output voltage, current, and corresponding harmonics are illustrated in Figure 2.21 to Figure 2.24. For the spectrum calculations, the last two cycles of the data have been used. These scenarios include two different reference voltage amplitudes ($25V, 100V$), each simulated at two different frequencies ($5Hz, 50Hz$). According to the simulation results and comparisons, the extracted model is verified and can be used for further analysis, as the outputs closely match those of the built-in Plecs inverter model. Additionally, based on the analysis at different voltage levels, it is evident that voltage and current are more noticeable at low voltage and high frequency.

It should be noted that the output voltage does not significantly change between 5 Hz and 50 Hz, even though a higher voltage is typically expected at higher frequencies. This may happen due to different reasons within the Plecs simulation. One key reason is that the modulation index in the PWM control likely remains constant, meaning that the output voltage amplitude of the inverter is not dynamically adjusted with frequency. In practical applications, V/f control is often used in simple IM drives to scale the voltage with frequency and maintain proper flux. For other machines like PMSMs, however, a constant V/f ratio is not directly applied as a strategy. It is more of a result of the control method aiming to keep the flux constant. However, in the current simulation setup, this proportional adjustment has not been implemented, leading to an almost unchanged voltage output regardless of frequency.

The general model extracted for inverter nonlinearity is very complex for self-commissioning, as it considers many parameters. To simplify the model, it is assumed that the inverter is balanced and that both sides of the inverter leg are identical. The turn-on and turn-off delays have been neglected since they are much smaller than the dead-time duration. Therefore, the following model has been proposed for inverter nonlinearity, which will be used for further analysis in this study:

$$\delta v_{xg}^{+} = \begin{cases} v_{on,d} + r_{on,d} i_x + \frac{t_d v_{dc}}{T_{sw}} - \frac{C_{out} v_{dc}^2}{T_{sw} i_x} & i_x >= I_{cr} \\ v_{on,d} + r_{on,d} i_x + \frac{t_d^2 i_x}{4 C_{out} T_{sw}} & 0 < i_x < I_{cr} \end{cases} \tag{2.27}$$

$$\delta v_{xg}^{-} = \begin{cases} -v_{on,t} + r_{on,t} i_x - \frac{t_d v_{dc}}{T_{sw}} - \frac{C_{out} v_{dc}^2}{T_{sw} i_x} & i_x <= -I_{cr} \\ -v_{on,t} + r_{on,t} i_x + \frac{t_d^2 i_x}{4 C_{out} T_{sw}} & -I_{cr} < i_x < 0 \end{cases} \tag{2.28}$$

where $I_{cr} = \frac{2 C_{out} V_{dc}}{t_d}$ and $C_{out} = C^H = C^L$.

Considering the balanced three-phase system, the phase-to-ground model can be converted to the phase-to-neutral model using:

$$\begin{bmatrix} \delta v_{an} \\ \delta v_{bn} \\ \delta v_{cn} \end{bmatrix} = \frac{1}{3} \begin{bmatrix} 2 & -1 & -1 \\ -1 & 2 & -1 \\ -1 & -1 & 2 \end{bmatrix} \begin{bmatrix} \delta v_{ag} \\ \delta v_{bg} \\ \delta v_{cg} \end{bmatrix} \tag{2.29}$$

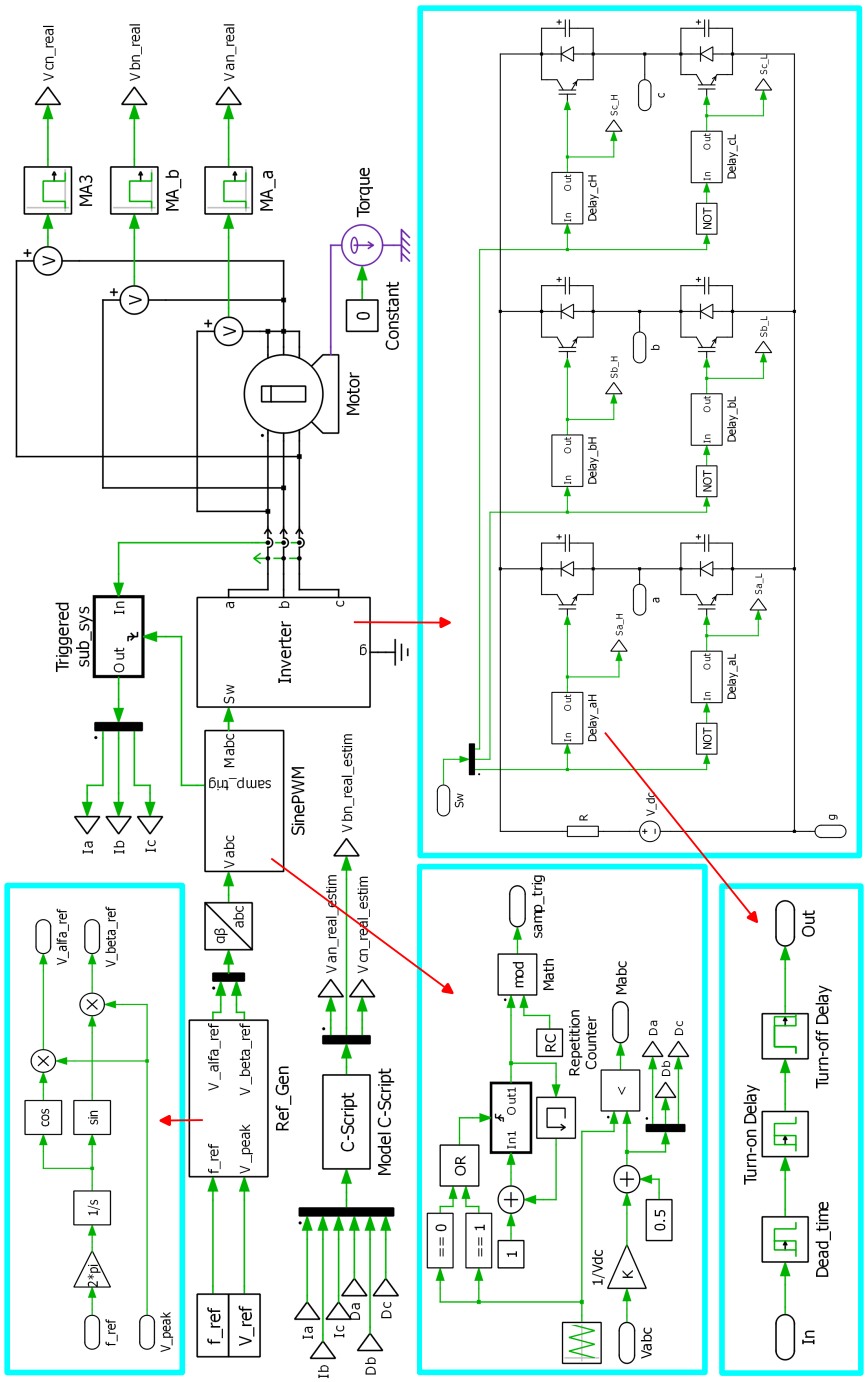

Figure 2.20: Plecs simulation schematic used for inverter model verification.

The phase-A voltage error considering excitation in the d-axis is given as follows, assuming $i_b = i_c = \frac{-i_a}{2}$:

$$\delta v_{an}(i_a) = \begin{cases} (\frac{v_{on,d}}{2} + \frac{v_{on,t}}{2} + \frac{t_d v_{dc}}{T_{sw}})sgn(i_a) + \frac{r_{on,d} i_a}{2} + \frac{r_{on,t} i_a}{2} - \frac{C_{out} v_{dc}^2}{T_{sw} i_a} & |i_a| >= I_{cr} \\ (\frac{v_{on,d}}{2} + \frac{v_{on,t}}{2})sgn(i_a) + \frac{r_{on,d} i_a}{2} + \frac{r_{on,t} i_a}{2} + \frac{t_d^2 i_a}{4 C_{out} T_{sw}} & |i_a| < I_{cr} \end{cases} \tag{2.30}$$

The phase-B voltage error considering excitation in the q-axis is given as follows, assuming $i_a = 0$, $i_c = -i_b$:

$$\delta v_{bn}(i_b) = \frac{\sqrt{3}}{2} \begin{cases} (\frac{v_{on,d}}{2} + \frac{v_{on,t}}{2} + \frac{t_d v_{dc}}{T_{sw}})sgn(i_b) + \frac{r_{on,d} i_b}{2} + \frac{r_{on,t} i_b}{2} - \frac{C_{out} v_{dc}^2}{T_{sw} i_b} & |i_b| >= I_{cr} \\ (\frac{v_{on,d}}{2} + \frac{v_{on,t}}{2})sgn(i_b) + \frac{r_{on,d} i_b}{2} + \frac{r_{on,t} i_b}{2} + \frac{t_d^2 i_b}{4 C_{out} T_{sw}} & |i_b| < I_{cr} \end{cases} \tag{2.31}$$

2.6 Inverter Nonlinearity Self-commissioning

Inverter nonlinearity self-commissioning can be achieved using a lookup table method that applies a DC voltage in incremental steps. This technique involves systematically applying a series of DC voltage steps, each corresponding to a distinct point, to capture the nonlinear characteristics of the inverter. By measuring the voltage-current pairs at each step, a detailed lookup table can be constructed, including the nonlinear voltage drops in the inverter system.

This self-commissioning process utilizes the lookup table to map the response of the inverter to various operating points, allowing the control algorithm to compensate for these nonlinearities in real-time. The approach improves the accuracy of the inverter in controlling the motor output by providing a pre-measured reference for expected voltage behavior across different load conditions, effectively improving overall system performance without requiring additional sensors or extensive manual calibration.

The typical lookup table-based self-commissioning method involves injecting a sequence of DC currents in one direction through the current control loop and record-

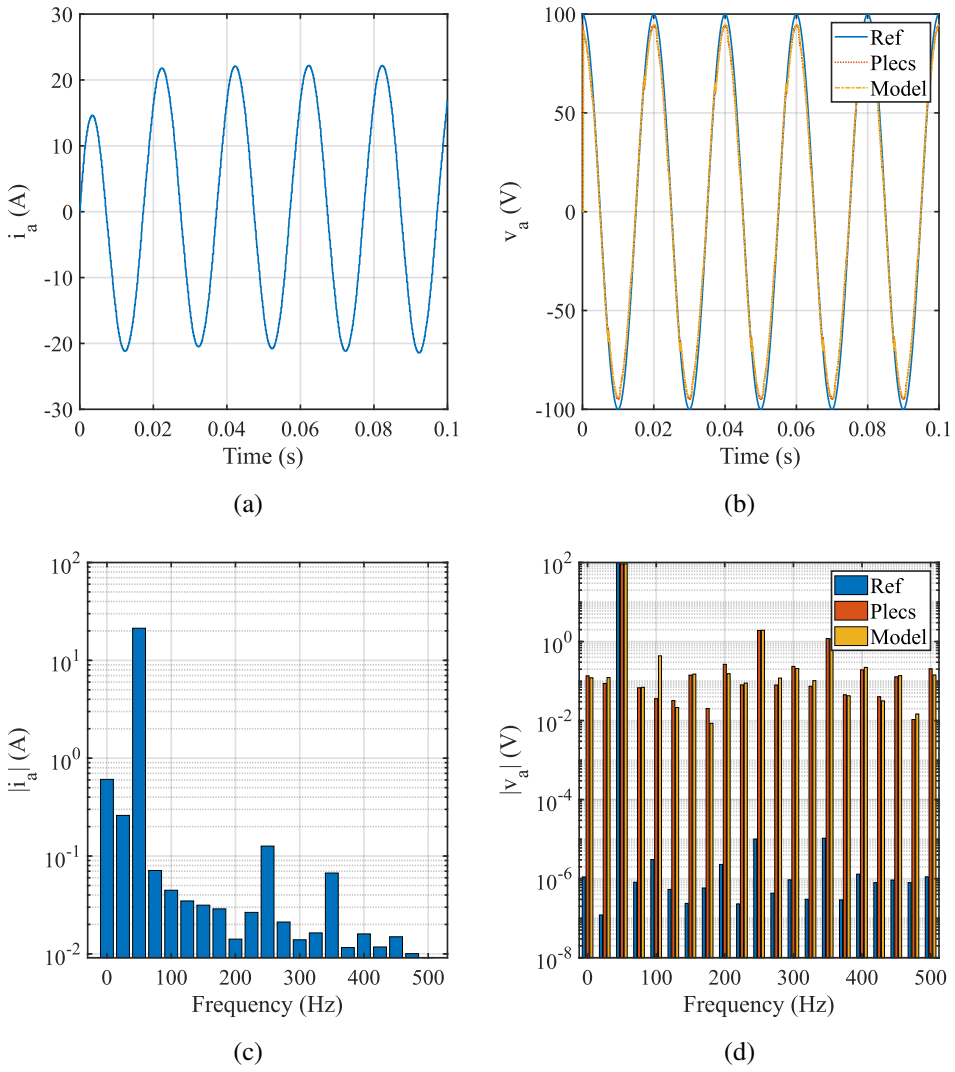

Figure 2.21: Simulation results comparing the proposed model with the Plecs model in time and frequency domains for $|v_a^*| = 100V$ and $f = 50Hz$.

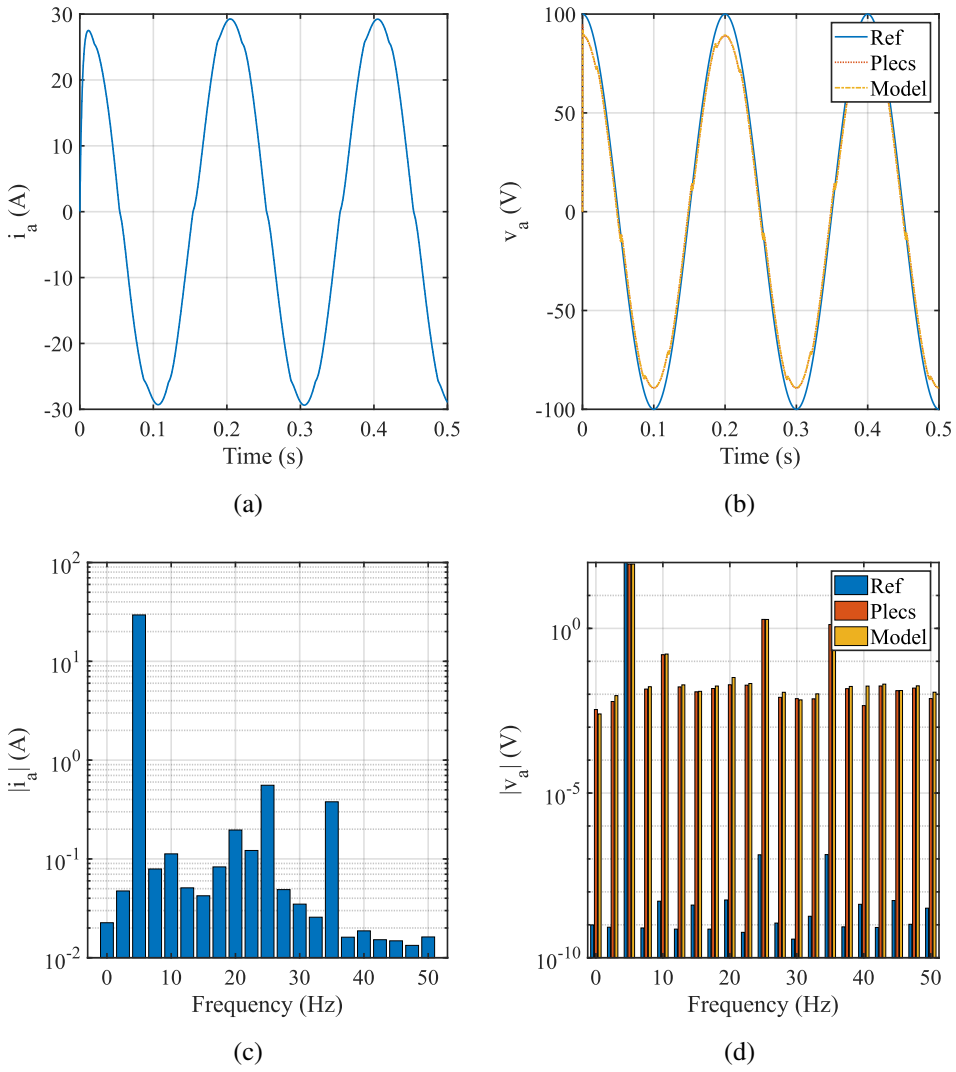

Figure 2.22: Simulation results comparing the proposed model with the Plecs model in time and frequency domains for $|v_a^*| = 100V$ and $f = 5Hz$.

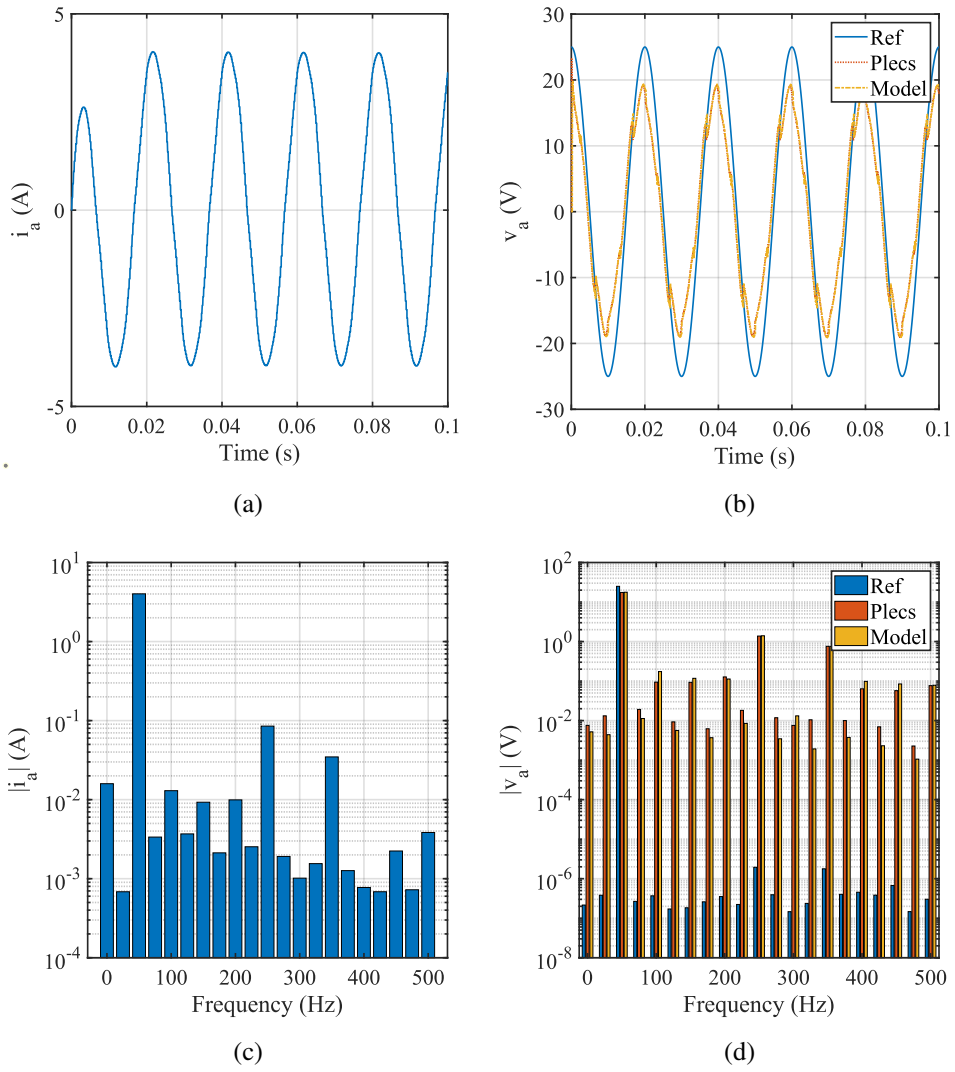

Figure 2.23: Simulation results comparing the proposed model with the Plecs model in time and frequency domains for $|v_a^*| = 25\,V$ and $f = 50\,Hz$.

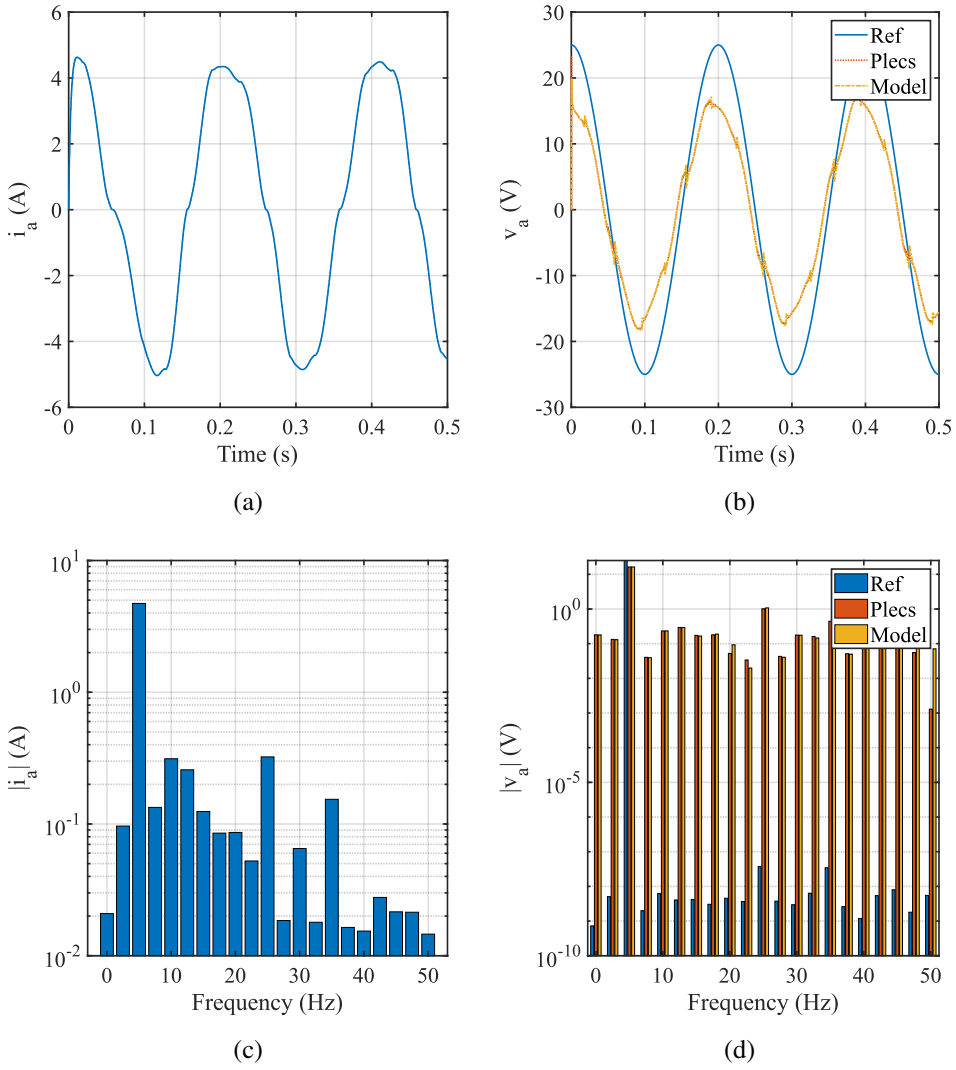

Figure 2.24: Simulation results comparing the proposed model with the Plecs model in time and frequency domains for $|v_a^*| = 25V$ and $f = 5Hz$.

ing the voltage reference at steady states [28]. However, based on the conducted analysis, this approach has limitations. The voltage drop may be asymmetric, and relying on the current injection in one direction may not correctly result in the characteristics of the inverter. Additionally, this method estimates total resistance using a two-step current injection, which is often impractical to replicate consistently. Moreover, the traditional approach assumes the presence of a current controller to regulate and inject currents precisely, making it unsuitable when the inverter and load are treated as a black box.

In contrast, in this study, a new bidirectional procedure is proposed for self-commissioning the inverter voltage drop in an open-loop configuration at standstill. Since the method relies on steady-state responses, it primarily accounts for the resistive voltage drop while minimizing the influence of inductance, offering a more practical solution for industrial applications. The proposed method does not rely on an active current controller but instead applies controlled voltage steps and observes the natural response of the system, allowing for self-commissioning even in an open-loop configuration. However, for a high-efficiency system, even very small voltages can result in high current. So, the current protection is utilized.

2.6.1 Typical Inverter Nonlinearity Self-commissioning Method

Among recent advancements in drive control, the work of Bojoi et al. [28] presents a robust and hardware-independent self-commissioning algorithm for identifying inverter nonlinearities, particularly dead-time effects and on-state voltage drops, at standstill, with no need for rotor movement or detailed inverter modeling. The method is designed for ease of implementation, using only a conventional current control loop, and is suitable for various motor types such as induction and PMSM or even resistive-inductive (RL) loads.

The total inverter voltage error is captured by the following equation:

$$\vec{v}_{\text{err}} = \frac{4}{3} V'_{\text{th}} \cdot \text{sgn}(\vec{i}) + R_d \cdot \vec{i} \tag{2.32}$$

where:

- $\vec{i} = [i_\alpha, i_\beta]^T$ is the stator current vector in the stationary α-β frame,
- $\text{sgn}(\vec{i})$ is a quantized vector with six directions (hexagonally distributed),
- $V'_{\text{th}} = V_{\text{dc}} f_{sw} t_d + V_{\text{th}}$ is the total threshold voltage including both dead-time and device threshold voltage,
- R_d is the dynamic resistance modeling the on-state linear drop.

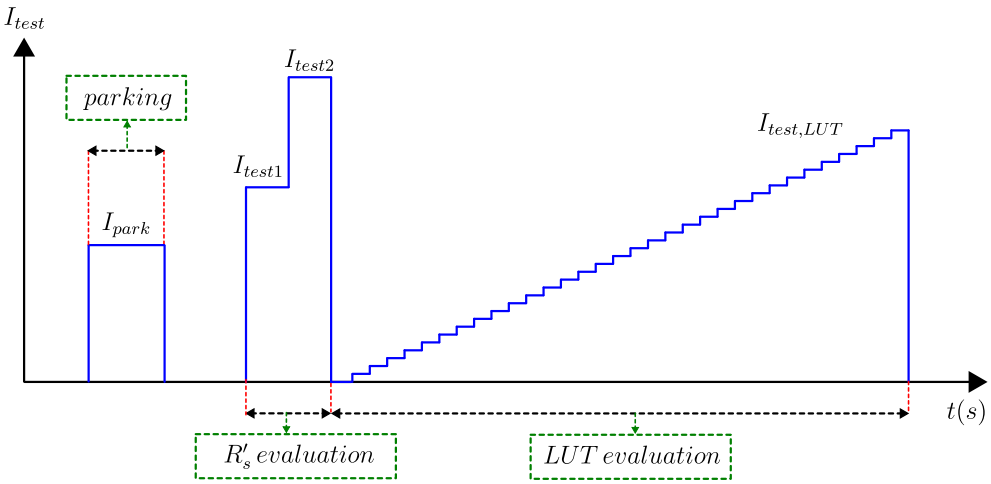

Figure 2.25: Complete current profile for the inverter identification by using typical method.

The complete test current waveform used during the identification routine has been shown in Figure 2.25. It starts with a short parking current (used only for PM machines) for alignment and ensuring the standstill condition, followed by two main steps.

Two DC current levels, $I_{\text{test},1}$ and $I_{\text{test},2}$, are injected sequentially along the α-axis, and the resulting steady-state voltages are used to estimate the total series resistance. This step assumes the nonlinear voltage component remains constant between the two levels. At steady state, the reference voltage generated by the controller is:

$$V^*_\alpha = \frac{4}{3} V'_{\text{th}} + i_\alpha R'_s \tag{2.33}$$

where $R'_s = R_s + R_d$ is the total series resistance (stator and inverter).

By measuring V^*_α at two current levels, R'_s is identified as:

$$R'_s = \frac{V^*_{\alpha,2} - V^*_{\alpha,1}}{I_{\text{test},2} - I_{\text{test},1}} \tag{2.34}$$

Next, a staircase current profile is applied along the α-axis to scan different current levels. At each current step k, the reference voltage is recorded:

$$v^*_\alpha(k) = \frac{4}{3}V'_{\text{th}} + I_\alpha(k)R'_s \tag{2.35}$$

Then, the pole voltage error is extracted as:

$$\delta V_\alpha(k) = \frac{3}{4}[v^*_\alpha(k) - I_\alpha(k)R'_s] \tag{2.36}$$

This value is stored in a lookup table indexed by the phase current I_α, as the α-axis corresponds to the phase a direction.

2.6.2 Proposed Inverter Nonlinearity Self-commissioning Method

The proposed self-commissioning procedure for inverter nonlinearity begins with aligning the d-axis of the rotor with the α-axis by applying an appropriate voltage and setting the inverse Park transformation position to zero. However, depending on the initial conditions and voltage application, the rotor may experience slight movement due to residual torque, particularly in the q-axis. This effect is influenced by the generated torque, which can cause unintended rotation if the applied voltage is not properly controlled. The alignment process typically follows either an a-to-bc or b-to-c current flow as shown in Fig. 2.26c and Fig. 2.27c, ensuring a defined electrical excitation pattern.

Additionally, for loads with high inertia, the alignment process may take longer or result in high current draw, as overcoming the resistance of the rotor to motion requires greater effort. To remove these challenges, a gradual voltage ramp, a current-limited control strategy, or an initial rotor position estimation method can be employed to ensure stable alignment without excessive current spikes. Notably, our experimental results indicate that the initialization voltage ramp itself helps the rotor

alignment, reducing the need for further correction. This effect is visible in the measured data, confirming that the rotor alignment is stabilized before the main procedure begins. Ensuring the motor is unloaded during alignment further improves accuracy and minimizes current transients.

The procedure can be performed in two scenarios:

1. Applying voltage along the d-axis with zero voltage on the q-axis, as shown in Fig. 2.26a.
2. Applying voltage along the q-axis with zero voltage on the d-axis, as shown in Fig. 2.27a.

Both scenarios aim to log the behavior of the inverter and create a lookup table for nonlinearity compensation and are expected to yield approximately the same results. The schematic of the proposed self-commissioning process is illustrated in Figure 2.28.

First Scenario: Voltage Applied Along the d-axis

As mentioned earlier, in this scenario, incremental voltage steps are applied along the d-axis, while the q-axis voltage reference is set to zero. At each step, the steady-state phase-A current is recorded. The voltage excitation continues until the sensed current reaches the nominal peak current of the load, a value typically provided in the datasheet of the load. The voltage corresponding to this current is identified as v_{test}^{max}, which serves as the maximum reference for the next stage of the procedure.

The next stage involves applying bidirectional symmetric voltage steps, starting from v_{test}^{max}, with the amplitude of the applied voltage decreasing step by step until it reaches a predefined minimum voltage. At each step, the applied voltage and the corresponding phase-A current are logged at steady state. The decrement in voltage amplitude is designed such that the step size is larger at higher voltages and progressively smaller at lower voltages, resulting in denser data points at lower voltage and current levels. This approach is particularly useful for accurately characterizing the behavior of the inverter in regions where nonlinearity effects are more evident. By focusing on better resolution in these critical areas, the resulting lookup table or model

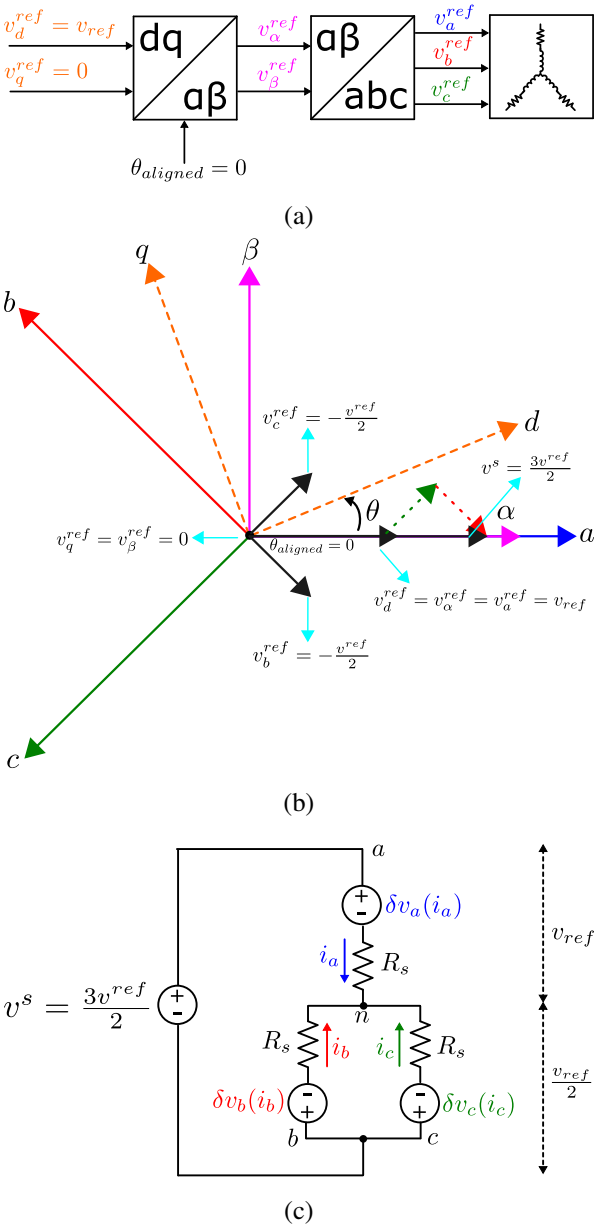

Figure 2.26: Inverter self-commissioning d-axis scenario: (a) Voltage excitation block diagram, (b) Voltage phasor diagram, (c) Equivalent circuit.

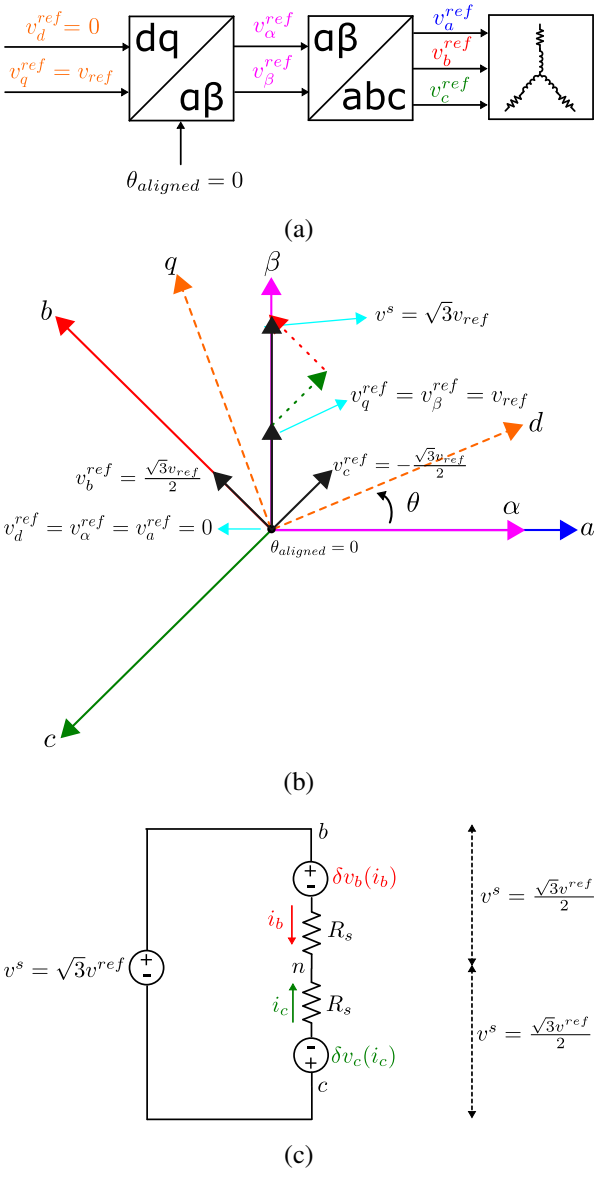

Figure 2.27: Inverter self-commissioning q-axis scenario: (a) Voltage excitation block diagram, (b) Voltage phasor diagram, (c) Equivalent circuit.

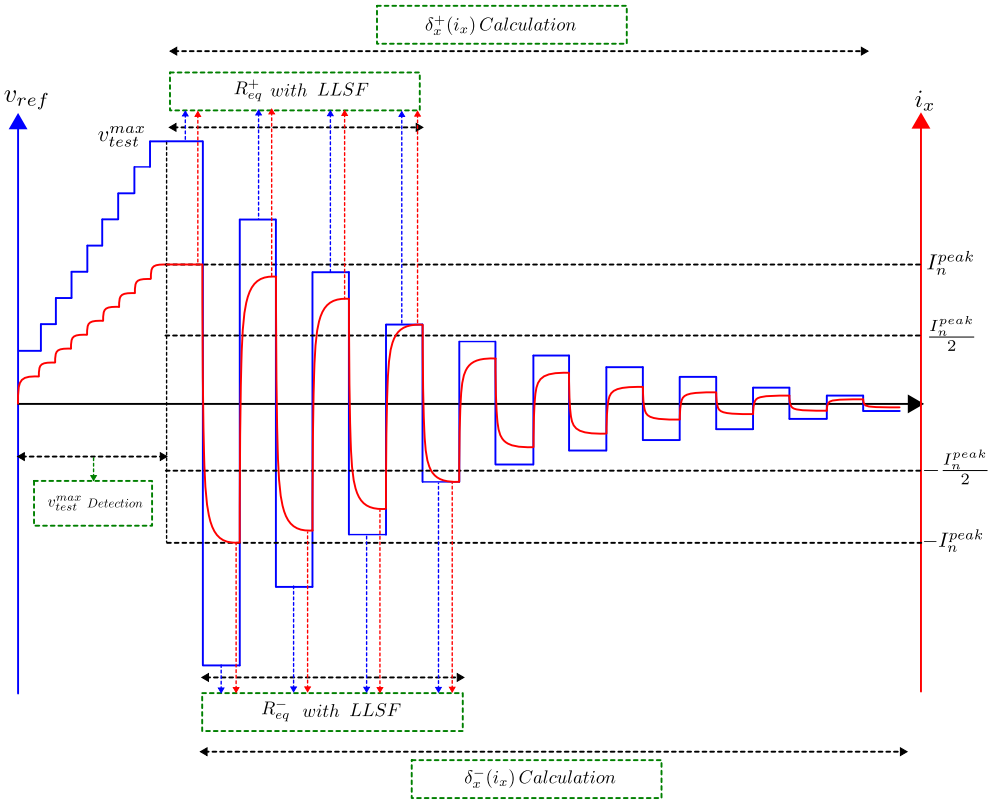

Figure 2.28: Proposed voltage injection procedure for the inverter self-commissioning.

for nonlinearity compensation becomes more precise, improving overall system performance and efficiency.

After completing the voltage excitation, the data processing phase begins. The logged data is analyzed separately for positive and negative current directions. For currents ranging from the nominal peak to half of the nominal peak, the total equivalent resistance R_{eq} is calculated for both the positive and negative current sides using linear least-squares fitting. This region has been chosen since it is a reliable range beyond the nonlinear region of the inverter and before possible load saturation.

The data is separated into two subsets: (i_+, v_+) for $(i > 0)$ and (i_-, v_-) for $(i < 0)$. For each subset, a linear least-squares fit is applied to the model $(\mathbf{V} = R_{eq}\mathbf{I} + c)$. The resistance R_{eq} is directly obtained as the slope m of the fit.

The least-squares solution for each region is:

$$\beta^{\pm} = (\mathbf{X}_{\pm}^{\top}\mathbf{X}_{\pm})^{-1}\mathbf{X}_{\pm}^{\top}\mathbf{V}_{\pm}, \tag{2.37}$$

where $\beta^{\pm} = \begin{bmatrix} c^{\pm} \\ R_{eq}^{\pm} \end{bmatrix}$ and $\mathbf{X} = [\mathbf{1} \quad \mathbf{I}]$, with $R_{eq}^{\pm}$ representing the resistance for the positive (i_+) and negative (i_-) current regions.

Considering the phasor diagram and equivalent circuit model in Fig. 2.26b and Fig. 2.26c, and utilizing Kirchhoff's Voltage Law (KVL), the phase voltage drop is calculated as:

$$\delta V_a^{\pm} = V_{an}^{\pm} - R_{eq}^{\pm} \cdot i_a^{\pm} \tag{2.38}$$

Here, i_a is the phase-A current, which is equal to the d-axis current due to the alignment at the zero position. Thus, the voltage drop along the d-axis is:

$$\delta V_d^{\pm} = V_{\pm}^{ref} - R_{eq}^{\pm} \cdot i_d^{\pm} = \delta V_a^{\pm}(i_a^{\pm}) \tag{2.39}$$

Finally, the computed voltage drops (δV_d) and their corresponding currents are used to create a lookup table for compensating the inverter voltage drop.

Second Scenario: Voltage Applied Along the q-axis

In this scenario, the procedure is similar, but the voltage is applied along the q-axis, with the d-axis voltage set to zero. The steady-state phase-B current is logged at each step. As before, the incremental voltage excitation continues until the sensed current reaches the nominal peak value, detecting v_{test}^{max}. Bidirectional symmetric voltages are then applied, decreasing step-by-step until the minimum voltage is reached, with the step size decreasing at lower voltages to capture more data points.

During data processing, the logged data for positive and negative currents is analyzed separately. The total equivalent resistance R_{eq} is calculated for both current directions using linear least-squares fitting, similar to the previous scenario. From the phasor diagram and the equivalent circuit in Fig. 2.27b and Fig. 2.27c, and using KVL, the phase voltage drop is computed as:

$$\delta V_b^{\pm} = V_{bn}^{\pm} - R_{eq}^{\pm} \cdot i_b^{\pm} \tag{2.40}$$

Here, i_b is the phase-B current, which corresponds to $\frac{\sqrt{3}}{2}$ times the q-axis current due to the alignment at the zero position. Thus, the voltage drop along the q-axis is:

$$\delta V_q^{\pm} = V_{\pm}^{ref} - R_{eq}^{\pm} \cdot i_q^{\pm} = \frac{2}{\sqrt{3}} \delta V_b^{\pm}(i_b^{\pm}) \tag{2.41}$$

This LUT is constructed by mapping the measured q-axis currents to their corresponding voltage drops, effectively characterizing the nonlinearity of the inverter across the operating range. To ensure that the rotor remains locked during the q-axis excitation, the procedure is performed at standstill, and mechanical constraints or active control strategies are applied as needed. Additionally, since torque is generated in the q-axis scenario, any unintended rotor movement is minimized by ensuring proper voltage control and maintaining the system in an open-loop condition by pre-alignment and locking the rotor before starting of the procedure. During operation, this LUT is accessed in real time to adjust the reference voltage commands sent to the inverter, compensating for the predicted voltage drop and improving overall system performance and accuracy.

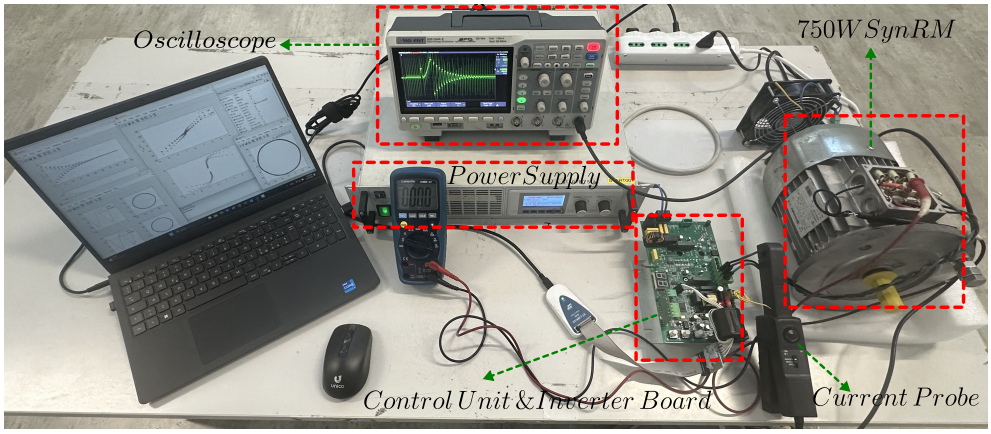

Figure 2.29: Experimental setup for inverter self-commissioning.

2.7 Experimental Implementation and Results

The experimental setup for the inverter nonlinearity self-commissioning is shown in Figure 2.29, utilizing a synchronous reluctance motor as the load, with specifications detailed in Table 2.2. The procedure was performed using the method described in [28] and two scenarios of the proposed method, d-axis excitation and q-axis excitation. The schematics of the inverter self-commissioning and verification procedure are illustrated in Figure 2.30 and Figure 2.31 for the typical and proposed method respectively. A commercial inverter and control board were employed, equipped with an STM32F303 microcontroller. The DC bus voltage was set to $V_{dc} = 320V$, the switching frequency to $f_{sw} = 10kHz$, and the dead time to $t_d = 1.69\,\mu s$, which were used in the drive process.

The sampling time $T_s = 200\,\mu s$ was set to be twice the switching time, ensuring accurate data acquisition and processing. While a $100\,\mu s$ sampling time was technically feasible for the self-commissioning process, the full setup, which includes real-time control algorithms with high computational demands, required $200\,\mu s$ to cover both data sampling and necessary calculations without missing data.

Table 2.2: Rated parameters of the SynRM.

Power P_N	750 W
Speed n_N	1500 rpm
Torque T_N	4.8 N m
Current I_N	2.2 A
Voltage U_N	400 V
Resistance R_s	6 Ω
Frequency f_N	50 Hz

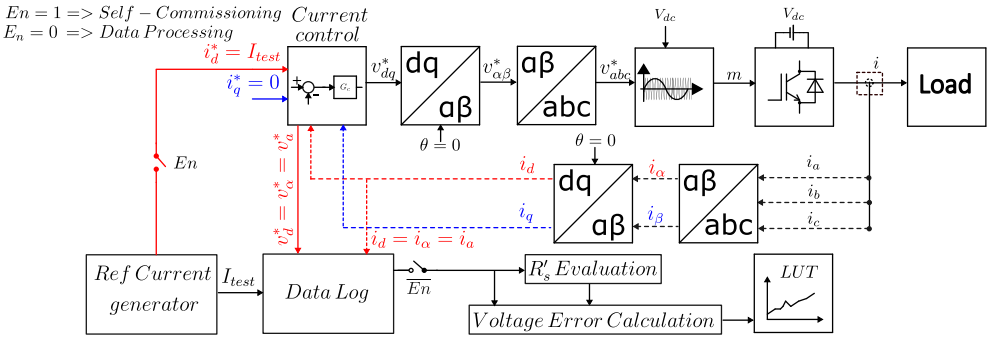

Figure 2.30: Equivalent control scheme for inverter self-commissioning by using the typical method.

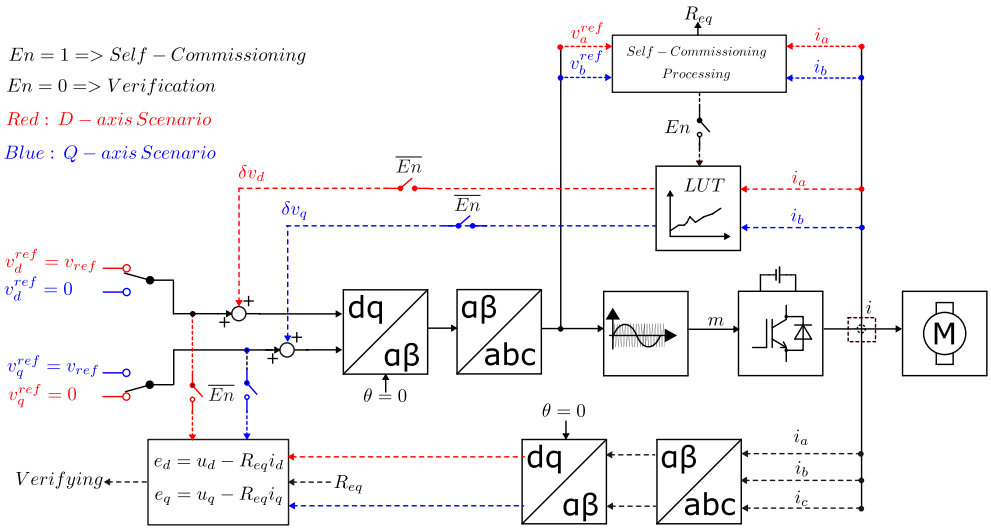

Figure 2.31: Proposed procedure for the inverter self-commissioning and verification.

Typical Inverter Self-commissioning Method Implementation

The typical self-commissioning method described in [28] was implemented experimentally as the procedure shown in Fig. 2.32a. The procedure consists of a rotor alignment stage followed by two main testing phases: resistance estimation and voltage drop characterization. All tests were performed at standstill to eliminate any back-EMF effects, ensuring accurate estimation of voltage drops due to resistance only. The test begins with a rotor parking step. A current equal to 50% of the nominal peak load current is injected through the current controller to align the rotor at the zero electrical position. This step ensures consistent initial conditions for all subsequent measurements.

In the first phase of testing, two step current levels (50% and 100% of the nominal peak load current) are applied sequentially. At each current level, the reference voltage produced by the current controller is recorded. Using these measurements, the total resistance of the motor is estimated based on (2.34). The calculated total resistance from this step is 6.04 Ω.

Next, a set of 16 gradually increasing current steps is applied to the motor via

the current controller. For each step, the corresponding reference voltage is recorded. By using the previously estimated total resistance and (2.36), the voltage drop is computed for each current value as shown in Fig. 2.32b. As seen in this figure, the voltage drop at high current levels deviates from the expected value for the given experimental setup. This is mainly due to the limited accuracy of the two-step current level method used for estimating the total resistance. These computed voltage drops are then used to generate a lookup table for voltage drop compensation.

To evaluate the accuracy of the voltage drop estimation, three distinct voltage levels are applied along both the d-axis and q-axis in separate tests as illustrated in Fig. 2.33a and Fig. 2.34a while the rotor remains stationary. The residual voltage is measured after compensation. As shown in Fig. 2.33b and Fig. 2.34b, the residual voltages are not zero, which indicates incomplete compensation. Since the rotor is at standstill and no back-EMF should exist, the residual voltages ideally should be zero.

Proposed Inverter Self-commissioning Method Implementation

In the proposed method implementation, during the first part of the procedure to detect v_{test}^{max}, the voltage amplitude was incremented in steps of 2 V, with a time interval of $500\,ms$ between each step. This approach ensured the identification of the maximum test voltage without exceeding the operational limits of the system.

For the second part, 23 steps were selected for both positive and negative voltage excitation. Starting from v_{test}^{max}, the voltage decreased to a minimum of $1\,V$. The amplitude of each voltage step followed a geometric progression, calculated as:

$$ratio = \left(\frac{v_{test}^{max}}{v_{test}^{min}}\right)^{\left(\frac{1}{23-1}\right)}$$

Each step lasted one second, allowing the system to reach steady-state conditions before transitioning to the next step.

After completing the excitation procedure and logging voltage and current data, the total equivalent resistance calculation and lookup table generation were carried out. Finally, the verification test was performed, involving the injection of three-step voltage signals into the d-axis or q-axis, including the voltage drop compensation

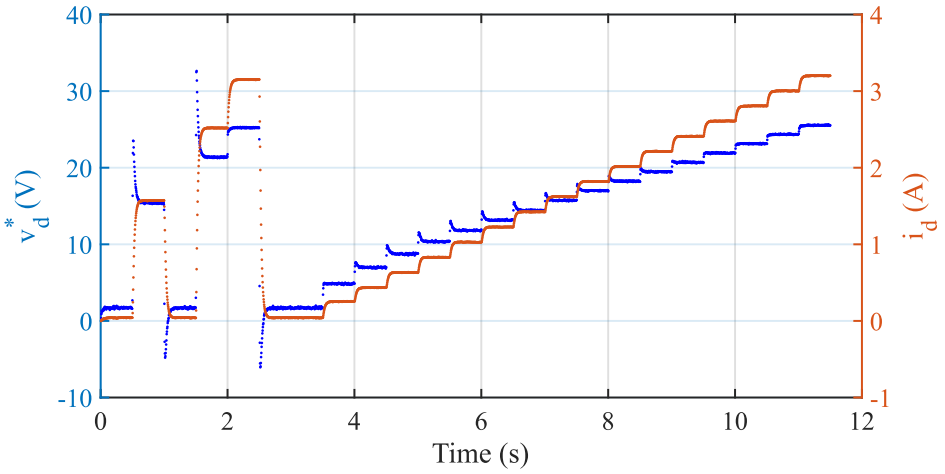

(a)

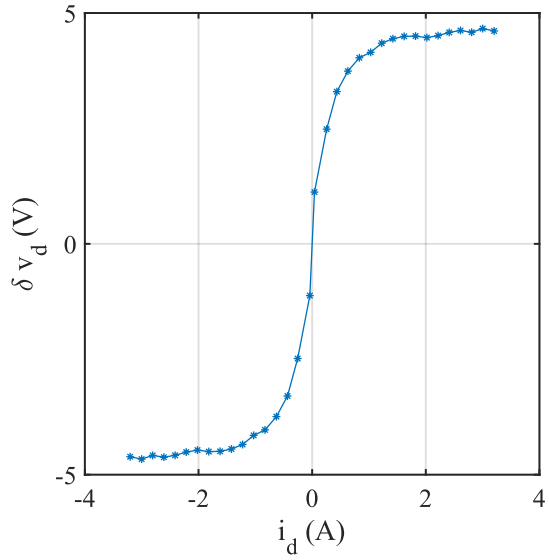

(b)

Figure 2.32: Inverter self-commissioning by using the typical method for the *d*-axis: (a) Reference voltage and the corresponding controlled current, (b) Estimated voltage drop.

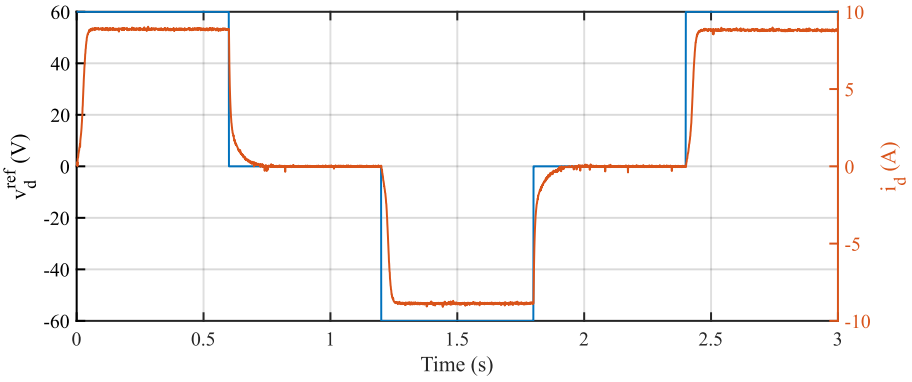

(a)

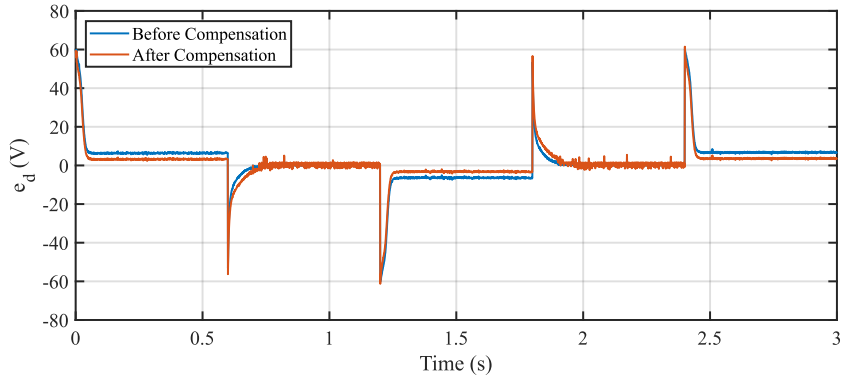

(b)

Figure 2.33: Precision verification of the typical method for the *d*-axis scenario: (a) Three-step voltage excitation and the corresponding output current for the *d*-axis voltage drop verification, (b) Effect of compensation using the typical method.

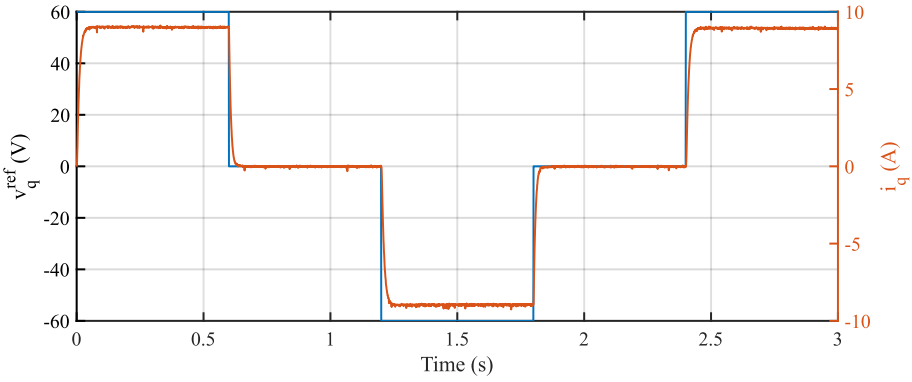

(a)

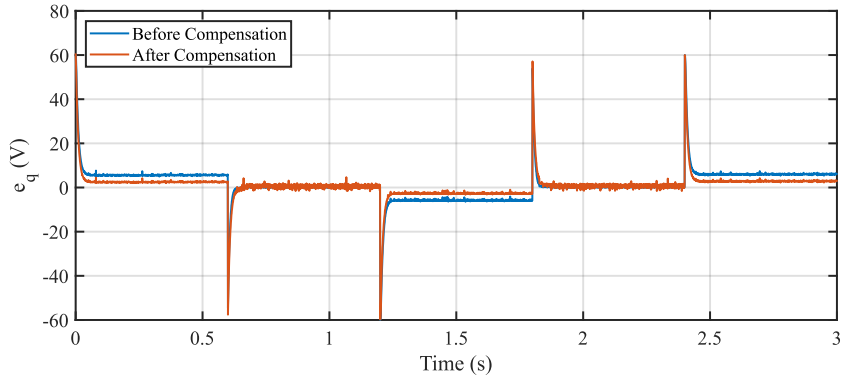

(b)

Figure 2.34: Precision verification of the typical method for the q-axis scenario: (a) Three-step voltage excitation and the corresponding output current for the q-axis voltage drop verification, (b) Effect of compensation using the typical method.

in the excitation voltage. Since the injected voltage is DC, and the load is resistive under steady-state conditions with the machine at standstill, motion-induced back-EMF is not expected. However, any residual voltage deviations due to uncompensated inverter nonlinearity could replicate like back-EMF effects. Successful compensation was confirmed by the absence of unexpected voltage deviations in the logged data, validating the accuracy of the lookup table and the overall procedure.

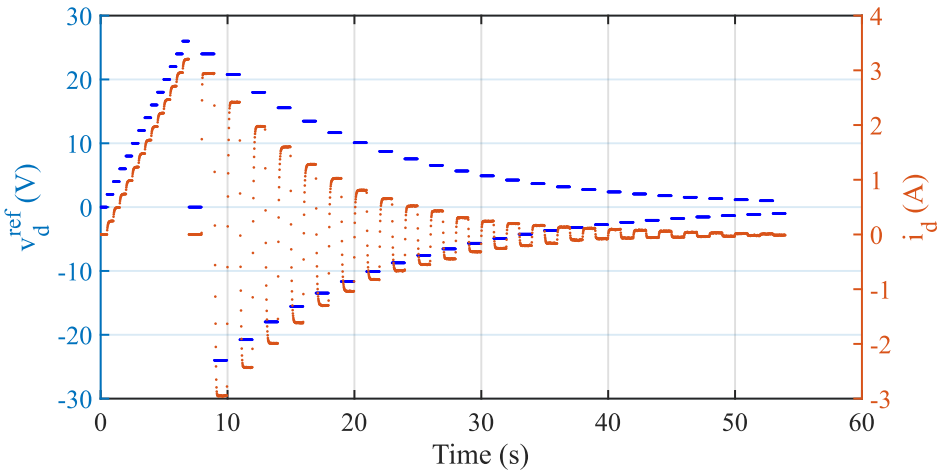

Figure 2.35: Reference voltage and the corresponding measured current during the *d*-axis self-commissioning.

The reference voltage and measured current for the first scenario are illustrated in Figure 2.35. As mentioned, 23 steps of voltage reference were applied to the *d*-axis, and the corresponding phase current was measured and converted into *d*-axis current. The neutral point of the motor was accessible in our setup, allowing the phase voltages to be measured directly at the motor terminal to the neutral point using a digital multimeter. Fig. 2.36a shows the difference between the applied voltage and the measured voltage. However, according to Fig. 2.36b, the estimated voltage drop does not match the measured voltage drop. This difference is caused by the limitations of the measurement device, a standard digital multimeter, which is not designed for high-speed or highly precise voltage measurements required for this

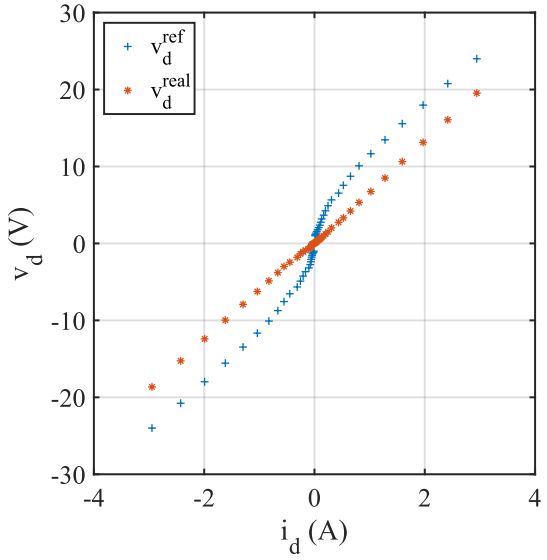

(a)

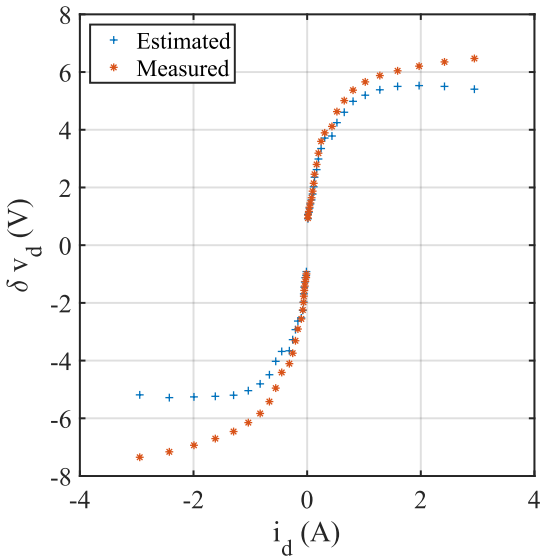

(b)

Figure 2.36: Comparison between self-commissioning-based voltage drop estimation and direct voltage measurement using a multimeter for the *d*-axis scenario: (a) Reference and measured voltage, (b) Estimated and measured voltage drop.

application.

Despite these limitations, the multimeter was chosen because it was available for initial experimentation and provided a basic comparison to identify trends in the voltage drop. Recognizing these constraints, a more reliable verification method was implemented by injecting a three-level voltage and calculating the residual voltage before and after compensating the reference voltage.

As mentioned earlier, considering that the rotor is at standstill, there should not be any back-EMF in the motor. Thus, the residual voltage after deducting the resistive drop is related to the inverter nonlinearity. It should be noted that the total equivalent resistance measured in this scenario is $(R_{eq}^{+}, R_{eq}^{-}) = (6.32\,\Omega, 6.38\,\Omega)$. These values were obtained using the reference voltage and current measurements acquired by the shunt current sensor and an STM32 microcontroller ADC. Given the ADC resolution and measurement uncertainties, the resistance values are reported with a precision that aligns with the effective accuracy of the measurement system. Fig. 2.37a and Fig. 2.37b show the results of excitation in the d-axis, before and after compensation. It is clear that compensation has a positive effect in reducing voltage distortion, since after compensation, no residual voltage is observed.

Similarly, the reference voltage and measured current for the second scenario are illustrated in Figure 2.38. A 23-step bidirectional voltage sequence was applied to the q-axis after detecting the maximum test voltage in the previous step of self-commissioning. Voltage-current pairs were logged for each step, and the total equivalent resistance was processed. The estimated equivalent resistance in this scenario was $(R_{eq}^{+}, R_{eq}^{-}) = (6.21\Omega, 6.25\Omega)$.

For this scenario, the direct motor phase-to-neutral voltage was also measured with a multimeter and compared in Fig. 2.39b. The difference in results is related to the same reason mentioned in the previous scenario. The same verification method was also applied to the q-axis. Fig. 2.40b shows the result of excitation in the q-axis, before and after compensation. It is clear that the compensation has a positive effect in reducing voltage distortion, since after compensation, no residual voltage is observed.

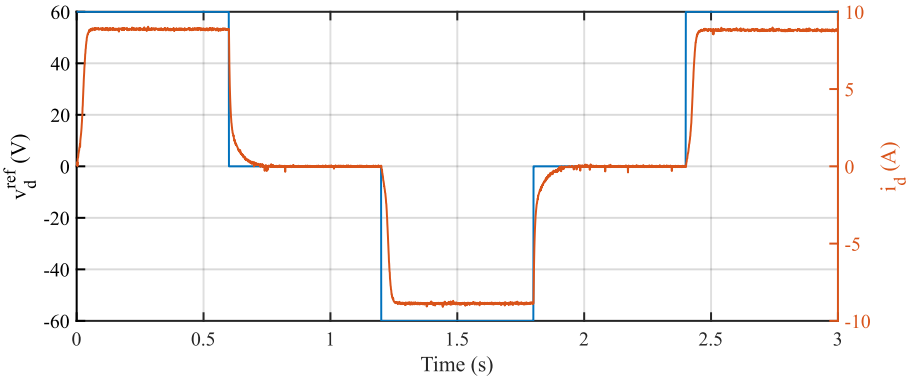

(a)

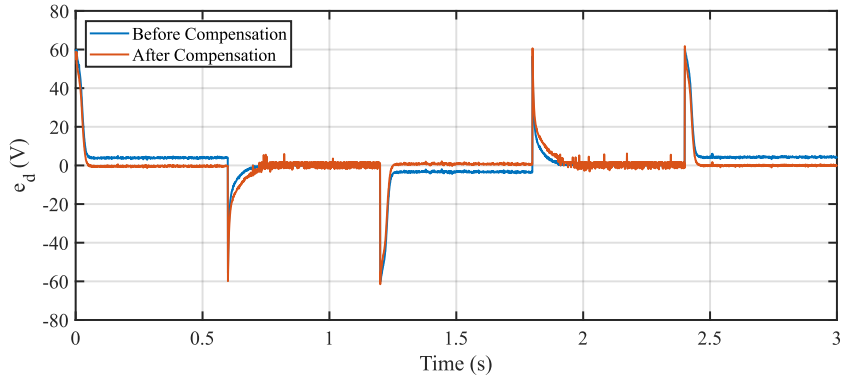

(b)

Figure 2.37: Precision verification of the proposed method for the d-axis scenario: (a) Three step voltage excitation and according output current for d-axis voltage drop verification, (b) Effect of compensation using proposed method.

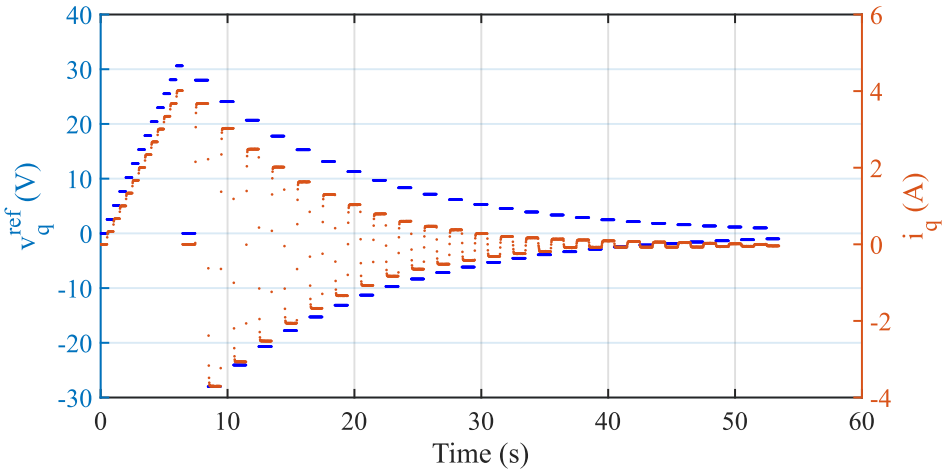

Figure 2.38: Reference voltage and the corresponding measured current during the q-axis self-commissioning.

Comparison of the Experimental Results

This section presents a comparative analysis of the experimental results obtained before and after applying compensation techniques using both the typical and the proposed inverter self-commissioning methods. The performance is evaluated on both the d-axis and q-axis voltage errors (e_d and e_q), as shown in Fig. 2.41a and Fig. 2.41b, respectively. The numerical metrics used for performance evaluation include Integral Absolute Error (IAE), Integral Squared Error (ISE), Maximum Absolute Error (MAE), Root Mean Square Error (RMSE), and the Maximum Error.

The plots indicate that before compensation, the system experiences significant deviations from the expected zero voltage. When the typical compensation method is applied, an improvement is observed. However, the residual errors still persist. In contrast, the proposed compensation method yields a significant improvement in performance by minimizing steady-state errors more effectively.

Table 2.3 summarizes the quantitative results for both axes. As seen, the proposed method achieves considerable reductions across all error metrics compared to the

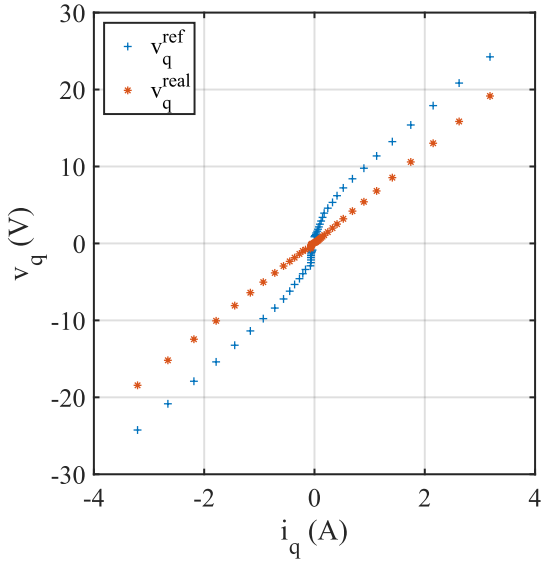

(a)

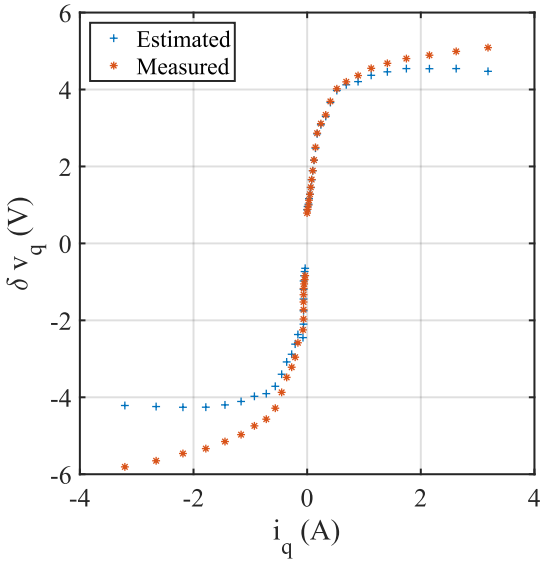

(b)

Figure 2.39: Comparison between self-commissioning-based voltage drop estimation and direct voltage measurement using a multimeter for the q-axis scenario: (a) Reference and measured voltage, (b) Estimated and measured voltage drop.

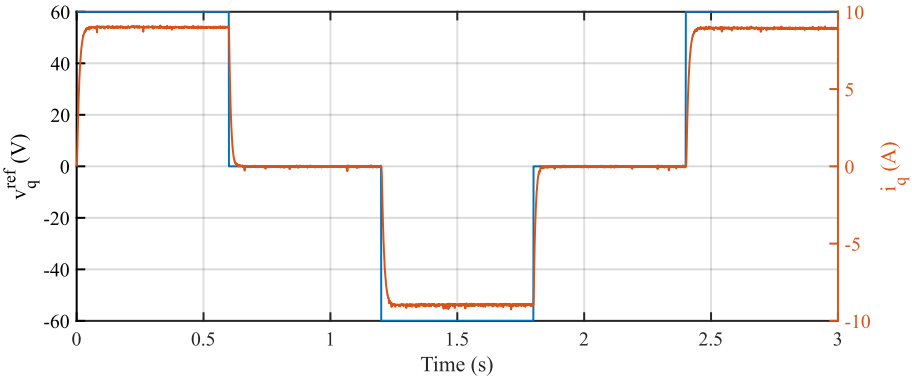

(a)

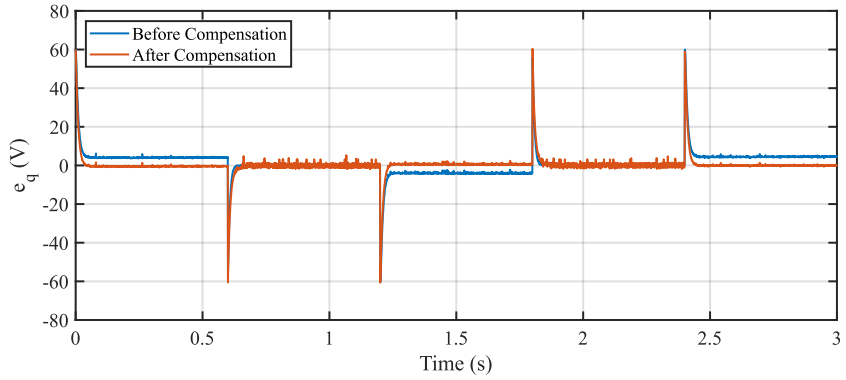

(b)

Figure 2.40: Precision verification of the proposed method for the q-axis scenario: (a) Three-step voltage excitation and the corresponding output current for the q-axis voltage drop verification, (b) Effect of compensation using the proposed method.

typical method. For instance, the IAE on the d-axis decreases from 0.0205 $V.s$ to 0.0046 $V.s$, and on the q-axis from 0.0149 $V.s$ to 0.0023 $V.s$. Similarly, all other metrics reflect the improved accuracy and effectiveness of the proposed approach.

Table 2.3: Comparison of the result from typical and proposed inverter self-commissioning methods on d-axis and q-axis.

	Method	**IAE** (V.s)	**ISE** (V^2.s)	**MAE** (V)	**RMSE** (V)	**Max Error** (V)
d-axis	Typical	0.0205	0.0644	2.2635	2.3005	2.5588
	Proposed	0.0046	0.0038	0.5153	0.5556	0.8242
q-axis	Typical	0.0149	0.0363	1.9443	1.9684	2.1677
	Proposed	0.0023	0.0009	0.2805	0.3048	0.4783

2.7.1 Parameter Estimation

In this section, the inverter parameters are estimated using optimal model fitting, considering the reduced model in (2.30). The parameters t_d, V_{dc}, and T_{sw} are known, while $v_{on,d}$, $v_{on,t}$, $r_{on,d}$, $r_{on,t}$, C_{out}, and I_{cr} are unknown.

Although it is theoretically possible to collect multiple samples to improve fitting accuracy, the model parameters are reduced to ensure a unique and well-conditioned fitting process. Specifically, the critical current I_{cr} is approximately derived from C_{out} using the relationship:

$$I_{cr} = \frac{2C_{out}V_{dc}}{t_d}$$

This ensures a physically consistent dependency between C_{out} and I_{cr}. This approach reduces the number of unknown parameters from six to five, simplifying the fitting process and avoiding excessive model complexity, especially in scenarios where data collection may be limited or noisy.

Additionally, combining voltage drop terms and resistance terms further reduces the number of unknown parameters to three:

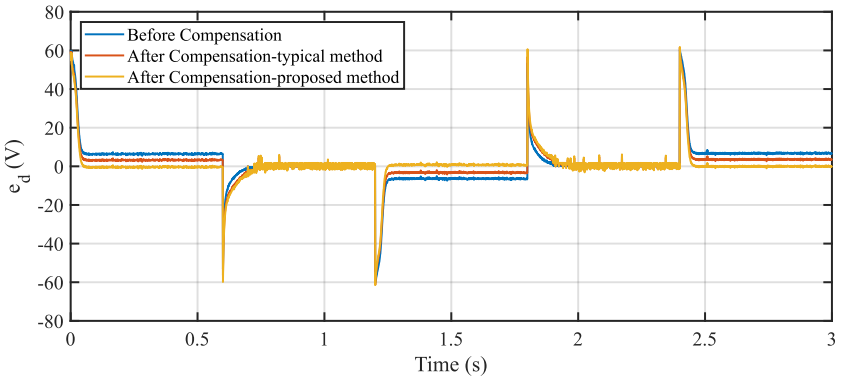

(a)

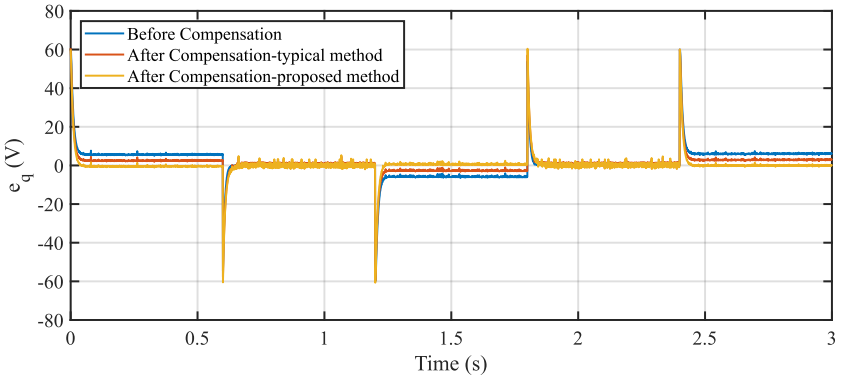

(b)

Figure 2.41: Voltage error comparison before and after compensation between typical and proposed self-commissioning methods: (a) *D*-axis voltage error, (b) *Q*-axis voltage error.

- v_{td}: The combined voltage drop term, defined as $v_{td} = \frac{1}{2}(v_{on,d} + v_{on,t})$.
- r_{td}: The combined resistance term, defined as $r_{td} = \frac{1}{2}(r_{on,d} + r_{on,t})$.

The optimization process aims to determine the parameters v_{td}, r_{td}, and C_{out} such that the predicted voltage drop δv_{xn} best matches the experimental data. The optimization problem is solved using a hybrid approach that combines Bayesian Optimization for global exploration and Sequential Quadratic Programming (SQP) for local refinement.

This hybrid method ensures a balance between global exploration of the parameter space, avoiding local minimum points, and fine-tuning the solution for high accuracy.

Cost Function Formulation

The cost function is designed to minimize the mean squared error (MSE) between the predicted and measured voltage drop, while enforcing physical constraints and avoiding boundary convergence. The total cost function is formulated as:

$$\text{Cost} = \text{MSE} + \lambda_1 \cdot \text{Regularization} + \lambda_2 \cdot \text{Boundary Penalty} + \lambda_3 \cdot \text{Continuity Penalty}.$$

The MSE term evaluates the goodness-of-fit between the predicted and experimental voltage drop:

$$\text{MSE} = \frac{1}{N} \sum_{i=1}^{N} \left(\delta v_{\text{pred},i} - \delta v_{\text{exp},i} \right)^2, \tag{2.42}$$

where $\delta v_{\text{pred},i}$ is the predicted voltage drop, $\delta v_{\text{exp},i}$ is the measured voltage drop, and N is the number of data points. The regularization term ensures the parameters v_{td} and r_{td} stay close to their expected ranges, avoiding extreme values:

$$\text{Regularization} = (r_{td} - r_{td,\text{center}})^2 + (v_{td} - v_{td,\text{center}})^2, \tag{2.43}$$

where $r_{td,\text{center}}$ and $v_{td,\text{center}}$ are the midpoints of their respective feasible ranges. A boundary penalty discourages parameters from converging at the edges of their

feasible ranges:

$$\text{Boundary Penalty} = \begin{cases} \infty & \text{if } r_{td} < r_{td,\min} \text{ or } r_{td} > r_{td,\max} \\ \infty & \text{if } v_{td} < v_{th,\min} \text{ or } v_{td} > v_{th,\max} \\ 0 & \text{otherwise.} \end{cases} \tag{2.44}$$

The continuity penalty enforces smoothness in the voltage drop model at the critical current I_{cr}, ensuring a physically realistic transition between the two regions of the voltage drop equation. In an ideal case, the voltage drop function should be mathematically continuous at I_{cr}. However, in our formulation, a discontinuity arises due to the fact that the model is based on experimental recorded data, and separate fitting procedures are used for different current regions. This discontinuity results from a piecewise representation of voltage drop behavior, which does not guarantee a smooth transition at I_{cr}. To remove this, we introduce a continuity penalty, defined as:

$$\text{Continuity Penalty} = \left(\delta v_{\text{model}}(I_{cr}) - \delta v_{\text{model}}(I_{cr} - \varepsilon)\right)^2, \tag{2.45}$$

where ε is a small perturbation used to evaluate continuity at I_{cr}. This penalty forces the transition to be smoother by minimizing sudden changes between the two regions, ensuring that the model remains both physically valid and numerically stable.

Optimization Workflow

The optimization is performed in two stages:

1. **Global Search with Bayesian Optimization:** Bayesian Optimization explores the parameter space globally using probabilistic models to identify regions of interest. This ensures that the optimizer does not get trapped in the local minimum point and provides a good starting point for the next stage.

2. **Local Refinement with SQP:** Sequential Quadratic Programming (SQP) refines the parameters obtained from Bayesian Optimization. SQP uses gradient-based methods to fine-tune the solution, ensuring high accuracy and adherence to constraints.

The optimization process is implemented in MATLAB, using the `bayesopt` function for Bayesian Optimization and `fmincon` for SQP refinement. During each iteration, the parameter values (v_{td}, r_{td}, C_{out}), the cost, and the predicted voltage drop are logged. Figure 2.42 illustrates the optimization iteration and according optimal fitted model to the voltage drop data. The final estimated parameters, real measurement of the parameters and datasheet values have been compared in Table 2.4. According to the result, this methodology ensures a balance between fitting accuracy and the reality of the physical model, providing a robust model for the voltage drop behavior.

Table 2.4: Estimated parameters of the inverter.

Parameter	**Estimated** ($i_x > 0$)	**Estimated** ($i_x < 0$)	**Average**	**Measured**	**Datasheet**
v_{td} (V)	0.85	0.84	0.85	0.66	0.72
r_{td} (Ω)	0.06	0.06	0.06	0.05	0.08
C_{out} (nF)	0.63	1.0	0.82	-	-
I_{cr} (A)	0.24	0.38	0.31	-	-

2.8 Chapter Summary

In this chapter, the nonlinearities of a three-phase two-level inverter have been reviewed, modeled and analyzed. Various sources of voltage distortion, such as dead-time effects, switching device characteristics, and parasitic capacitance, have been studied in detail, highlighting their effects on inverter performance.

A novel self-commissioning procedure for inverter voltage drop compensation has been proposed, employing a lookup table-based compensation strategy to remove voltage distortion. This method provides a practical and effective solution for addressing inverter nonlinearities without requiring extensive prior knowledge of the inverter parameters.

The proposed procedure has been experimentally validated and compared to the typical lookup table based method, demonstrating its ability to enhance performance

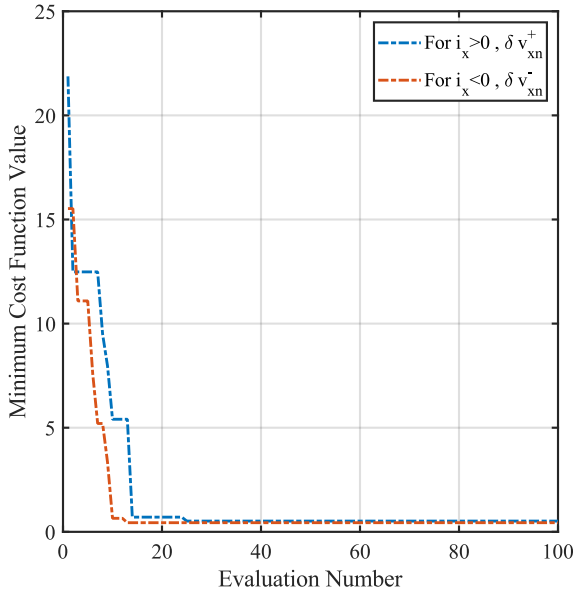

(a)

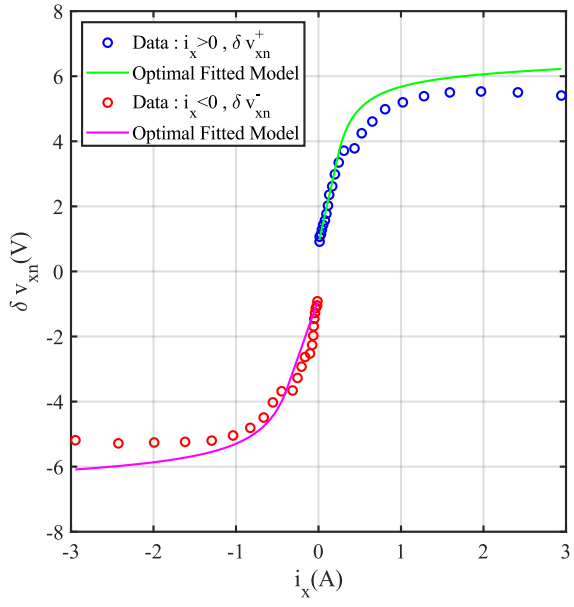

(b)

Figure 2.42: Estimation of inverter parameters using optimal fitting procedure: (b) Local and global minimization process for best fitting, (b) Optimal model fitted to the voltage drop for positive and negative current region.

by accurately compensating for the effects of voltage distortion. Additionally, a hybrid optimization method has been employed to estimate the equivalent parameters of a simplified inverter nonlinearity model. This method effectively combines parameter fitting and search techniques, providing an accurate representation of the inverter behavior and enabling better model tuning.

The findings and methodologies presented in this chapter offer a robust framework for understanding and addressing inverter nonlinearities, making the performance improvement possible in motor drive applications.

Chapter 3

Synchronous Reluctance Motor Self-Commissioning

3.1 State of the Art

The modeling and self-commissioning of SynRMs have had significant improvements over the past decade, with numerous techniques proposed to accurately identify the magnetic characteristics and parameters of the motor without requiring extensive manual calibration. Self-commissioning methods aim to simplify the commissioning process by estimating the important motor parameters such as inductance, resistance, and magnetic flux linkage, while compensating for phenomena like saturation and inverter nonlinearities. In this review, we categorize self-commissioning techniques into three primary methods: standstill flux mapping, rotor-lock and rotor-kinetic methods, and advanced modeling approaches including neural networks and coenergy models. Standstill flux mapping involves applying specific voltage or current excitations to the stator windings while the rotor remains stationary and free to align itself naturally. This method captures the magnetic characteristics of the motor across a range of operating points without requiring external constraints on the rotor. In contrast, rotor-locked methods physically lock the rotor in a fixed position to prevent any movement during excitation. This allows for precise parameter measure-

ments under controlled rotor alignment, making it particularly useful for analyzing the anisotropic properties of the rotor. In the following, recent developments of each category are discussed with references.

3.1.1 Standstill Flux Mapping Techniques

Standstill flux mapping methods rely on the stationary condition of the rotor to identify the flux linkage and inductance characteristics of SynRMs. These methods are particularly useful for flux map identification, as they do not require rotor motion. Hinkkanen et al. [42, 43] proposed a sensorless standstill self-commissioning method based on flux map identification, utilizing linear least squares (LLS) to accurately capture the flux saturation characteristics. Similarly, Peretti et al. [44] introduced a quasi-standstill method, enabling rapid torque oscillations to estimate the flux linkage curves effectively. Ortombina et al. [45] employed a coenergy model at standstill, which provides an alternative approach to identifying magnetic maps without requiring high-frequency injections.

Current injection-based methods at standstill involve injecting controlled currents into the stator windings to create specific flux conditions, allowing the estimation of the inductance and magnetic saturation characteristics in real-time. Tan et al. [46] developed a current injection method that considers cross-saturation effects, enhancing self-commissioning accuracy for SynRMs. Wiedemann and Kennel [47] further explored encoderless self-commissioning techniques at standstill, utilizing flux-linkage maps and machine learning models to provide accurate parameter identification. This method compensates for nonlinear magnetic characteristics through iterative adaptation, as outlined in Pescetto and Pellegrino's high-frequency voltage injection work [48].

3.1.2 Rotor-Lock and Rotor-Kinetic Methods

Rotor-lock methods temporarily fix the rotor to simplify parameter identification, often allowing for a robust self-commissioning process without the need for complex motion control. The rotor is typically fixed using mechanical forces, such as clamp-

ing devices or fixtures that hold the rotor in a specific position. Varatharajan et al. [49] proposed a rotor-locked self-commissioning approach that identifies the magnetic model parameters, even accommodating cross-saturation. Expanding on this, Varatharajan et al. [50] explored a kinetic-rotor self-commissioning approach, where the motor undergoes controlled rotational movements to adaptively estimate the inductance and flux linkage with real-time magnetic model identification. Truong et al. [51] presented a capacitor discharge method for inductance identification using rotor lock, simplifying the magnetic model identification by utilizing a controlled discharge cycle to measure the response accurately.

3.1.3 Advanced Modeling Approaches

Advanced modeling techniques utilize artificial neural networks, coenergy methods, and parameter compensation algorithms to enhance the accuracy and robustness of self-commissioning. Bao et al. [52] introduced a neural network model for flux saturation modeling, which provides an efficient parameter identification method even under complex saturation effects. Ortombina et al. [53] utilized a radial basis function network to account for speed and load transients, thus improving the robustness of the model under dynamic conditions. Varvolik et al. [54] proposed a rapid experimental approach for magnetic model identification, enabling faster commissioning without sacrificing accuracy. Zhong et al. [55] addressed inverter nonlinearity and resistance error compensation in their self-commissioning technique, which further improves the precision of SynRM models at standstill by correcting for systematic errors in the inverter output.

Credo et al. [56] proposed a unified self-commissioning approach, combining finite element simulations with experimental measurements to provide an integrated solution that covers inductance estimation, initial position detection, and resistance calibration. This approach is suitable for scenarios requiring high accuracy and provides a comprehensive model that can adapt to both stationary and dynamic operating conditions.

Each category offers distinct advantages and trade-offs depending on the requirements for applications, such as accuracy, computation time, and adaptation to dy-

namic load conditions. Standstill methods are widely used for their simplicity and direct approach to flux mapping, while rotor-free and rotor-lock methods allow more dynamic estimation. Advanced modeling techniques, including neural networks and compensation algorithms, provide enhanced flexibility and accuracy by learning nonlinear magnetic behaviors and adapting to varying operating conditions in real time. For instance, neural networks can model complex flux saturation effects and cross-saturation interactions without requiring explicit mathematical formulations, which are often challenging to derive analytically. This data-driven capability makes them well-suited for capturing dynamic changes in the characteristics of the motor across a wide operating range. Compared to traditional look-up table or physics-based approaches, these models can generalize better to reduce the need for extensive offline calibration. Additionally, compensation algorithms such as those correcting for inverter nonlinearities or resistance drift, further improve model precision, especially under high-load or temperature-varying conditions. Thus, these advanced methods are particularly advantageous in applications where environmental or operational variability would compromise the performance of more static modeling techniques.

3.2 SynRM Nonlinear Saturated Model

A SynRM is a type of electric motor that operates based on the magnetic reluctance principle. SynRMs do not have permanent magnets or windings on the rotor, and the torque is generated by the difference in the reluctance between the direct (d) and quadrature (q) axes. In this section, we develop a mathematical model for the SynRM, starting from a nonlinear, saturated model and progressing to a simplified model at standstill needed for parameter identification.

3.2.1 α-β Model Representation

The modeling of SynRMs under saturation involves nonlinear inductance that varies with both the current and magnetic field intensity. The voltage equations for a SynRM in the $\alpha\beta$ reference frame, accounting for magnetic saturation, are:

$$\begin{aligned} v_\alpha &= R_s i_\alpha + \frac{d\psi_\alpha}{dt}, \\ v_\beta &= R_s i_\beta + \frac{d\psi_\beta}{dt}, \end{aligned} \tag{3.1}$$

where:

- v_α, v_β: Voltages in the α-β axes,
- R_s: Stator resistance,
- i_α, i_β: Currents in the α-β axes,
- ψ_α, ψ_β: Flux linkages in the α-β axes.

3.2.2 d-q Model Representation

The dq-model is essential for analyzing SynRMs under dynamic conditions. Transforming the $\alpha\beta$ quantities to the dq reference frame rotating at the electrical angular velocity ω, the voltage equations become:

$$\begin{aligned} v_d &= R_s i_d + \frac{d\psi_d}{dt} - \omega\psi_q, \\ v_q &= R_s i_q + \frac{d\psi_q}{dt} + \omega\psi_d. \end{aligned} \tag{3.2}$$

The flux linkages ψ_d and ψ_q can be expressed in terms of the nonlinear inductances, which depend on the current due to saturation. In the simplified decoupled model, the d- and q-axis inductances are assumed to depend only on their respective axis currents:

$$\begin{aligned} \psi_d &= L_d(i_d) \cdot i_d, \\ \psi_q &= L_q(i_q) \cdot i_q. \end{aligned} \tag{3.3}$$

Here:

- $L_d(i_d)$: Direct-axis inductance as a function of i_d,
- $L_q(i_q)$: Quadrature-axis inductance as a function of i_q.

However, in practical SynRMs operating under significant saturation, cross-saturation effects may occur, leading to coupled inductance behavior, where L_d and L_q are functions of both i_d and i_q. In such cases, a more accurate model would use:

$$\begin{aligned} \psi_d &= L_d(i_d, i_q) \cdot i_d, \\ \psi_q &= L_q(i_d, i_q) \cdot i_q. \end{aligned} \tag{3.4}$$

The nonlinear nature of L_d and L_q in (3.4) represents the cross saturation effect as well, which can be captured by experimental fitting or lookup tables derived from identification methods. However, in this study, the simplified decoupled expressions for ψ_d and ψ_q in (3.3) have been used. So, we can rewrite the voltage equations as:

$$\begin{aligned} v_d &= R_s i_d + L_d(i_d)\frac{di_d}{dt} + i_d\frac{dL_d(i_d)}{dt} - \omega L_q(i_q) i_q, \\ v_q &= R_s i_q + L_q(i_q)\frac{di_q}{dt} + i_q\frac{dL_q(i_q)}{dt} + \omega L_d(i_d) i_d. \end{aligned} \tag{3.5}$$

The torque T_e generated by the SynRM is given by:

$$T_e = \frac{3}{2} p(L_d(i_d) - L_q(i_q)) i_d i_q, \tag{3.6}$$

where p is the number of pole pairs.

3.2.3 Standstill Model Representation

At standstill, the angular velocity ω is zero, simplifying (3.5) to:

$$\begin{aligned} v_d &= R_s i_d + L_d(i_d)\frac{di_d}{dt} + i_d\frac{dL_d(i_d)}{dt}, \\ v_q &= R_s i_q + L_q(i_q)\frac{di_q}{dt} + i_q\frac{dL_q(i_q)}{dt}. \end{aligned} \tag{3.7}$$

The standstill model is particularly useful for parameter identification and initial commissioning because the stationary rotor eliminates back EMF and mechanical dynamics, simplifying the voltage equations and enabling more accurate extraction of electrical parameters under controlled conditions.

3.3 Self-commissioning Methods Study

In this section, two methods of SynRM self-commissioning are studied and simulated in MATLAB to compare their results with the proposed method later: (1) the DC-biased high-frequency signal injection (HFSI) method, originally developed for PMSMs and IMs [57, 58] and adapted for SynRMs, and (2) the bipolar voltage injection method at standstill [42, 43, 59].

These two methods were selected because they represent two widely adopted approaches in the literature for rotor position estimation and parameter identification under standstill conditions. The HFSI method provides high estimation accuracy even under saturation and is commonly used in sensorless control schemes, while the bipolar voltage injection method is relatively simple and effective for flux map extraction without requiring rotor motion. Their contrasting characteristics make them suitable benchmarks for evaluating the performance and robustness of the proposed method.

3.3.1 DC-biased HFSI Method

In order to extract the inductance map, a signal injection procedure similar to that in [57], but without a current controller, has been implemented separately for each axis. This is based on the working points illustrated in Fig. 3.1a and Fig. 3.1b, and the procedure block diagram shown in Figure 3.2. The voltage excitation described in [57], which operates through a current controller, may cause current spikes during transitions between working points. This can lead to issues in both motor safety and data processing. In contrast, the proposed open-loop voltage excitation method avoids these unwanted phenomena.

Furthermore, using this method makes it possible to implement the procedure in a continuous manner, allowing smooth transitions between working points and enabling faster identification. In this procedure, different DC voltage levels ($v^{dc}i$), superimposed with a fixed-amplitude (v_{inj}) and fixed-frequency (f_{inj}) sinusoidal signal, are applied to the axis under test, while zero voltage is applied to the other axis. The incremental inductance values are calculated from the impedance at the injected

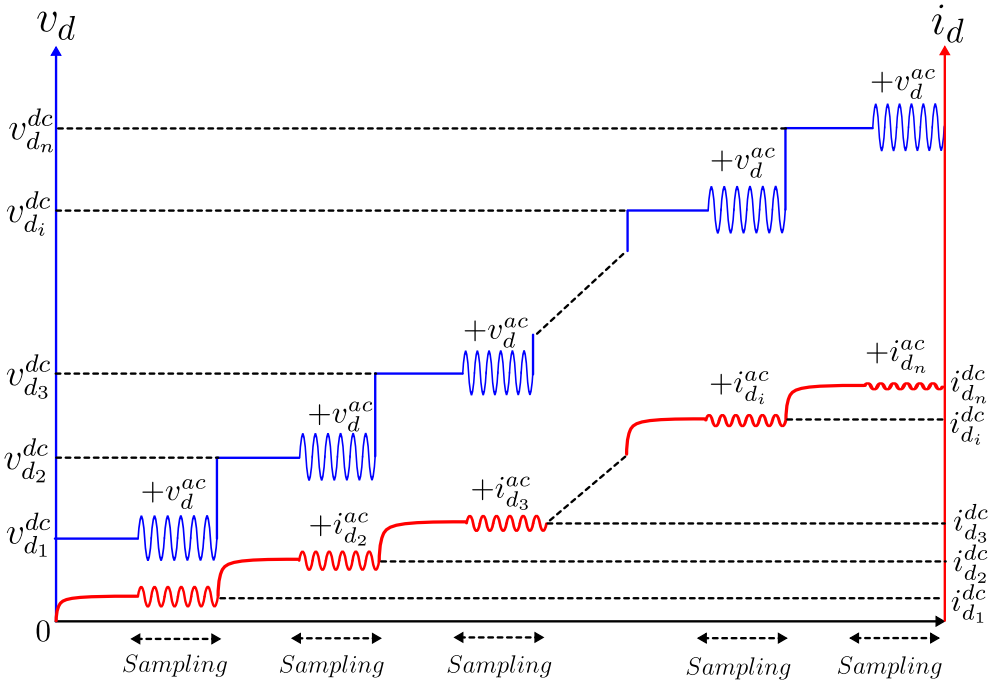

(a)

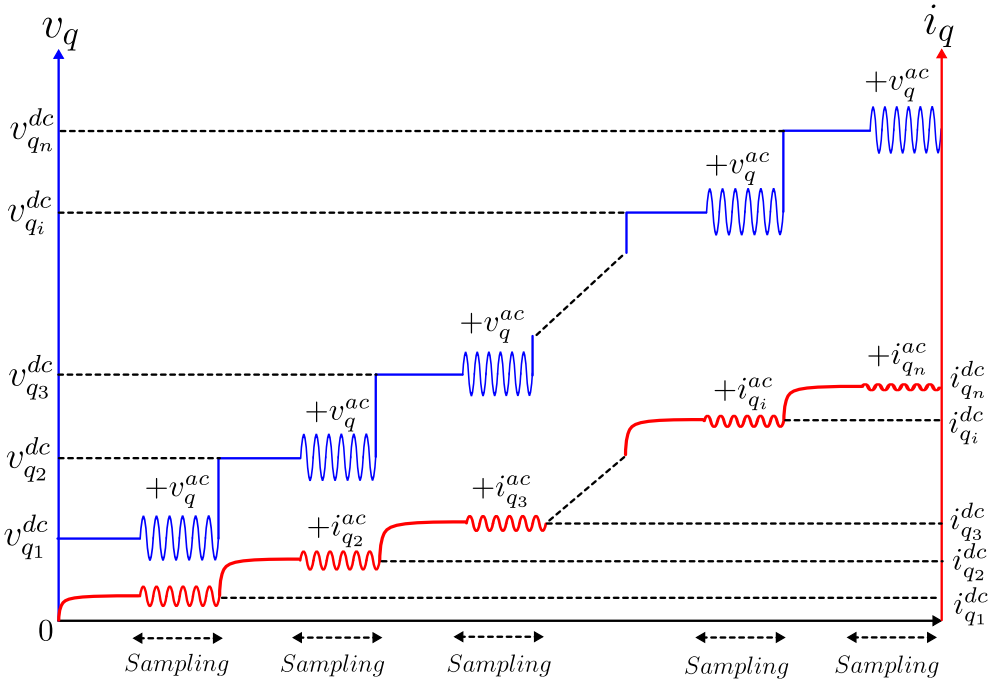

(b)

Figure 3.1: DC-biased high-frequency signal injection method: (a) D-Axis injection procedure when $v_q = 0$, (b) Q-Axis injection procedure when $v_d = 0$.

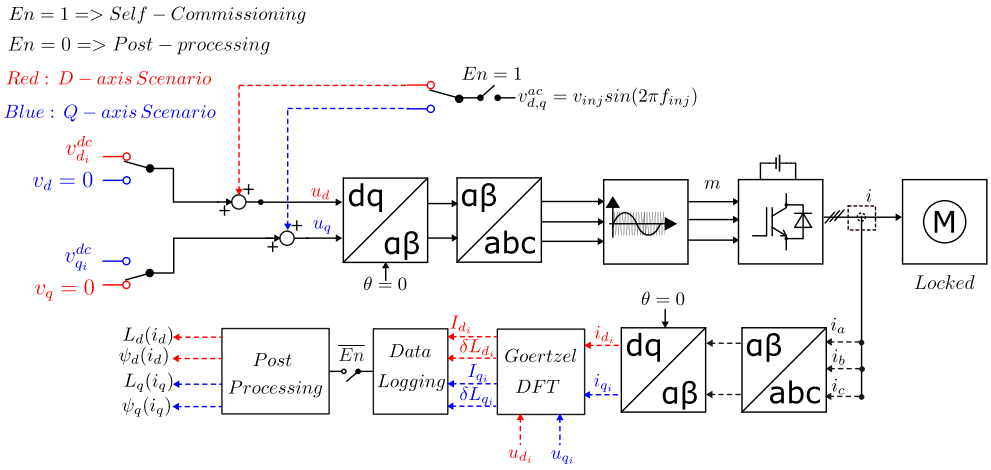

Figure 3.2: Procedure for the DC-biased high-frequency injection method.

frequency. The amplitude of the sinusoidal signal is chosen such that high-frequency components can be clearly detected in the sampled current, enabling more accurate frequency domain analysis.

The choice of injection frequency depends on the signal-to-noise ratio of the system and the sampling procedure. In practice, the injection frequency should be high enough to separate the response from the fundamental current components but still within the bandwidth of the current sensors and the inverter. Frequencies in the range of 200 Hz to 1 kHz are typically used, depending on the switching frequency of the inverter and the sampling rate of the control system. A lower frequency may result in interference from fundamental components, while a much higher frequency can be attenuated by the system dynamics or distorted due to inverter nonlinearity. Therefore, the selected frequency is a trade-off between observability, sensor bandwidth, and noise immunity. It should be noted that both tests for the d- and q-axes must be conducted at the same locked rotor position, and an initial alignment to a known rotor position is required before locking. Zero-position alignment is typically preferred for this purpose.

As mentioned, the inductance obtained from this method is the incremental inductance at each current point. Therefore, selecting a greater number of working

points results in a more precise inductance and flux map.

Considering that steady-state data is recorded under locked-rotor conditions, the frequency-domain mathematical model from (3.7), evaluated at the injected frequency f_{inj}, can be written as:

$$\begin{aligned} V_d(f_{inj}) &= R_s I_d(f_{inj}) + j2\pi f_{inj} L_d I_d(f_{inj}) \\ V_q(f_{inj}) &= R_s I_q(f_{inj}) + j2\pi f_{inj} L_q I_q(f_{inj}) \end{aligned} \tag{3.8}$$

Accordingly, since the signal injection procedure yields the incremental d- and q-axis inductances, we have:

$$\begin{aligned} \delta L_d(I_d) &= \frac{1}{2\pi f_{inj}} \Im\left(\frac{V_d(f_{inj})}{I_d(f_{inj})}\right) \\ \delta L_q(I_q) &= \frac{1}{2\pi f_{inj}} \Im\left(\frac{V_q(f_{inj})}{I_q(f_{inj})}\right) \end{aligned} \tag{3.9}$$

where the term $\Im(.)$ denotes the imaginary part of the complex quantity.

After fitting a piecewise model to the extracted incremental inductances, $L_d(i_d)$ and $L_q(i_q)$, the flux maps can be obtained by integrating the inductance functions along the current range:

$$\begin{aligned} \psi_d(I_d) &= \int_0^{Id} L_d(i_d) di_d \\ \psi_q(I_q) &= \int_0^{Iq} L_q(i_q) di_q \end{aligned} \tag{3.10}$$

In this method, explicit voltage compensation was not applied. Since the incremental inductance extracted from the high-frequency component effectively reflects the magnetic behavior, and the integration yields an accurate flux map without the need for resistive voltage compensation.

3.3.2 Bipolar Voltage Injection Method

The typical procedure of this method is illustrated in Figure 3.3. In this method, hysteresis current control is employed to regulate the stator currents during the injection process at standstill [42, 43, 59]. This control strategy ensures precise shaping of the

current waveform while maintaining simplicity and robustness. Reference currents are specified to inject the desired current magnitudes along the d and q axes, and the hysteresis controller ensures that the actual current remains within a specified tolerance band around the reference value. The controller achieves this by adjusting the output voltage vector via inverter switching, similar to standard current control. In this case, a simple hysteresis-based scheme is adopted rather than a PI current controller, due to its fast response and ease of implementation during standstill conditions where conventional controllers may be less effective due to unknown parameters of the machine that are needed for the tuning of the controller. To increase the current, the inverter applies a voltage vector oriented in the direction of the desired current and to decrease the current, a voltage vector in the opposite direction is applied:

$$u_{d,q}^{ref}(k) = \begin{cases} u^{max}, & \text{if } i_{d,q}(k) < -i_{d,q}^{max} \\ -u^{max}, & \text{if } i_{d,q}(k) > i_{d,q}^{max} \\ u_{d,q}^{ref}(k-1) & \text{otherwise,} \end{cases} \quad , u_{q,d}^{ref}(k) = 0 \tag{3.11}$$

According to Fig. 3.4a, for d-axis flux estimation, the reference current is set to the desired value i_d^{max}, and u_q^{ref} is maintained at zero. The hysteresis controller regulates i_d while ensuring that i_q remains negligible. Similarly, as shown in Fig. 3.4b, for q-axis flux estimation, the reference current i_q^{max} is applied, and u_d^{ref} is held at zero. The hysteresis controller regulates i_q, ensuring effective decoupling between the axes.

During the injection process, the reference voltages and output currents are sampled. Using these values, the stator flux linkages Ψ_d and Ψ_q are calculated using the forward Euler approximation, which provides the flux characteristics required for self-commissioning:

$$\Psi_{d,q}(k+1) = \Psi_{d,q}(k) + T_s \left[u_{d,q}(k) - R_s i_{d,q}(k) \right] \tag{3.12}$$

3.4 Proposed Self-commissioning Method

This section presents a self-commissioning methodology for synchronous reluctance motors (SynRMs), aimed at characterizing motor parameters and mapping flux hys-

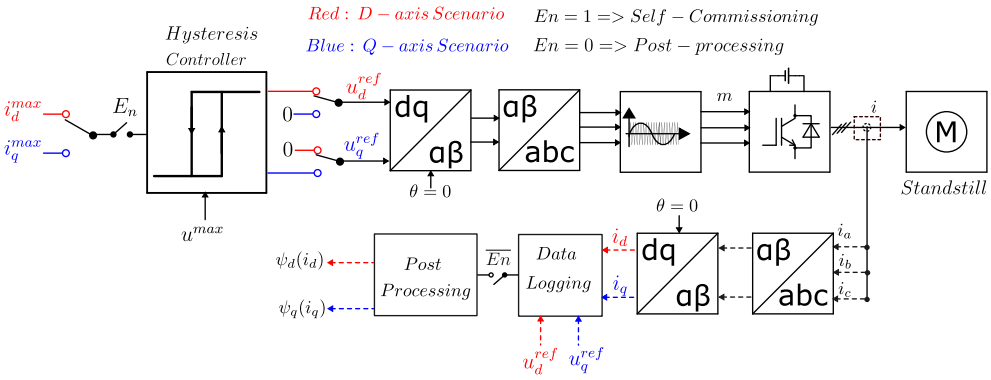

Figure 3.3: Procedure for the bipolar voltage injection method.

teresis at standstill, without the need for rotor locking. The process loop of the method is illustrated in Figure 3.5. The method systematically applies a specific voltage pattern, evaluates the electrical behavior of the motor, and calculates critical parameters such as total resistance, inverter voltage drops, and flux linkage characteristics for both the d and q axes.

The process begins with the application of a three-level voltage pattern, represented as $(u^{ref}, 0, -u^{ref}, 0, u^{ref})$. This pattern is applied sequentially, with voltage amplitudes decreasing from a maximum value to a minimum desired value using a predetermined decrement ratio or fixed step. Importantly, the procedure is performed at standstill, and the rotor shaft is free to move without mechanical locking. This ensures that the motor operates under natural conditions during the self-commissioning process.

To determine the appropriate maximum voltage level, the motor is initially subjected to incrementally increasing voltages at standstill while monitoring the resulting current. The voltage at which the current reaches the nominal peak value of the motor is recorded. This voltage is then scaled by a predefined ratio to define the maximum voltage level for self-commissioning, ensuring that the applied voltage levels are sufficient to drive the motor into the saturated region. This step ensures that flux mapping and parameter estimation are performed over a wide and representative operating range.

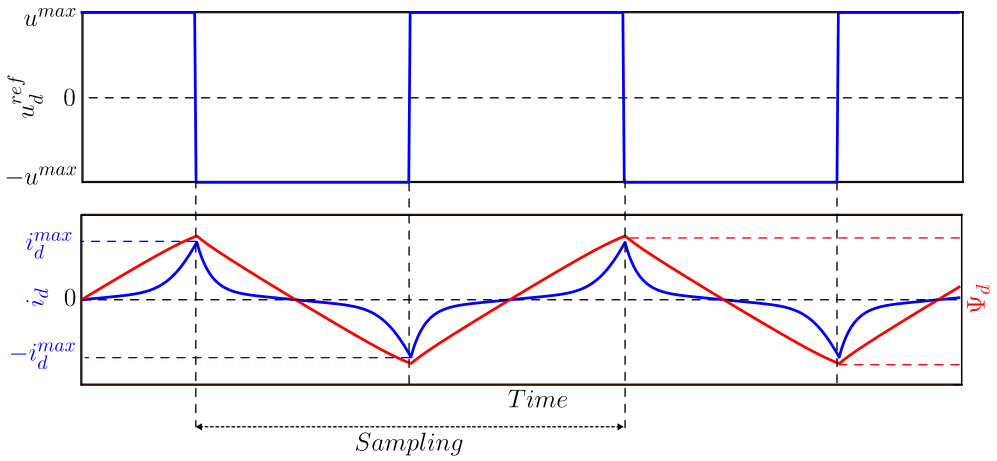

(a)

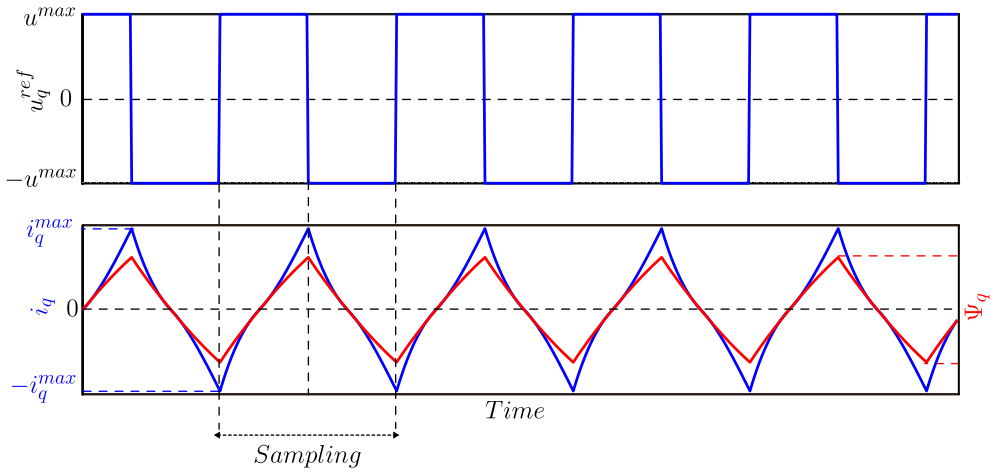

(b)

Figure 3.4: Bipolar voltage injection method: (a) *D*-axis injection procedure when $u_q^{ref} = 0$, (b) *Q*-axis injection procedure when $u_d^{ref} = 0$.

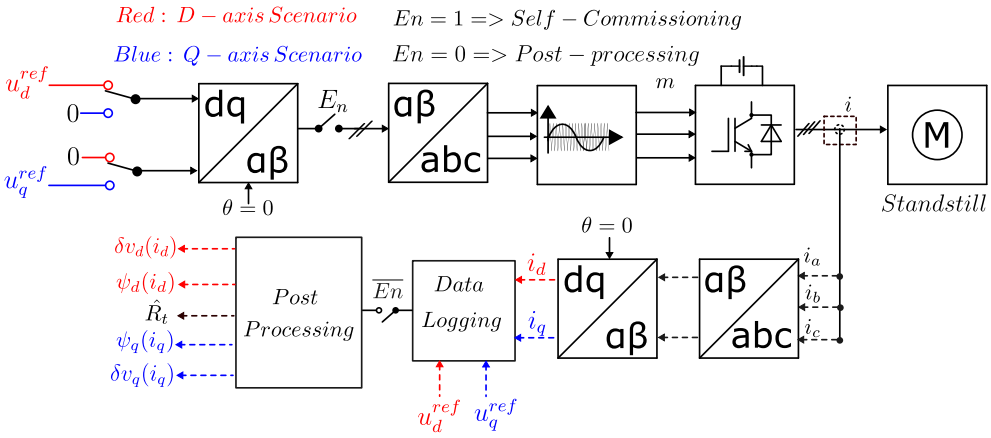

Figure 3.5: Procedure for the proposed voltage injection method.

The total resistance $\hat{R}_t$, comprising the stator resistance and any additional series resistances, is estimated based on two voltage patterns within the applied sequence, chosen near the nominal operating current of the machine. The steady-state currents corresponding to two different voltage levels are measured. The reference voltages $u_{d,q}^{ref}$ used in this step represent the voltage setpoints commanded to the inverter. While these setpoints are used for calculating resistance, it is important to note that inverter nonlinearities, such as dead-time effects or voltage drops, can cause deviations between the reference and the actual applied voltage.

To minimize the impact of such nonlinearities, this estimation is performed at relatively high current levels, where the effect of inverter nonlinearity becomes less pronounced compared to the total voltage. As a result, the estimation yields a sufficiently accurate approximation of $\hat{R}_t$ for use in subsequent calculations. Nevertheless, this is considered as an approximate resistance value, and more precise modeling can incorporate measured voltage or compensated inverter output if higher accuracy is required.

$$\hat{R}_t = \frac{u_{d,q_1}^{ref} - u_{d,q_2}^{ref}}{i_{d,q_1} - i_{d,q_2}} = \frac{\delta u_{d,q}^{ref}}{\delta i_{d,q}} \tag{3.13}$$

Following the estimation of total resistance, the total voltage drop introduced

by the inverter and other components is estimated. For each steady-state level of applied voltage, the measured current is used to compute the resistive voltage drop by multiplying the estimated total resistance with the current. Since the procedure is conducted at standstill and the rotor is assumed to remain stationary, the back-EMF component due to rotor motion is negligible and can be omitted from the voltage equation. By subtracting the estimated resistive voltage drop from the commanded inverter voltage, the remaining component is interpreted as the voltage drop of the inverter:

$$\delta v_{d,q}(i_{d,q}) = u_{d,q}^{ref} - \hat{R}_t \, i_{d,q} \tag{3.14}$$

As mentioned before, the estimated total resistance $\hat{R}_t$ obtained from voltage and current data, may also include the effective series resistance of the inverter, such as on-state voltage drops in the switching devices. As a result, the separation between stator and inverter contributions is approximate, and part of the inverter voltage drop may already be included in the resistive term. Despite this potential overlap, the remaining voltage $\delta v_{d,q}$ is still treated as an empirical correction factor to improve flux estimation accuracy. This simplification is acceptable in the context of standstill self-commissioning, where precise decoupling of all resistive effects is not strictly necessary for generating accurate flux maps.

The actual voltage applied to the motor is then obtained by compensating for the estimated inverter voltage drop. Using this corrected voltage, the flux of the motor is calculated by integrating the voltage difference over time for each applied voltage pattern:

$$\begin{aligned} \psi_d(t) &= \int_0^T (u_d^{ref} - \delta v_d(i_d) sgn(i_d) - \hat{R}_t \, i_d(t)) dt \\ \psi_q(t) &= \int_0^T (u_q^{ref} - \delta v_q(i_q) sgn(i_q) - \hat{R}_t \, i_q(t)) dt \end{aligned} \tag{3.15}$$

Here, T denotes the sampling and data logging period for a single pattern. The result of this integration forms the basis of the hysteresis flux map, which characterizes the flux-current relationship of the motor.

To capture the complete flux characteristics of the motor, the procedure is carried out independently for the d- and q-axes, as shown in Figure 3.6 and Figure 3.7. During the d-axis process, the q-axis voltage is set to zero, and the flux is mapped for the

d-axis. Similarly, during the q-axis process, the d-axis voltage is set to zero while the flux is mapped for the q-axis. It is noted that during the q-axis procedure, minor rotor movement may occur due to the absence of a mechanical lock. To counteract this movement, a compensating voltage is applied to the d-axis using a current controller, ensuring that the d-axis current remains zero throughout the process.

This self-commissioning method provides an effective framework for estimating motor parameters and flux linkage characteristics without requiring rotor locking. The approach accounts for critical aspects such as inverter voltage drops, total resistance, and flux mapping for both axes, ensuring accurate motor characterization. The entire procedure is executed automatically through a predefined sequence of voltage patterns and data acquisition routines, without the need for human intervention or manual parameter tuning. This unsupervised operation is made possible by relying only on current measurements at standstill, with each step; resistance estimation, inverter drop compensation, and flux calculation; performed in software using real-time feedback. This information is essential for achieving precise control and optimizing the performance of synchronous reluctance motors.

3.5 Simulation Analysis

The SynRM used for simulation is selected from [48, 42], and its details are provided in Table 3.1. The methods described in the previous sections have been implemented in MATLAB/Simulink, and their results are compared with those of the proposed method. To simulate the machine behavior, the analytical flux model provided in [42] is used, which captures the nonlinear magnetic characteristics of the SynRM based on current-dependent inductance expressions. This model enables accurate simulation of flux linkage and torque under varying current conditions without requiring finite element analysis.

Simulation of DC-biased HFSI Method

- D-axis: A $200\,Hz$, 2-volt sinusoidal voltage is superimposed on different levels of DC voltage, ranging from 60 volts to 0 volts, with a decrement ratio of 0.5.

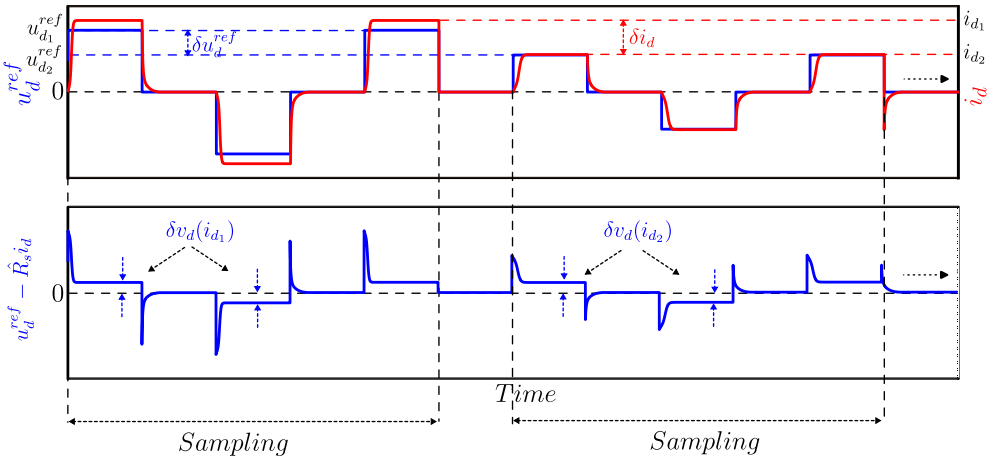

(a)

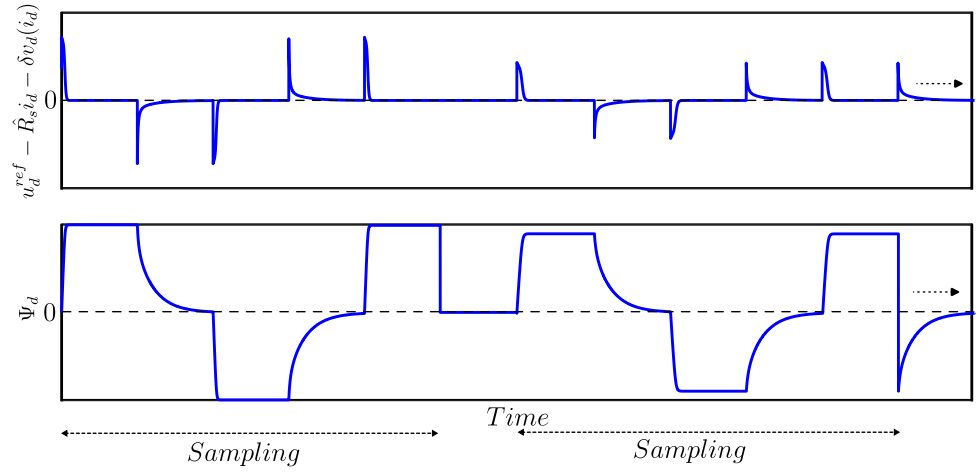

(b)

Figure 3.6: Proposed voltage injection method for the d-axis when $u_q^{ref} = 0$ is applied: (a) D-axis voltage injection, resistance and voltage drop calculation, (b) D-axis voltage compensation and flux calculation.

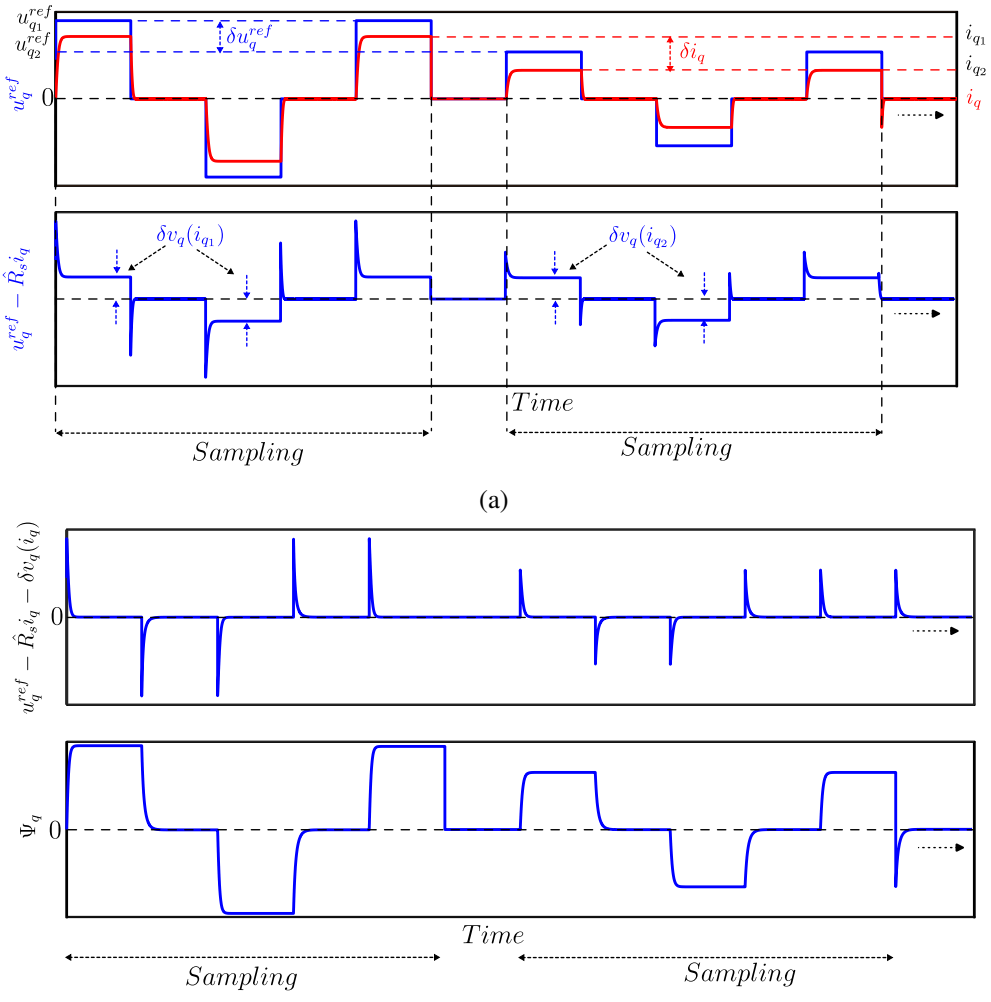

Figure 3.7: Proposed voltage injection method for the q-axis when $u_d^{ref} = 0$ is applied: (a) Q-axis voltage injection, resistance and voltage drop calculation, (b) Q-axis voltage compensation and flux calculation.

Table 3.1: SynRM rating parameters used for simulation.

Power P_N	2.2 kW
Speed n_N	1500 rpm
Pole pairs	2
Torque T_N	15 Nm
Current I_N	5.08 A
Voltage U_N	400 V
Resistance R_s	3.6 Ω
Frequency f_N	50 Hz

This voltage is applied to the d-axis while zero voltage is applied to the q-axis, as shown in Figure 3.8. The inductance map and the corresponding extracted flux map of the d-axis are illustrated in Figure 3.9.

- Q-axis: A $200\,Hz$, 2-volt sinusoidal voltage is superimposed on different levels of DC voltage, ranging from 30 volts to 0 volts, with a decrement ratio of 0.5. This voltage is applied to the q-axis while zero voltage is applied to the d-axis, as shown in Figure 3.10. The inductance map and the corresponding extracted flux map of the q-axis are illustrated in Figure 3.11.

Simulation of Bipolar Voltage Injection Method

Simulation of this method has been implemented to generate the flux hysteresis map over a high current range, based on the motor's nominal current, considering that the lower current range is a subset of the higher range:

- D-axis: The d-axis reference current for hysteresis control is set equal to $20A$, which is approximately three times the nominal current. The reference output voltage is set to 200 volts. Fig. 3.12a shows the time-domain applied voltage and the measured current during the d-axis procedure. The corresponding flux linkage in the d-axis is calculated using numerical integration, as described in

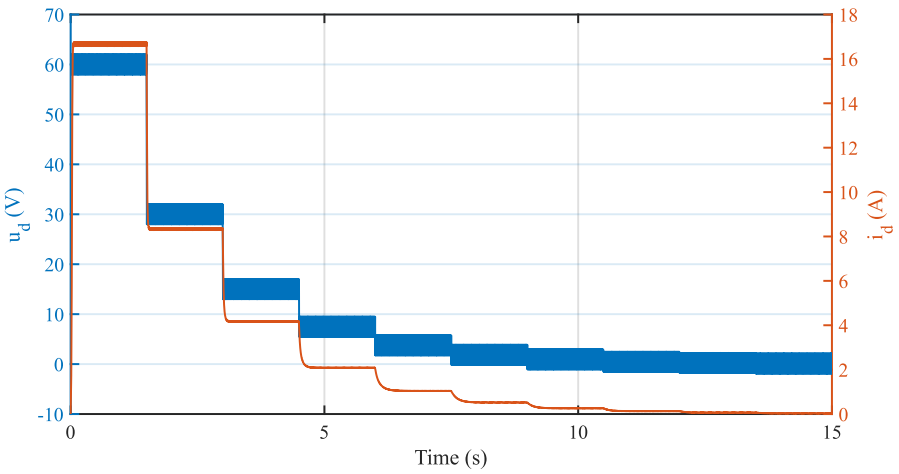

Figure 3.8: Injected voltage and corresponding measured current for the d-axis using the DC-biased HFSI method (simulation).

(3.12), and illustrated in Fig. 3.12b. Finally, the d-axis flux map is generated and shown in Fig. 3.14a.

- Q-axis: The q-axis reference current for hysteresis control is set equal to $14A$, which is approximately twice the nominal current. The reference output voltage is also set to 200 volts. Fig. 3.13a shows the time-domain applied voltage and the measured current during the q-axis procedure. The corresponding flux linkage in the q-axis is calculated using numerical integration, as described in (3.12), and illustrated in Fig. 3.13b. Finally, the q-axis flux map is generated and shown in Fig. 3.14b.

Simulation of Proposed Method

In the proposed simulation method, two reference voltage levels are applied separately to the d- and q-axes, following the procedure described earlier. These two voltage levels are used for estimating the total resistance. At this stage, it is not necessary to consider additional voltage levels, as the inverter is modeled as ideal. This

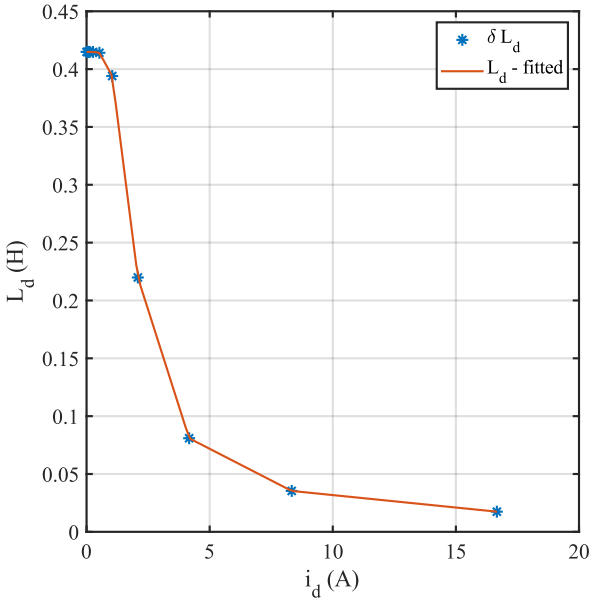

(a)

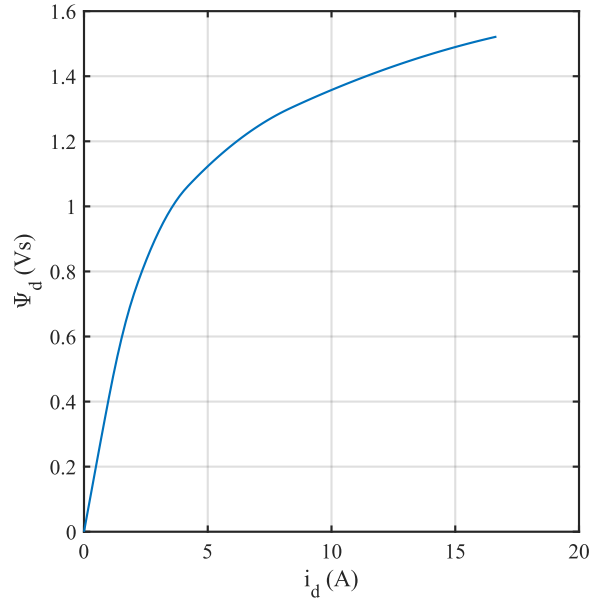

(b)

Figure 3.9: Simulation results obtained using the DC-biased HFSI method: (a) Inductance map for *d*-axis, (b) Flux map for *d*-axis.

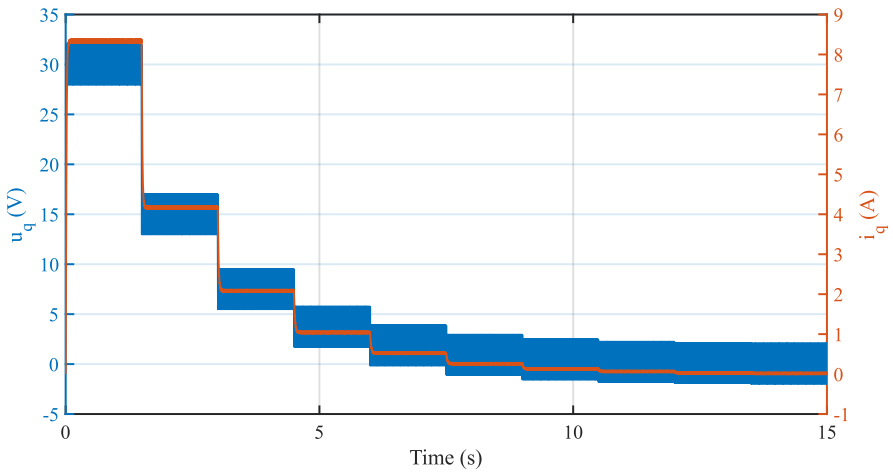

Figure 3.10: Injected voltage and corresponding measured current for the q-axis using the DC-biased HFSI method (simulation).

assumption implies that the output voltage precisely follows the reference command without any nonlinearities or voltage drops.

It should be noted that in a practical system with a non-ideal inverter, voltage deviations due to switching behavior, dead-time effects, and device losses would influence the measurements. In such cases, the estimated total resistance would inherently include the effects of the inverter's linearity and parasitic resistance, which cannot be entirely separated from the motor model. However, since an ideal inverter is assumed in this simulation, the voltage applied to the motor terminals is taken as equal to the reference voltage, ensuring a clean and isolated evaluation of the proposed method.

- D-axis: $60V$ and $36V$ reference voltages have been used as the test voltage levels. These levels are chosen such that the steady-state current remains approximately between the nominal current and twice the nominal current, which leads to more accurate resistance estimation. Fig. 3.15a shows the time-domain applied voltage and measured current in the d-axis procedure. The total resistance, estimated using (3.13), is found to be 3.6Ω. After that, the correspond-

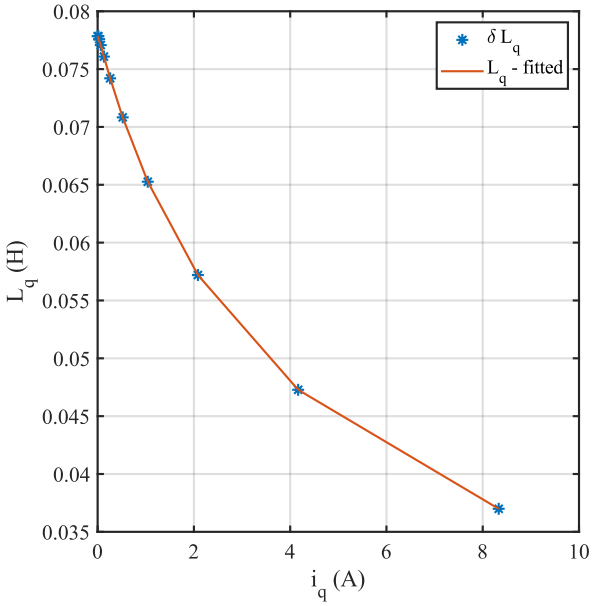

(a)

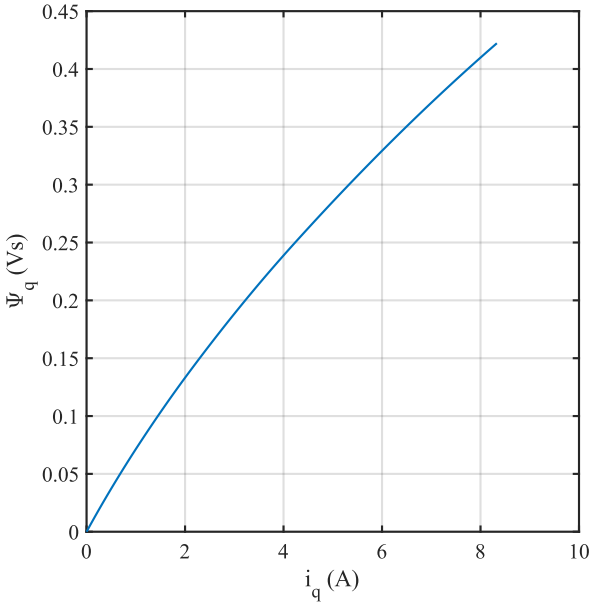

(b)

Figure 3.11: Simulation results obtained using the DC-biased HFSI method: (a) Inductance map for q-axis, (b) Flux map for q-axis.

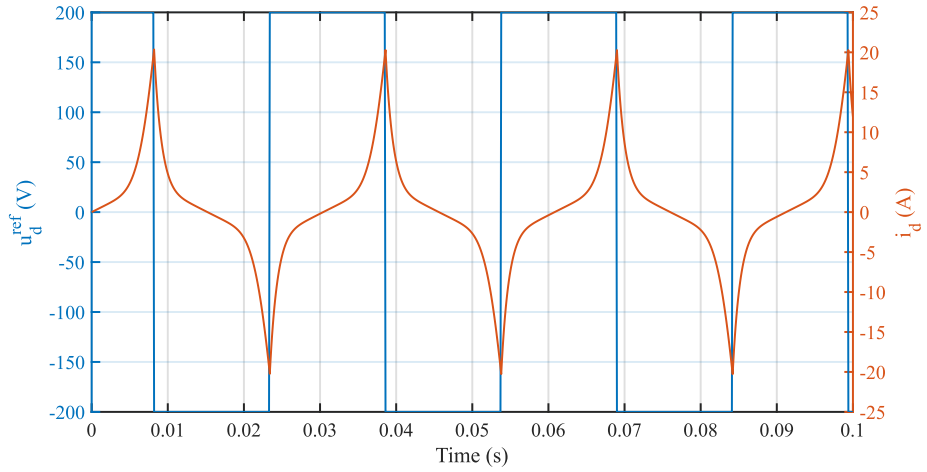

(a)

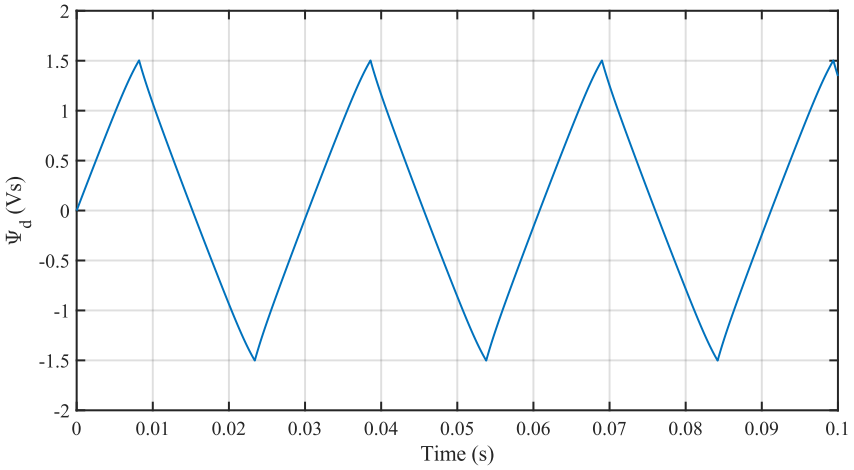

(b)

Figure 3.12: Simulation results using the bipolar voltage excitation method for the *d*-axis: (a) Voltage and current in time domain, (b) Flux in time domain.

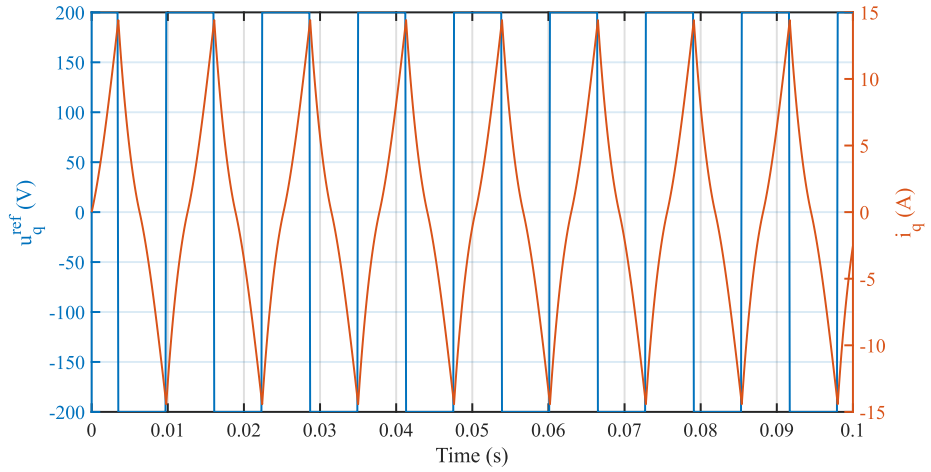

(a)

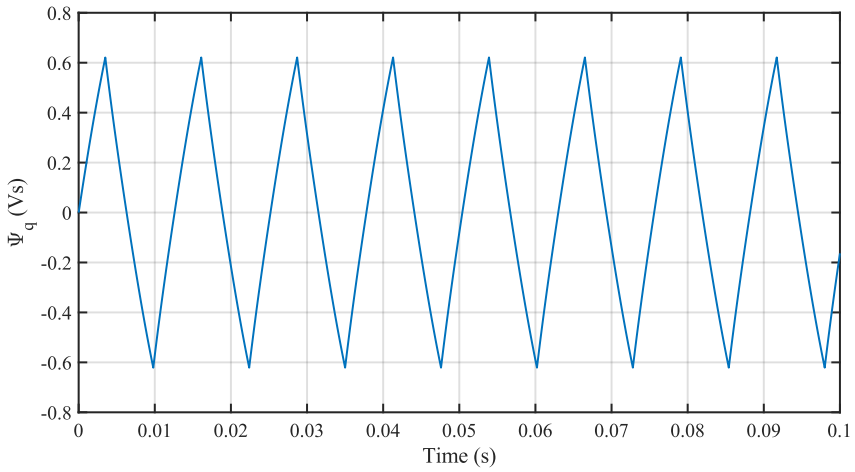

(b)

Figure 3.13: Simulation results using the bipolar voltage excitation method for the q-axis: (a) Voltage and current in time domain, (b) Flux in time domain.

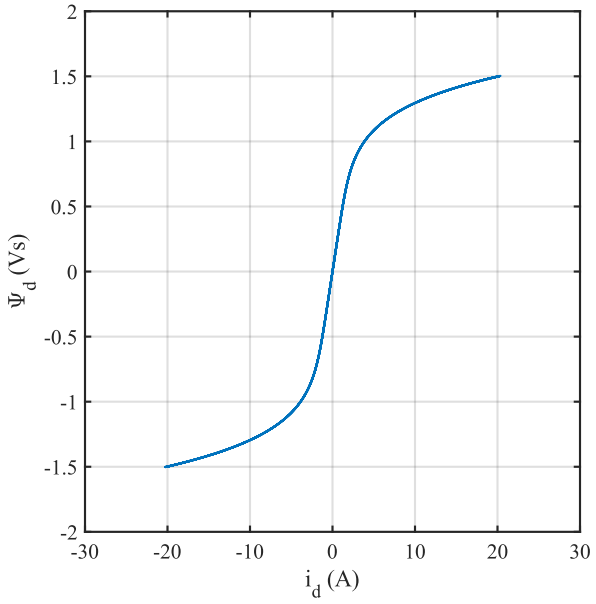

(a)

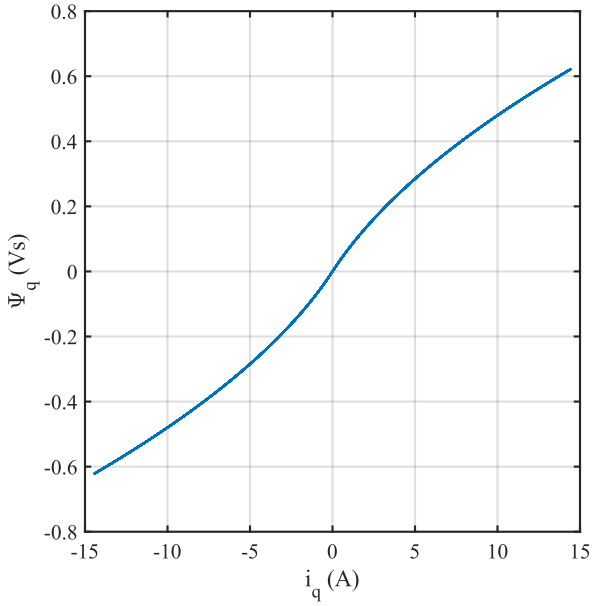

(b)

Figure 3.14: Simulated flux map obtained using the bipolar voltage excitation method: (a) *D*-axis flux map, (b) *Q*-axis flux map.

ing flux linkage in the d-axis is calculated using (3.14) and (3.15). The time-domain simulation results are illustrated in Fig. 3.15b. Finally, the d-axis flux map is generated and shown in Fig. 3.17a.

- Q-axis: $30V$ and $36V$ reference voltages have been used as the test voltage levels. Considering that the q-axis flux tends to saturate faster than the d-axis, lower voltage and current levels are sufficient. Fig. 3.16a shows the time-domain applied voltage and measured current in the q-axis procedure. The total resistance, estimated using (3.13), is also found to be $3.6\,\Omega$. After that, the corresponding flux linkage in the q-axis is calculated using (3.14) and (3.15). The time-domain simulation results are illustrated in Fig. 3.16b. Finally, the q-axis flux map is generated and shown in Fig. 3.17b.

Comparison of the Simulation Results

The flux map extracted from the proposed method has been compared with the results of two other methods, one considering inverter nonlinearity and voltage drop in the model, and one without. Figure 3.18 shows the result without incorporating inverter nonlinearity. The flux maps extracted from the proposed method and the bipolar voltage excitation method closely match, while a small deviation is observed in the result from the HFSI method. This difference is likely due to numerical issues arising from the linear piecewise fitting step during inductance map generation, which used a limited number of test points. Additional errors may also result from numerical integration in the HFSI method, especially near zero current where data acquisition becomes more error-prone.

Figure 3.19 shows the result when inverter nonlinearity is included in the simulation. It can be observed that the proposed method yields an accurate and symmetric flux map by compensating for inverter voltage drops within the procedure; an outcome that aligns with the expected behavior of a synchronous reluctance motor.

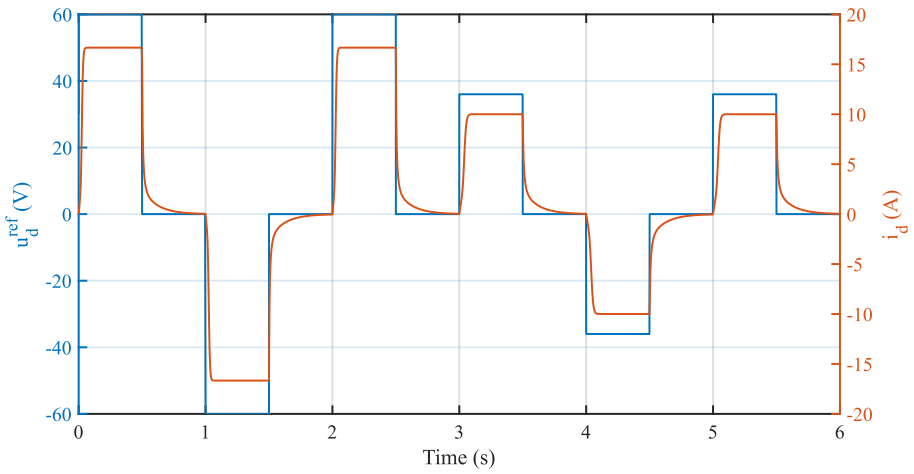

(a)

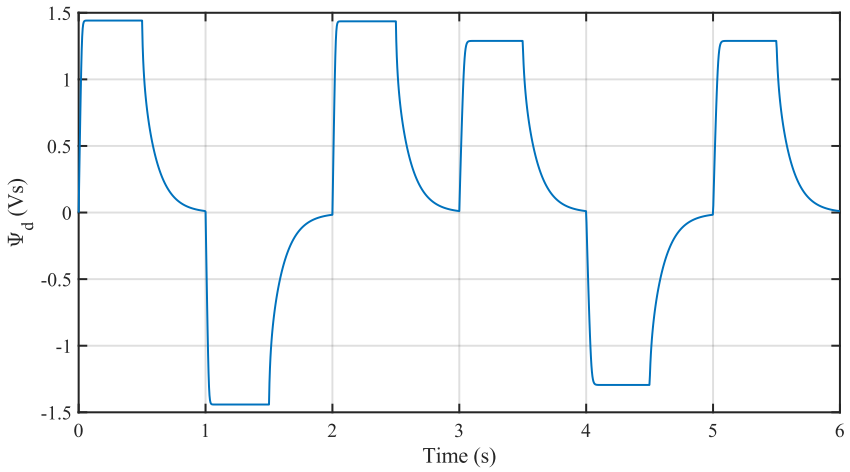

(b)

Figure 3.15: Simulation results using the proposed voltage excitation method for the *d*-axis: (a) Voltage and current in time domain, (b) Flux in time domain.

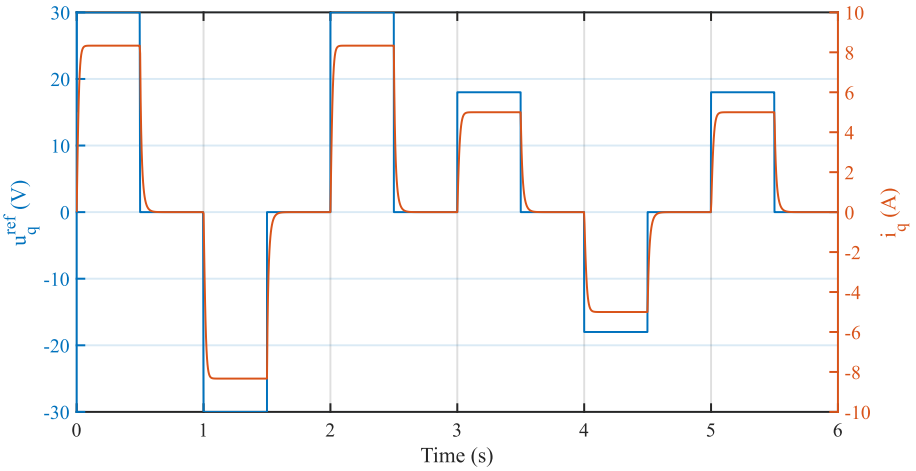

(a)

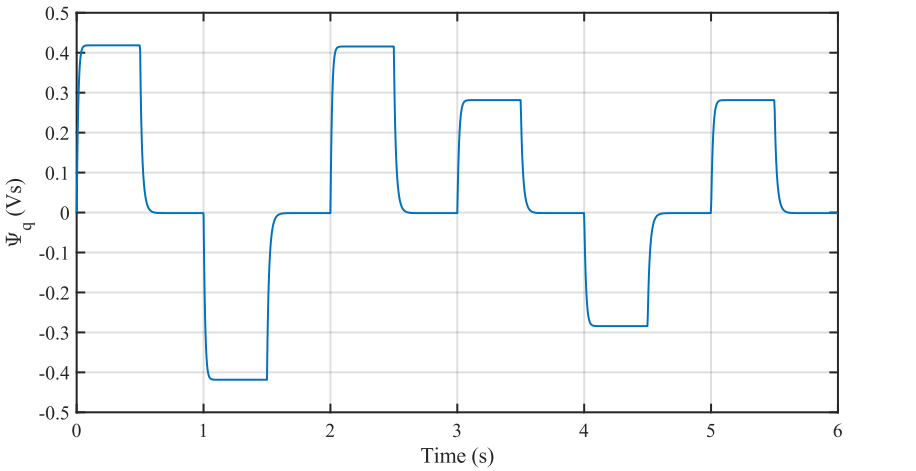

(b)

Figure 3.16: Simulation results using the proposed voltage excitation method for the q-axis: (a) Voltage and current in time domain, (b) Flux in time domain.

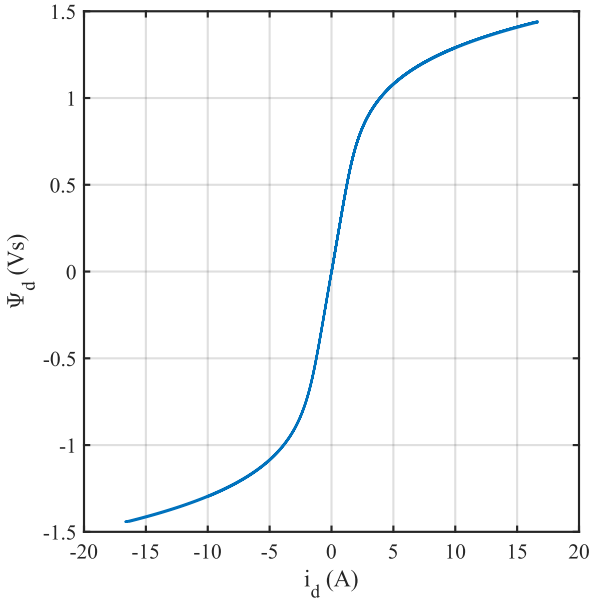

(a)

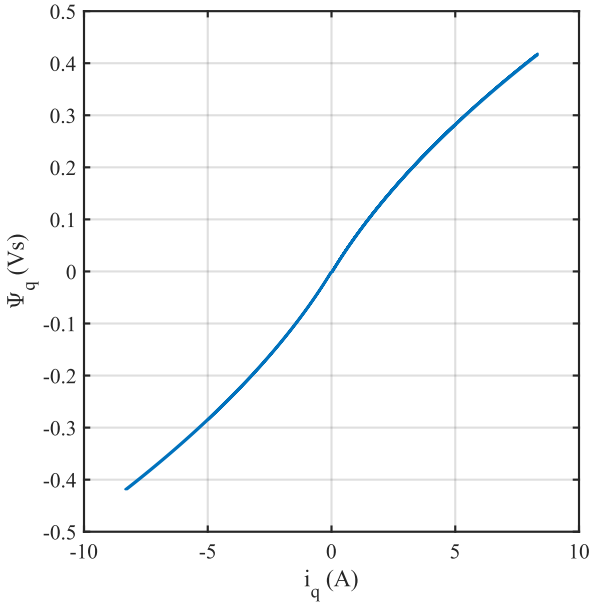

(b)

Figure 3.17: Simulated flux map obtained using the proposed voltage excitation method: (a) *D*-axis flux map, (b) *Q*-axis flux map.

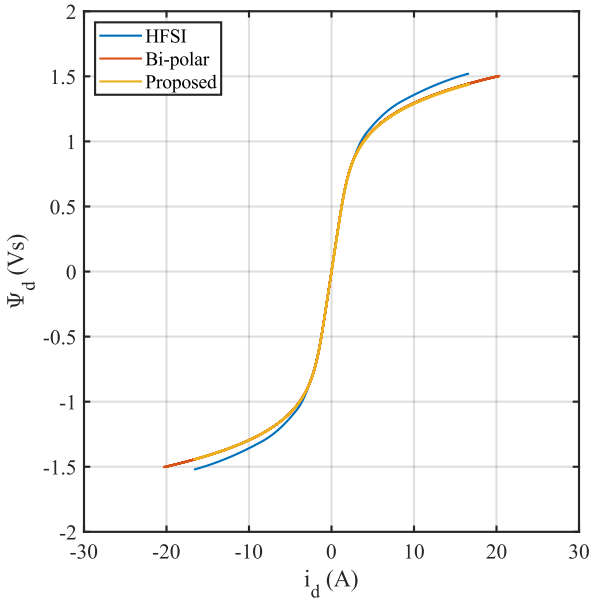

(a)

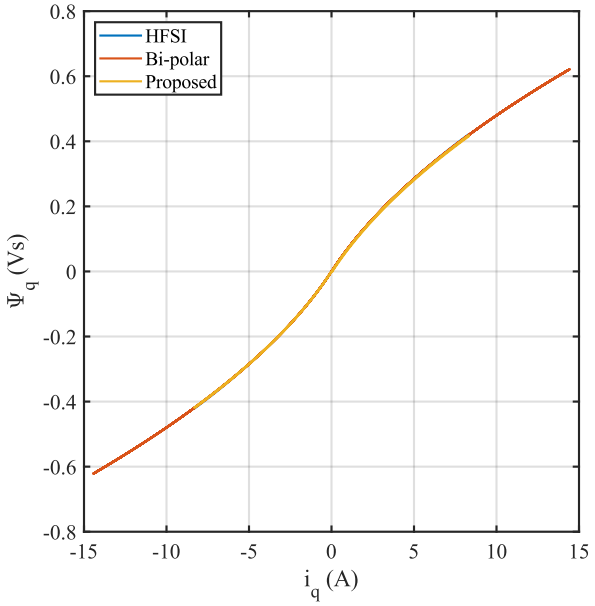

(b)

Figure 3.18: Comparison of simulation results for a system model excluding inverter nonlinearities: (a) *D*-axis flux map, (b) *Q*-axis flux map.

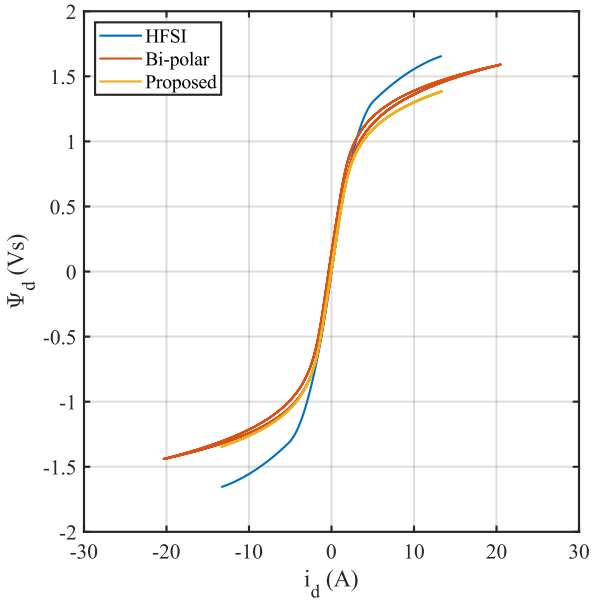

(a)

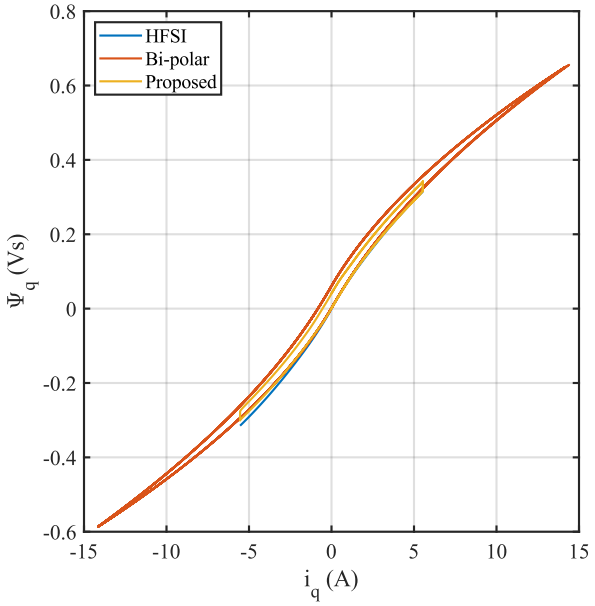

(b)

Figure 3.19: Comparison of simulation results including inverter nonlinearities: (a) *D*-axis flux map, (b) *Q*-axis flux map.

3.6 Experimental Implementation and Results

In this section, all three methods have been implemented experimentally and compared to evaluate the performance of the proposed method in a real environment. The SynRM used is the same as that described in Table 2.2. A $1.1\,kW$ commercial inverter, incorporating an STM32F303 microcontroller and the IGBT modules, has been used to drive the motor. In all tests, the inverter DC bus voltage is set to $320\,V$. The switching frequency and sampling time are set to $10\,kHz$ and $200\,\mu s$, respectively.

Experimental Result of DC-biased HFSI Method

The experimental test using the HFSI method was performed automatically using the processor embedded in the commercial inverter. For the d-axis, a minimum of $5\,V$ with an incremental step of $5\,V$ was applied, reaching a maximum level of $50\,V$ (i.e., 10 working points), while zero voltage was applied to the q-axis. During voltage excitation, a $250\,Hz$ sinusoidal voltage with an amplitude of $5\,V$ was superimposed on the applied DC voltage levels. At each DC level, during high-frequency signal injection, the corresponding current was measured. Using the Goertzel Discrete Fourier Transform (DFT), the incremental inductance was calculated in real time and logged.

A similar procedure was implemented for the q-axis, while zero voltage was applied to the d-axis. A minimum of $5\,V$ with an incremental step of $3\,V$ was applied, reaching a maximum level of $32\,V$ (i.e., 10 working points). Similarly, a sinusoidal voltage with an amplitude of $5\,V$ and a frequency of $250\,Hz$ was superimposed on the DC levels. Using the Goertzel DFT, the q-axis incremental inductance was also calculated in real time and logged.

In post-processing, the incremental d- and q-axis inductance maps were generated using linear interpolation. Figure 3.20 shows the generated d- and q-axis inductance maps. By integrating along the current range, the corresponding flux maps were generated and are plotted in Fig. 3.21a and Fig. 3.21b.

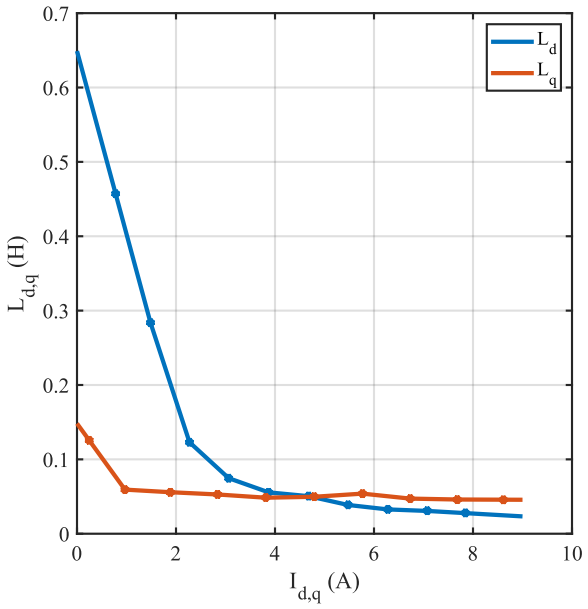

Figure 3.20: Experimental inductance maps for the d-axis and q-axis obtained using the DC-biased HFSI method.

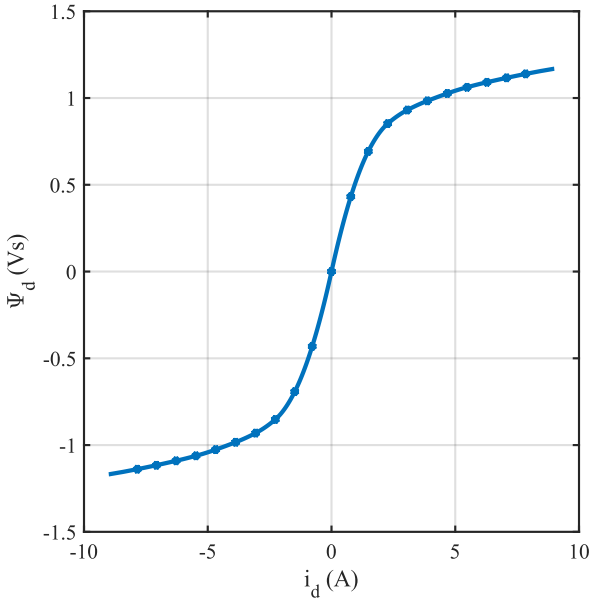

(a)

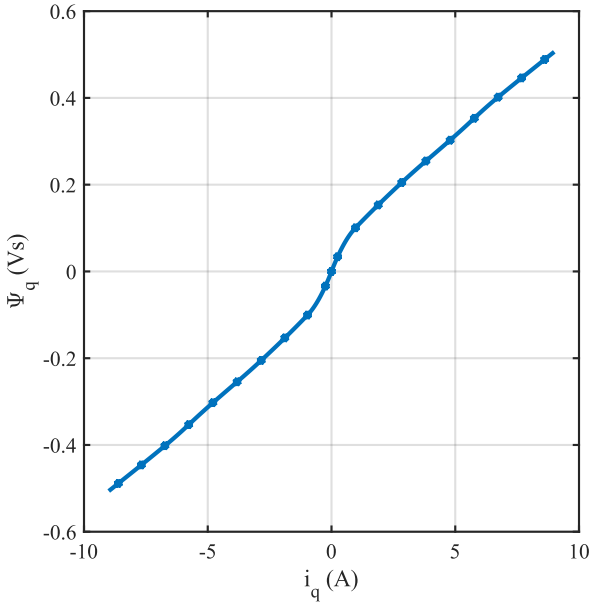

(b)

Figure 3.21: Experimental flux map obtained using the HFSI method: (a) *D*-axis flux map, (b) *Q*-axis flux map.

Experimental Result of Bipolar Voltage Injection Method

The procedure illustrated in Figure 3.3 has been implemented experimentally to extract the flux map of the SynRM using bipolar voltage injection through hysteresis current control. The maximum output voltage of the hysteresis current controller was set to $120V$.

To extract the d-axis flux map, a set of reference currents ranging from $1A$ to $8A$, with an incremental step of $1A$, was utilized. The corresponding output currents were measured using current sensors, as shown in Figure 3.22. Using the cold resistance value provided in the motor datasheet and direct measurement, the flux map was extracted by employing (3.12). The resulting d-axis flux map is illustrated in Figure 3.23.

Similarly, to extract the q-axis flux map, a set of reference currents ranging from $1A$ to $7A$, with an incremental step of $1A$, was used. The corresponding output currents were measured using current sensors, as shown in Figure 3.24. There is a small timing mismatch between the applied voltage and the measured current, which is likely caused by delays in the measurement system and can be corrected by aligning the signals more accurately in post-processing. Although it does not affect the effectiveness of the method, this skew does introduce some visible effects, such as the slight loops in the flux map. Improving the synchronization would help remove these effects in future tests.

Again, using the cold resistance value from the motor datasheet, the flux map was extracted by applying (3.12). The resulting q-axis flux map is illustrated in Figure 3.25.

It should be noted that only one cycle is sufficient for calculating the flux hysteresis map; however, averaging over multiple cycles can yield a more accurate result.

Experimental Result of Proposed Method

Implementation of the proposed method is based on the procedure illustrated in Figure 3.5. According to the procedure described in the relevant section, a three-level voltage pattern with varying amplitudes is applied to the machine, and the corre-

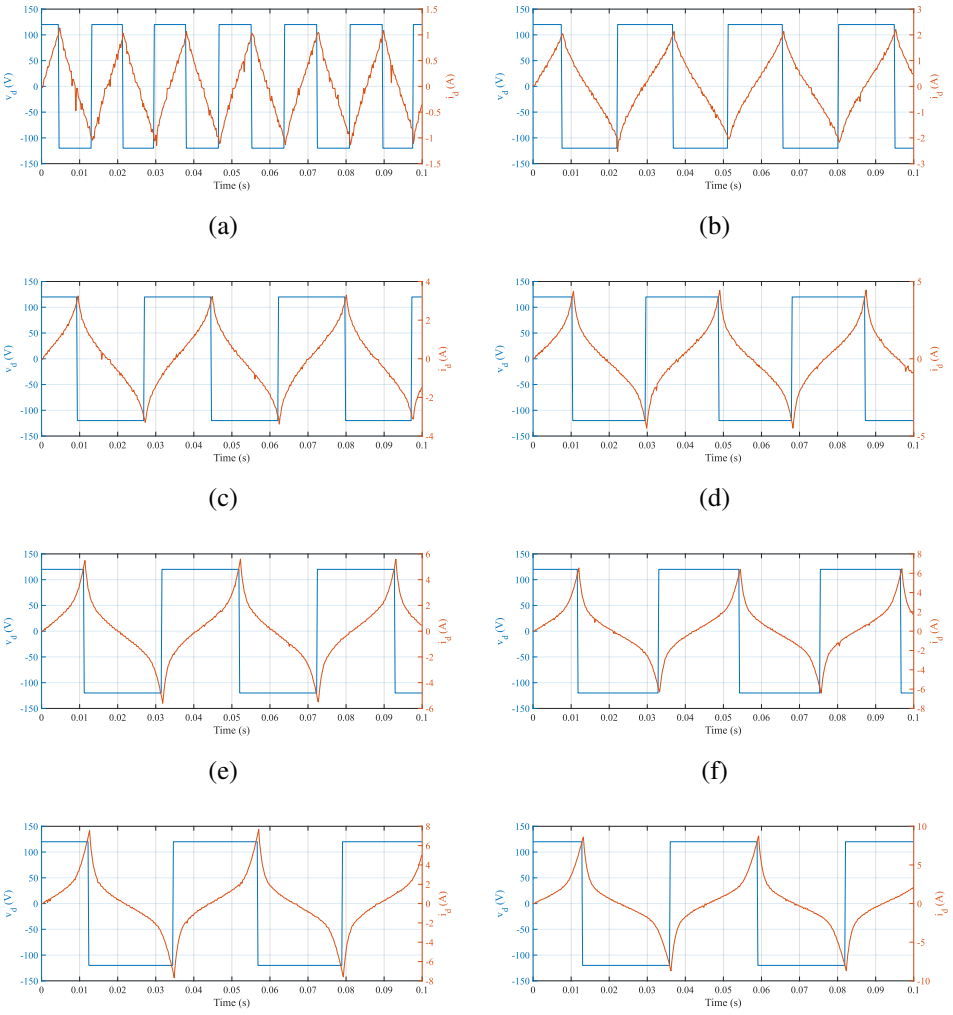

Figure 3.22: Experimental applied voltage and measured current in the d-axis during SynRM self-commissioning using the bipolar voltage injection method: (a) $i_d^{max} = 1A$, (b) $i_d^{max} = 2A$, (c) $i_d^{max} = 3A$, (d) $i_d^{max} = 4A$, (e) $i_d^{max} = 5A$, (f) $i_d^{max} = 6A$, (g) $i_d^{max} = 7A$, (h) $i_d^{max} = 8A$.

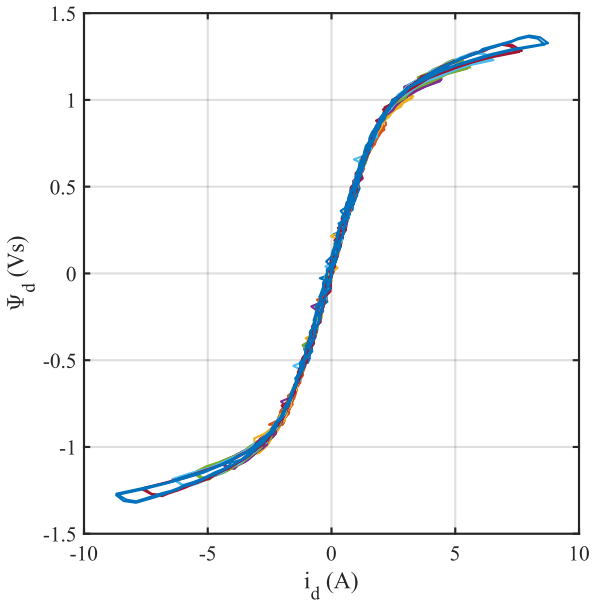

Figure 3.23: Experimental *d*-axis flux map obtained using the bipolar voltage injection method.

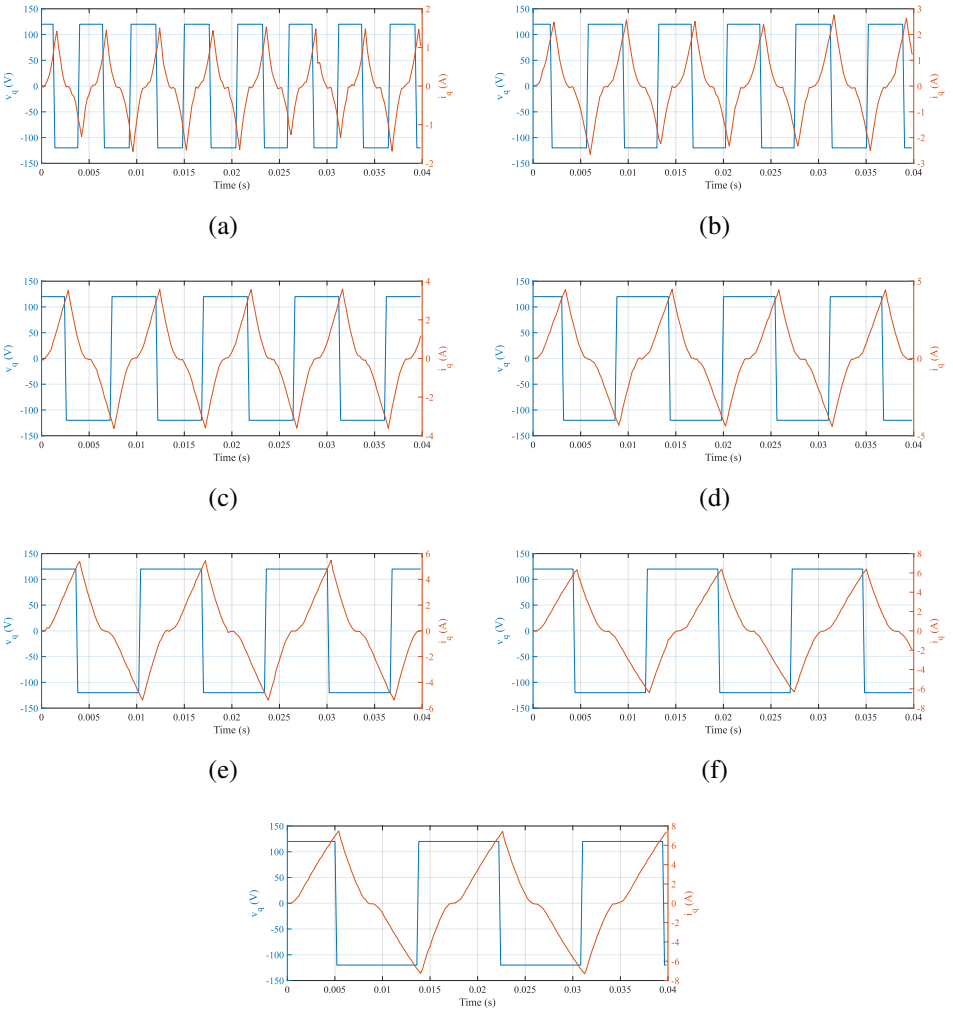

Figure 3.24: Experimental applied voltage and measured current in the q-axis during SynRM self-commissioning using the bipolar voltage injection method: (a) $i_q^{max} = 1A$, (b) $i_q^{max} = 2A$, (c) $i_q^{max} = 3A$, (d) $i_q^{max} = 4A$, (e) $i_q^{max} = 5A$, (f) $i_q^{max} = 6A$, (g) $i_q^{max} = 7A$.

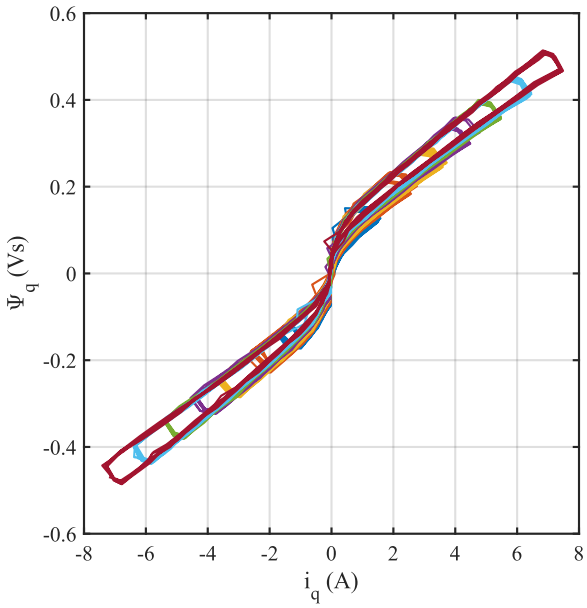

Figure 3.25: Experimental q-axis flux map obtained using the bipolar voltage injection method.

sponding output currents are logged for post-processing.

For d-axis flux map identification, a voltage range from $5V$ to $60V$ is applied in a three-level pattern to the d-axis, while zero voltage is applied to the q-axis. The corresponding currents are measured and logged using current sensors. The duration of each level in the voltage pattern is set to $500ms$ to ensure the current reaches a steady state for accurate post-processing. The maximum voltage of $60V$ is chosen because it results in approximately three times the nominal current of the machine. The applied voltages and corresponding measured currents are shown in Figure 3.26. It is important to note again that no current controller was used in this experiment and the current waveforms are purely a result of the applied voltage steps. The unusual behaviors, like the almost linear rise in current during on-switching of the v_d and the almost step-wise change during off-switching of the v_d, are caused by non-ideal effects in the inverter, such as parasitic capacitance and dead-time. These effects tend to be more noticeable, especially at lower current levels.

Using two different voltage amplitudes near the nominal current, the total resistance is estimated to be 6.12Ω by applying (3.13). The voltage drop in the d-axis is then estimated using (3.14), since the motor is at standstill and no back-EMF is expected. Figure 3.27 illustrates the back-EMF before and after compensation, and it can be seen that the compensation is effective, as the back-EMF becomes nearly zero after correction. Finally, using (3.15), the flux linkage is calculated.

It should be noted that integrating voltage to obtain flux linkage may result in accumulated error near zero current due to noise and data acquisition imperfections, potentially leading to inaccuracies in the flux map. To mitigate this issue, integration is performed only from the start of each voltage level to the first zero-crossing of the back-EMF at that level, resulting in cleaner and more reliable results. The d-axis flux hysteresis map extracted using the proposed method is illustrated in Figure 3.28.

Furthermore, the estimated voltage drop in the d-axis is compared with the result obtained using an inverter self-commissioning method, as shown in Figure 3.29. The comparison shows that the estimated voltage drops are similar across different working points using the two methods.

Similarly, for q-axis flux map identification, a voltage range from $5V$ to $60V$

in a three-level pattern is applied to the q-axis, while zero voltage is applied to the d-axis. The corresponding currents are measured and logged using current sensors. The duration of each voltage level is also set to $500\,ms$ to allow the current to reach a steady state. However, this procedure may cause rotor movement due to the torque generated by the q-axis excitation. This makes voltage excitation in the q-axis more challenging, as it introduces a trade-off between maximum voltage amplitude, pattern duration, and the ability to achieve steady-state current without causing rotor displacement.

The applied voltages and corresponding measured currents are shown in Figure 3.30. Using two different voltage amplitudes near the nominal current, the total resistance is estimated to be $6.25\,\Omega$ by applying (3.13). The voltage drop in the q-axis is then estimated using (3.14), under the same assumption of no back-EMF at standstill. Figure 3.31 illustrates the back-EMF before and after compensation, confirming that the compensation is effective.

Finally, using (3.15), the q-axis flux linkage is calculated, considering the same precautions against accumulated integration error as discussed earlier. The q-axis flux hysteresis map extracted using the proposed method is shown in Figure 3.32. In addition, the estimated voltage drop in the q-axis is compared with the result obtained via the inverter self-commissioning method in Figure 3.33, showing strong agreement across different working points.

Comparison of Experimental Results

To compare the results of the proposed method with the other two procedures, an algebraic model was selected and fitted to the generated flux hysteresis maps using the nonlinear least squares method:

$$\Psi_{d,q}(i_{d,q}) = a + \frac{b}{1+\exp(-m\cdot(i_{d,q}-n))} + c\cdot i_{d,q} \tag{3.16}$$

where, a, b, c, m and n are the fitting parameters.

This model was chosen not to reflect the physical symmetry or magnetic characteristics of the machine, but only to enable consistent and accurate curve fitting

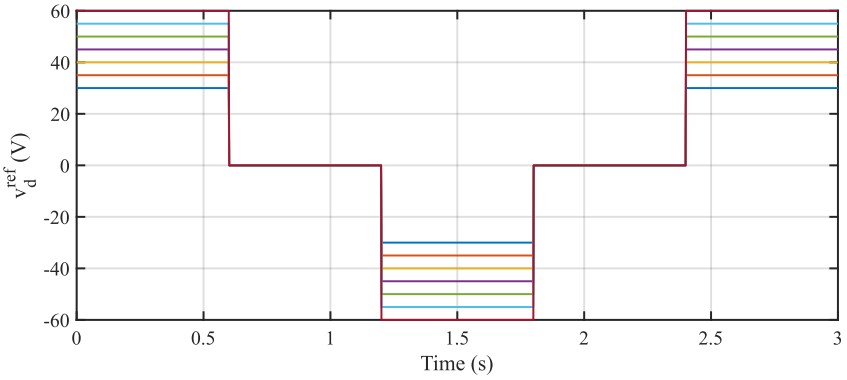

(a)

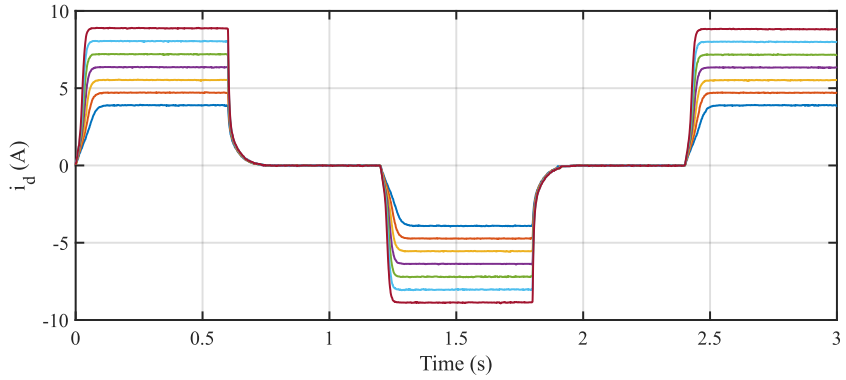

(b)

Figure 3.26: Experimental applied voltage and measured current in the *d*-axis using the proposed method.: (a) Applied voltage, (b) Measured current.

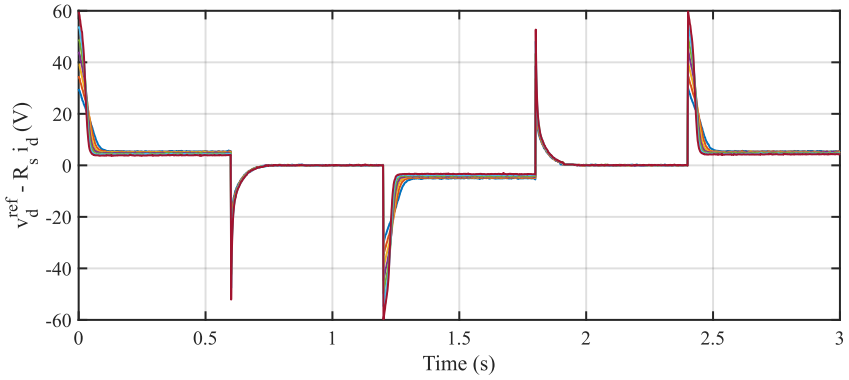

(a)

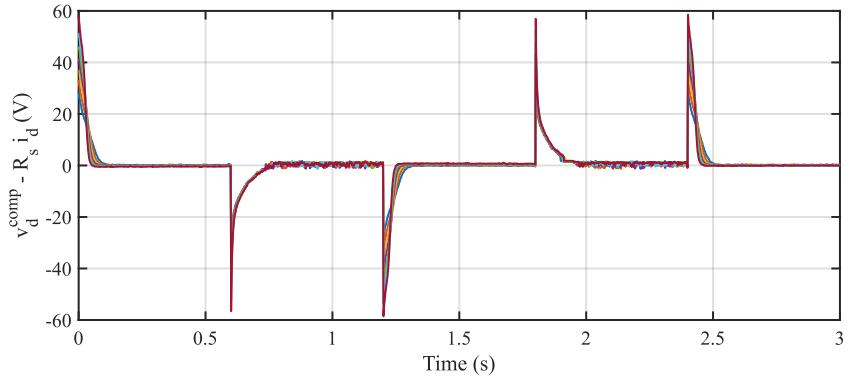

(b)

Figure 3.27: Back-EMF before and after voltage drop compensation in the d-axis using the proposed method: (a) Before compensation, (b) After compensation.

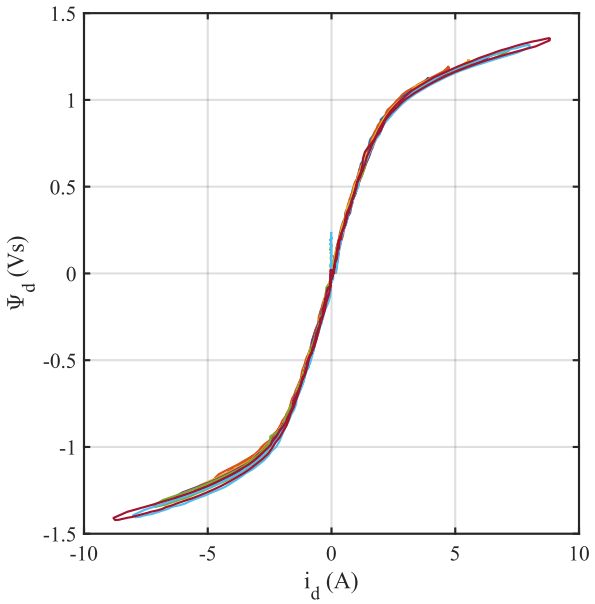

Figure 3.28: Experimental *d*-axis flux map obtained using the proposed self-commissioning method.

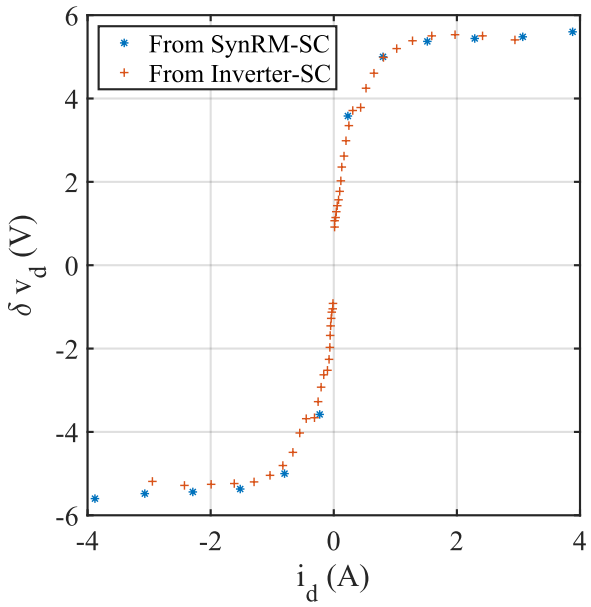

Figure 3.29: Experimental comparison of estimated voltage drop in the *d*-axis with inverter self-commissioning results.

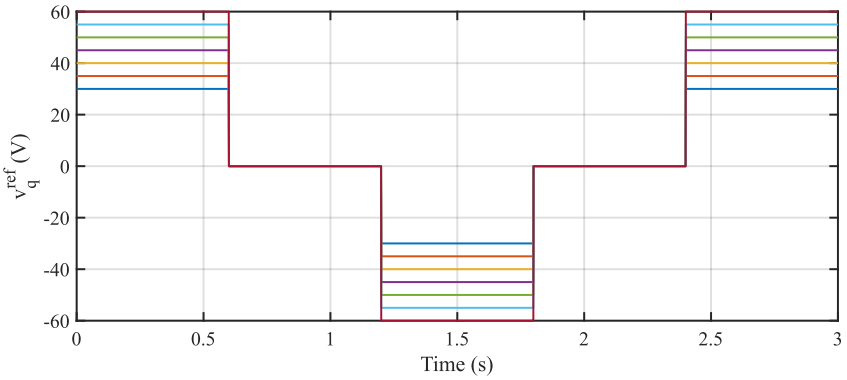

(a)

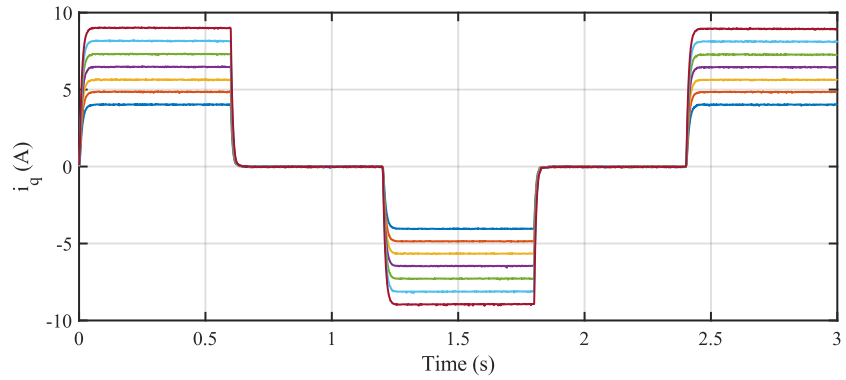

(b)

Figure 3.30: Experimental applied voltage and measured current in the q-axis using the proposed method: (a) Applied voltage, (b) Measured current.

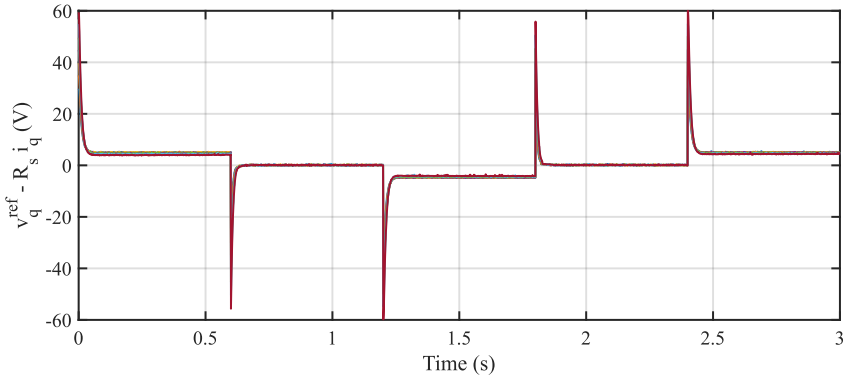

(a)

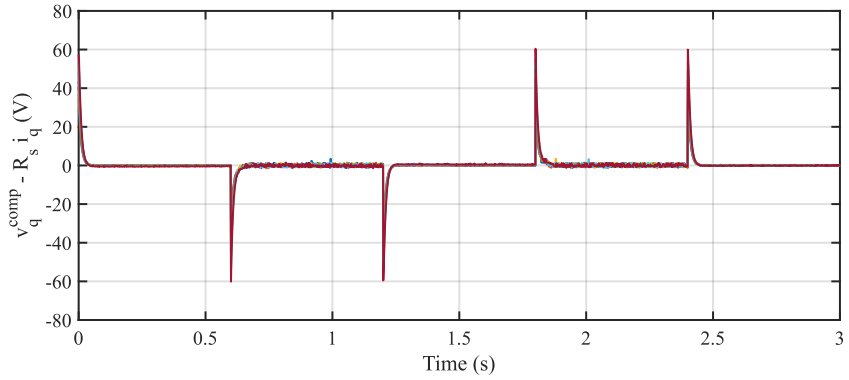

(b)

Figure 3.31: Back-EMF before and after voltage drop compensation in the q-axis using the proposed method: (a) Before compensation, (b) After compensation.

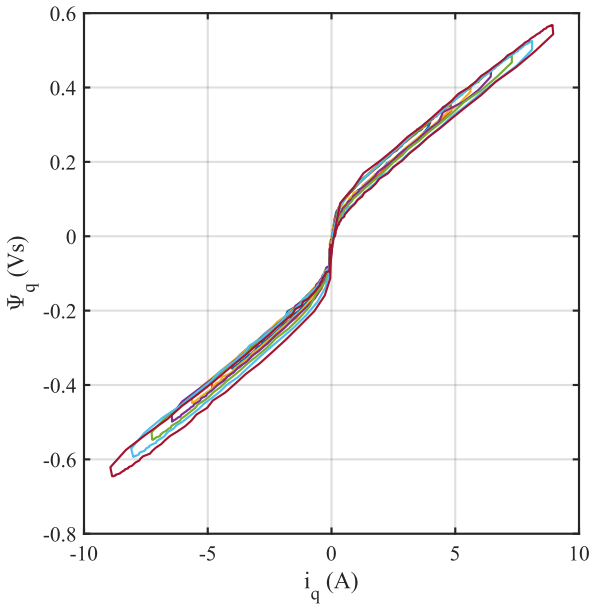

Figure 3.32: Experimental q-axis flux map obtained using the proposed self-commissioning method.

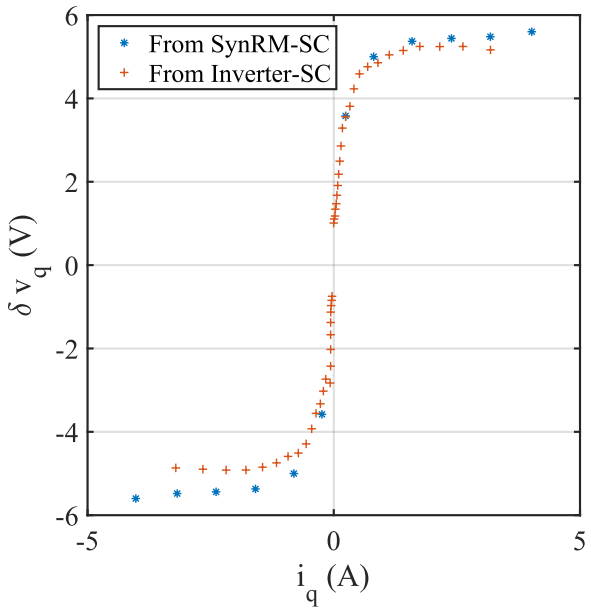

Figure 3.33: Experimental comparison of estimated voltage drop in the q-axis with inverter self-commissioning results.

Table 3.2: Quantitative comparison between the HFSI method and the proposed method relative to the bipolar method for d and q-axes flux maps.

Method	d-**Axis** (Wb)			q-**Axis** (Wb)		
	MAE	**RMSE**	**MaxError**	**MAE**	**RMSE**	**MaxError**
HFSI	0.1120	0.1265	0.1896	0.0548	0.0591	0.1069
Proposed	0.0447	0.0531	0.1189	0.0284	0.0299	0.0447

across datasets from the three methods. It provides sufficient flexibility to capture the nonlinearity and saturation behavior observed in the experimental flux data, which improves the precision of the comparison. While the selected model does not enforce the expected odd symmetry $\Psi_{d,q}(-i_{d,q}) = -\Psi_{d,q}(i_{d,q})$, this was considered acceptable for the purpose of model fitting and method comparison rather than physical interpretation.

The model fitted to the flux data extracted from the bipolar voltage excitation method is illustrated in Figure 3.34, and the corresponding algebraic model is provided within the figure. Similarly, the model fitted to the flux extracted from the proposed method is illustrated in Figure 3.35, with the associated algebraic expression shown in the figure. Visually, it is evident that the selected algebraic model adequately describes the relationship between flux and current.

Finally, as shown in Figure 3.36, the output of the proposed method is compared with those of the two other methods to validate the new procedure. It can be concluded that the proposed method, with its more precise post-processing such as outlier removal, serves as a viable alternative to the other approaches. In addition, it can simultaneously identify the machine's stator resistance, flux map, and inverter nonlinearity at standstill.

Based on the experimental findings, the bipolar method was chosen as the reference for comparison due to its demonstrated reliability in capturing accurate flux linkage characteristics across both the d- and q-axes. This method provides consistent flux mapping, as evident from the experimental results, with balanced performance across the entire current range. While it does exhibit moderate hysteresis, the bipolar

method effectively captures nonlinear magnetic effects, making it a robust benchmark for evaluating other methods. Its ability to maintain convergence under diverse operating conditions further underscores its suitability as a reference.

Quantitative analysis of the results in Table 3.2 highlights the superior performance of the proposed three-level voltage excitation method compared to the HFSI method. For the d-axis flux map, the proposed method demonstrates significantly lower errors relative to the bipolar approach, with a Mean Absolute Error (MAE) of $0.0447\,Wb$ and a Root Mean Square Error (RMSE) of $0.0531\,Wb$, compared to $0.1120\,Wb$ (MAE) and $0.1265\,Wb$ (RMSE) for the HFSI method. Additionally, the maximum error for the proposed method in the d-axis ($0.1189\,Wb$) is markedly smaller than that of the HFSI method ($0.1896\,Wb$), underscoring its accuracy and robustness under extreme operating conditions.

Similarly, for the q-axis flux map, the proposed method achieves a MAE of $0.0284\,Wb$ and a RMSE of $0.0299\,Wb$, outperforming the HFSI method, which recorded $0.0548\,Wb$ (MAE) and $0.0591\,Wb$ (RMSE). The maximum error for the proposed method in the q-axis ($0.0447\,Wb$) is also considerably lower than that of the HFSI method ($0.1069\,Wb$), further emphasizing its accuracy.

These findings demonstrate the limitations of the HFSI method, which, despite producing clean flux maps without hysteresis, struggles to achieve the same level of accuracy as the proposed method, particularly in the d-axis, where flux estimation is critical for precise torque control. In contrast, the proposed method achieves closer alignment with the bipolar reference, ensuring higher accuracy, reduced errors, and enhanced robustness. This improved performance makes the proposed method a more reliable and efficient choice for motor control applications, particularly in scenarios that demand high precision and stability. Thus, the experimental results underscore the advantages of the proposed method over established techniques, positioning it as a promising solution for self-commissioning flux map generation in SynRMs.

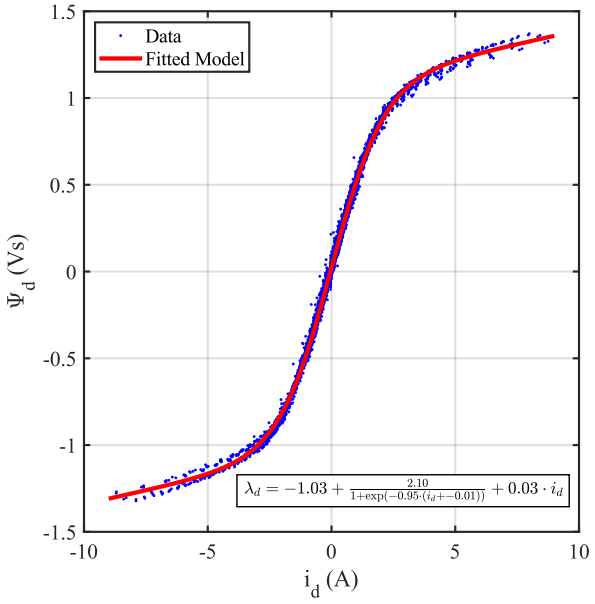

(a)

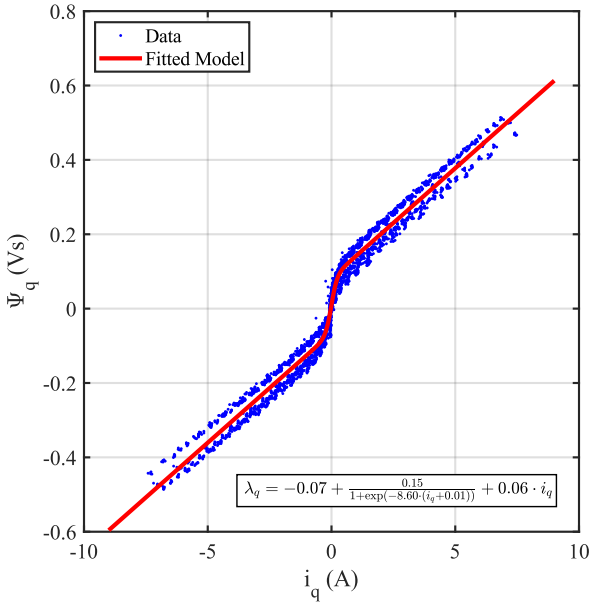

(b)

Figure 3.34: Algebraic model fitted to the flux map obtained by the bipolar excitation method: (a) *D*-axis fitted model, (b) *Q*-axis fitted model.

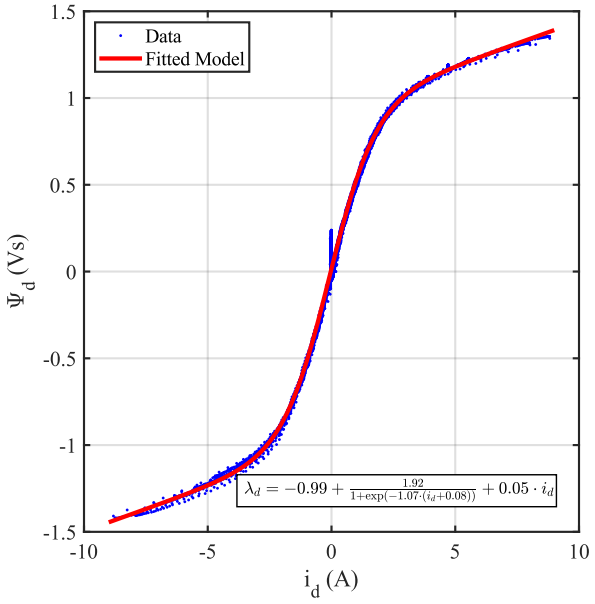

(a)

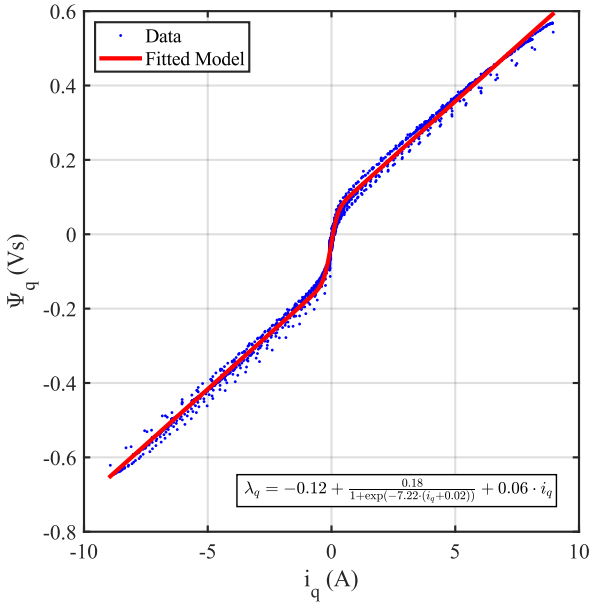

(b)

Figure 3.35: Algebraic model fitted to the flux map obtained by the proposed method: (a) *D*-axis fitted model, (b) *Q*-axis fitted model.

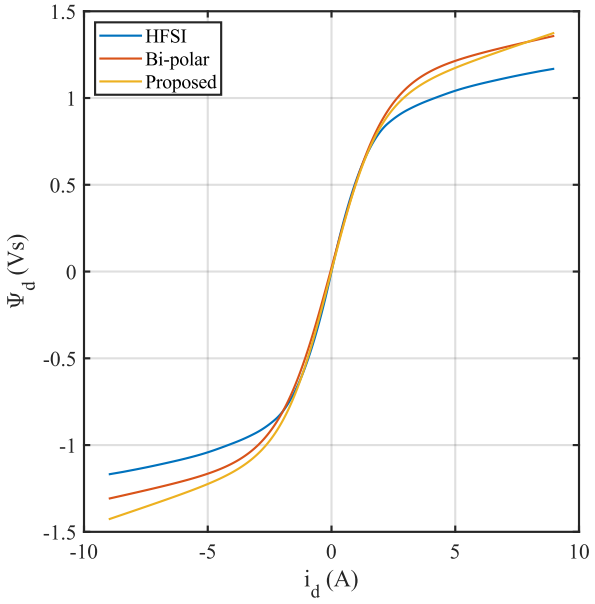

(a)

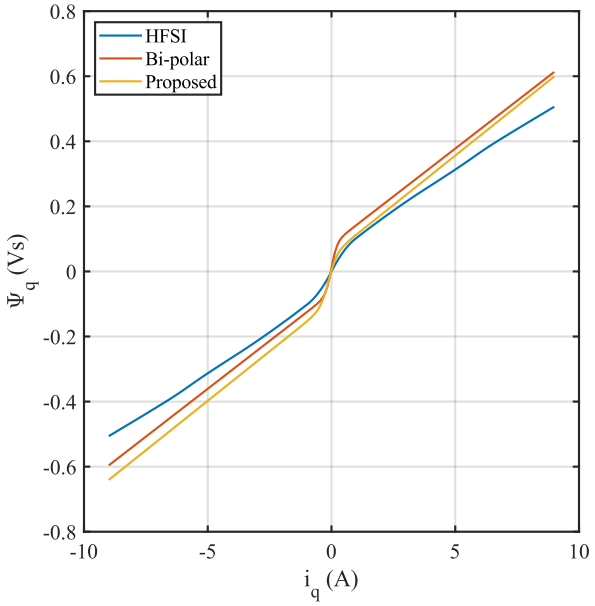

(b)

Figure 3.36: Comparison of experimental results obtained by the three different methods: (a) *D*-axis flux, (b) *Q*-axis flux.

3.7 Chapter Summary

This chapter has explored the procedures for flux map self-commissioning of SynRMs, focusing on two established methods and a newly proposed approach. The high-frequency signal injection method and the bipolar voltage excitation method were reviewed in detail, highlighting their operational principles and effectiveness in obtaining accurate flux maps. To address the limitations of these methods, a novel three-level voltage excitation method was proposed. This innovative approach facilitates flux map self-commissioning at standstill conditions while simultaneously estimating critical parameters such as stator resistance and inverter voltage drops, ensuring a more comprehensive and efficient characterization process.

The proposed method, alongside the two existing methods, was rigorously tested through simulations to analyze and compare their performance under various conditions. The simulation results provided valuable insights into the strengths and weaknesses of each method, paving the way for further refinement and validation. Subsequently, all three methods were experimentally implemented to assess their real-world applicability and effectiveness. These experiments offered a detailed comparison, showcasing the performance of the proposed three-level voltage excitation method relative to the established techniques. The findings underline the advantages of the proposed method, particularly in terms of precision, efficiency, and ease of implementation, establishing it as a promising alternative for flux map self-commissioning in SynRMs.

Chapter 4

PLL-Based Observer

4.1 State of the Art

Sensor-less control of SynRMs is critical for improving reliability and reducing costs in drive applications. Observer-based methods are widely employed to estimate rotor position and speed, enabling effective control and eliminating the need for physical sensors. The Phase-Locked Loop (PLL) is a fundamental technique embedded within various observers to enhance speed and position estimation in sensor-less control and drive systems. By integrating PLLs into observers such as sliding mode [60, 61, 62], Kalman filters [63, 64], extended Luenberger observers [65, 66], adaptive-based observers [67], high-frequency signal injection-based observers [68], and injection-less observers [69], these systems utilize the robust synchronization of the PLLs to track the position and speed of the motor shaft.

This combination allows for accurate estimation of rotor speed and position without the need for physical sensors, thereby reducing system complexity, cost, and maintenance requirements. The ability of the PLL to dynamically adapt and lock onto signal variations ensures precision even under challenging conditions, such as low-speed operation, transient loads, or electrical parameters variation. This approach not only enhances control performance but also improves efficiency and reliability in applications such as electric vehicles, robotics, and industrial drives, where precise

motor control is critical.

In addition to the conventional PLL approach [70], numerous extended and enhanced versions have been developed. For instance, [71] introduces a robust PLL method designed to handle amplitude fluctuations in resolver excitation signals. In [72], a Type-III PLL utilizing Chebyshev filters is proposed. The integration of the PLL with recursive least squares is explored in [73], while PLLs featuring speed-loop compensation structures are presented in [74]. A universal, parameter-independent PLL offering disturbance rejection is proposed in [75]. A novel quadrature PLL-based estimation scheme is described in [76], although it demonstrates sensitivity to disturbances.

A new PLL scheme was introduced to address speed reversal issues in sensorless PMSM drives, effectively enhancing reliability during such operations [77]. Another innovative approach employs a dual-PLL structure to mitigate harmonic effects in back electromotive force, significantly improving estimation accuracy and stability in IPMSM systems [78]. Furthermore, a PLL design integrated with a sliding mode observer has been proposed to suppress position estimation errors, demonstrating robust performance in sensorless IPMSM control [79]. Similarly, an enhanced PLL-based strategy has been developed to improve low-speed operation by estimating cross-coupling factors, resulting in better control and estimation accuracy [80]. Additionally, a second-order PLL-based speed estimator for induction motor drives has been designed to accurately detect the rotor flux vector phase angle, thereby enhancing the overall reliability of sensorless drives [81]. These advancements highlight the critical role of PLL innovations in refining observer-based sensorless control systems.

In this chapter, the proposed PLL, previously introduced as a contribution in a conference paper [82], is revisited and explained. It was implemented in software and connected to a custom-designed resolver-to-digital interface for motor shaft position and speed estimation.

4.2 PLL in the Context of an Observer

In the context of sensorless control, a PLL is often used as part of an observer to estimate rotor position and speed. The PLL mechanism is well-suited for dynamic systems because it tracks rotor position by locking onto the estimated angle derived from the flux or back-EMF vector in the $\alpha\beta$ stationary frame. By aligning a reference frame with the flux vector, the PLL continuously adjusts its phase to match that of the rotating field. This approach provides accurate position estimation even during variable-speed operation and in the presence of parameter uncertainties, using the ability of the PLL to minimize phase error and stabilize the observer. It processes the α- and β-axis components of back-EMF or flux, typically represented as sinusoidal $(\sin)$ and cosinusoidal $(\cos)$ signals, to track the phase and frequency of the rotor. The mathematical representation of the PLL method is as follows:

The α- and β-axis signals represent the components of the back-EMF or flux:

$$\begin{cases} x_\alpha(t) & = A\sin(\theta) \\ x_\beta(t) & = A\cos(\theta) \end{cases} \tag{4.1}$$

where A is the amplitude of the signal, which is typically normalized before being applied to the PLL to simplify phase detection, and θ is the input phase. However, it is important to note that at low speeds, the signal amplitude may become very small, resulting in a low signal-to-noise ratio. In such cases, normalization can amplify noise relative to the signal, potentially degrading PLL performance. To mitigate this, low-speed enhancements such as high-frequency signal injection or adaptive gain scaling are often integrated into sensorless control schemes to maintain reliable phase tracking [83, 84].

The PLL computes the phase error between the input phase θ and the estimated phase $\hat{\theta}$ generated by the observer. This is done using the following trigonometric relationship:

$$e(t) = x_\alpha(t)\cos(\hat{\theta}) - x_\beta(t)\sin(\hat{\theta}). \tag{4.2}$$

Substituting from (4.1), the phase detector output becomes:

$$e(t) = A\sin(\theta)\cos(\hat{\theta}) - A\cos(\theta)\sin(\hat{\theta}). \tag{4.3}$$

Using the sine difference identity, $\sin(a-b) = \sin(a)\cos(b) - \cos(a)\sin(b)$, this simplifies to:

$$e(t) = A\sin(\theta - \hat{\theta}), \tag{4.4}$$

where $(\theta - \hat{\theta})$ is the phase error.

The phase error signal, $e(t)$, is processed by a loop filter, usually a proportional-integral controller in conventional PLL structures, as shown in Figure 4.1, to generate the control signal, that adjusts the estimated phase. The loop filter is characterized by its transfer function $H(s)$:

$$\hat{\Omega}(s) = H(s)E(s), \tag{4.5}$$

where $\hat{\Omega}(s)$ and $E(s)$ are the Laplace transforms of $\hat{\omega}(t)$ and $e(t)$, respectively.

Finally, the estimated position is extracted as:

$$\hat{\theta}(t) = \int \hat{\omega}(t)\,dt. \tag{4.6}$$

To design the conventional PLL parameters, the proportional and integral gains are typically selected based on the desired bandwidth and dynamic response of the following second order system:

$$\frac{\hat{\theta}}{\theta} = \frac{k_p s + k_i}{s^2 + k_p s + k_i} \tag{4.7}$$

After matching its characteristic equation to the standard form, the parameters can be tuned easily:

$$s^2 + 2\zeta\omega_n s + \omega_n^2 \quad \Rightarrow \quad \begin{cases} k_p = 2\zeta\omega_n \\ k_i = \omega_n^2 \end{cases} \tag{4.8}$$

where ζ and ω_n are the damping ratio and natural frequency respectively, that should be selected according to the desired system response.

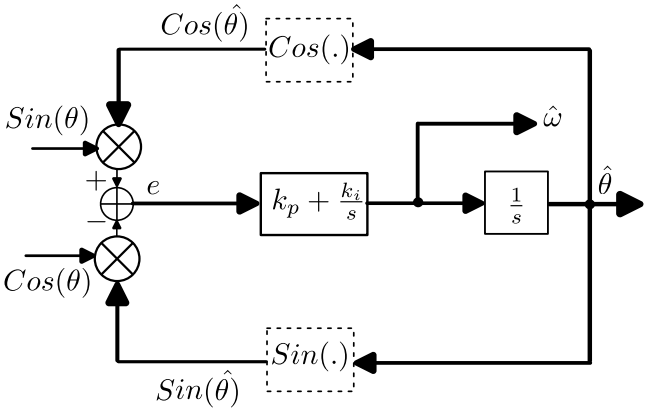

Figure 4.1: Conventional PLL block diagram. Reprinted from [82] with permission. © 2023 IEEE.

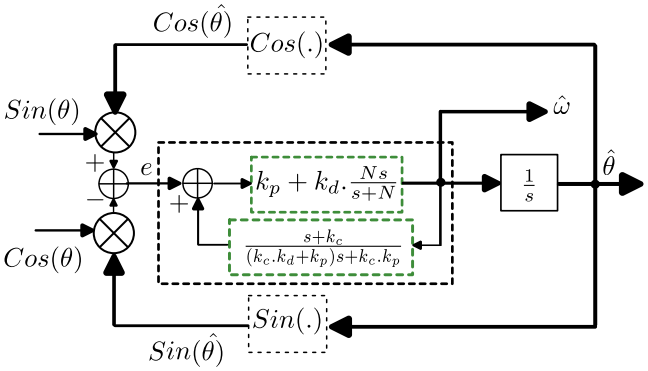

Figure 4.2: Proposed PLL block diagram. Reprinted from [82] with permission. © 2023 IEEE.

4.3 Proposed PLL-Based Observer

To enhance the dynamics of the conventional PLL, a novel compensated PLL-type observer has been proposed [82], as illustrated in Figure 4.2. This design is based on the structure presented in [74] and incorporates a PD controller instead of the PI controller typically used in conventional PLL-type observers. The inclusion of an inner-loop compensation results in a Type-III PLL, as described below:

$$\frac{\hat{\theta}}{\theta} = \frac{a(s^2 + (\lambda_1 + \lambda_2)s + \lambda_1\lambda_2))}{s^3 + as^2 + a(\lambda_1 + \lambda_2)s + a\lambda_1\lambda_2} \tag{4.9}$$

and the error transfer function is:

$$\frac{e}{\theta} = \frac{s^3}{s^3 + as^2 + a(\lambda_1 + \lambda_2)s + a\lambda_1\lambda_2} \tag{4.10}$$

where,

$$\begin{cases} a = \dfrac{(k_c k_d + k_p)(Nk_d + k_p)}{k_d(k_c - N)} \\ \lambda_1 + \lambda_2 = \dfrac{(k_c k_p^2 + Nk_p^2 + 2Nk_c k_p k_d)}{(k_c k_d + k_p)(Nk_d + k_p)} \\ \lambda_1\lambda_2 = \dfrac{Nk_c k_p^2}{(k_c k_d + k_p)(Nk_d + k_p)} \end{cases} \tag{4.11}$$

where k_p, k_d and N are the parameters of the inner loop PD controller, and k_c is a new parameter added to the compensation part of the proposed PLL. These parameters should be designed based on stability criteria, the final value theorem, and the system's bandwidth requirements. To ensure a stable closed-loop system, the Routh-Hurwitz stability criterion dictates that $k_c > N$ must be satisfied, along with the following additional condition:

$$a^2(\lambda_1 + \lambda_2) - a(\lambda_1\lambda_2) > 0 \tag{4.12}$$

Since the transfer functions and analysis are based on a linearized model of the PLL, the system dynamics are simplified, making design and stability evaluation

more straightforward. According to (4.9) and the block diagram shown in Figure 4.2, the open-loop transfer function can be derived as:

$$\frac{a(s+\lambda_1)(s+\lambda_2)}{s^3} \tag{4.13}$$

To guarantee stability and attain the desired bandwidth, the values of a, λ_1 and λ_2 must be determined for the closed-loop system with unity feedback gain. Subsequently, the four main parameters are numerically calculated using (4.11) to satisfy the previously outlined conditions.

4.4 Simulation Analysis

Time Domain Analysis

To evaluate the performance of the proposed method depicted in Figure 4.2 against the conventional approach shown in Figure 4.1, a simulation test was conducted. For the proposed method, the parameters were set as $[k_p, k_d, k_c, N] = [350, 50, 600, 10.5]$, whereas the conventional method used $[k_p, k_i] = [892.25, 10]$, ensuring an equivalent bandwidth for both the proposed method without compensation and the conventional approach.

The results in Fig. 4.3b indicate that the proposed PLL achieves rapid and precise position tracking during both acceleration and steady-speed phases, maintaining zero steady-state error. Conversely, the conventional method struggles with accurate position tracking during acceleration and exhibits steady-state error during the constant-speed phase.

Furthermore, Fig. 4.4b and Fig. 4.4c highlight the speed tracking performance. The proposed method demonstrates faster convergence to the actual speed, reduced overshoot, and zero steady-state error, clearly outperforming the conventional approach.

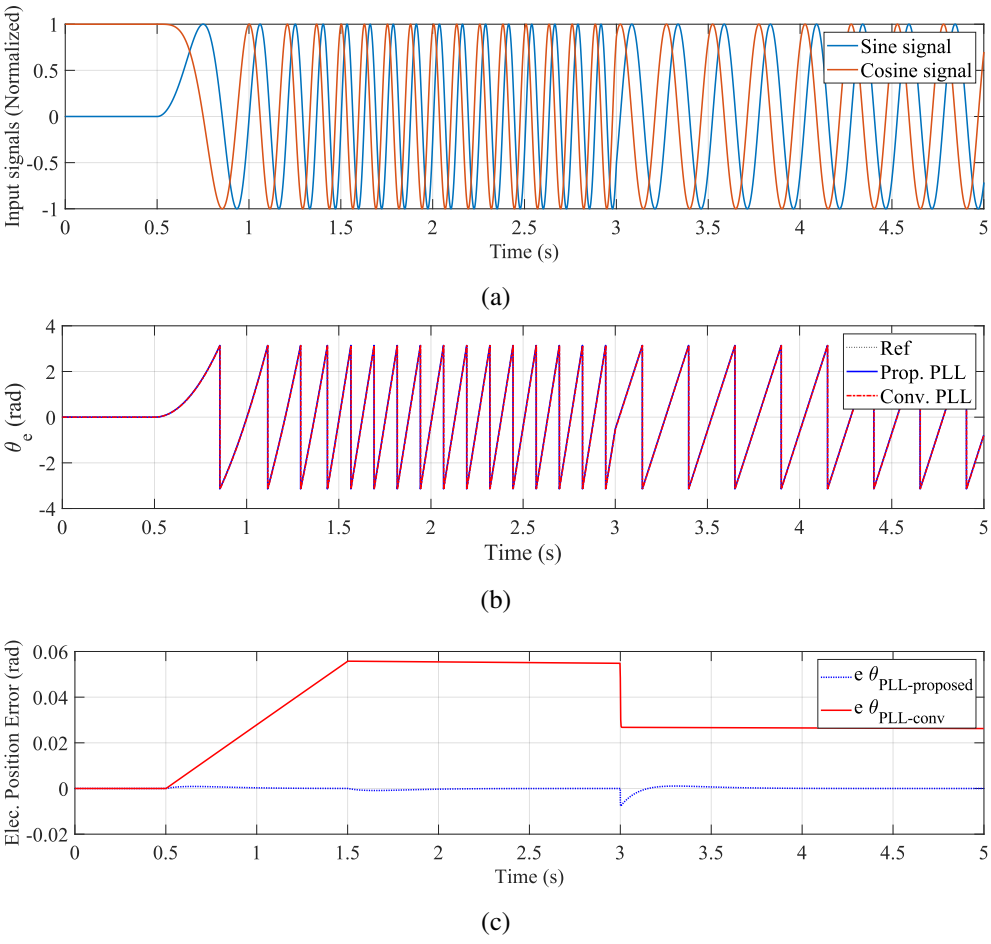

Figure 4.3: (a) PLL input signals, (b) Position tracking comparison between the conventional and the proposed PLL in simulation, (c) Error between real and estimated position using conventional and proposed PLL in simulation.

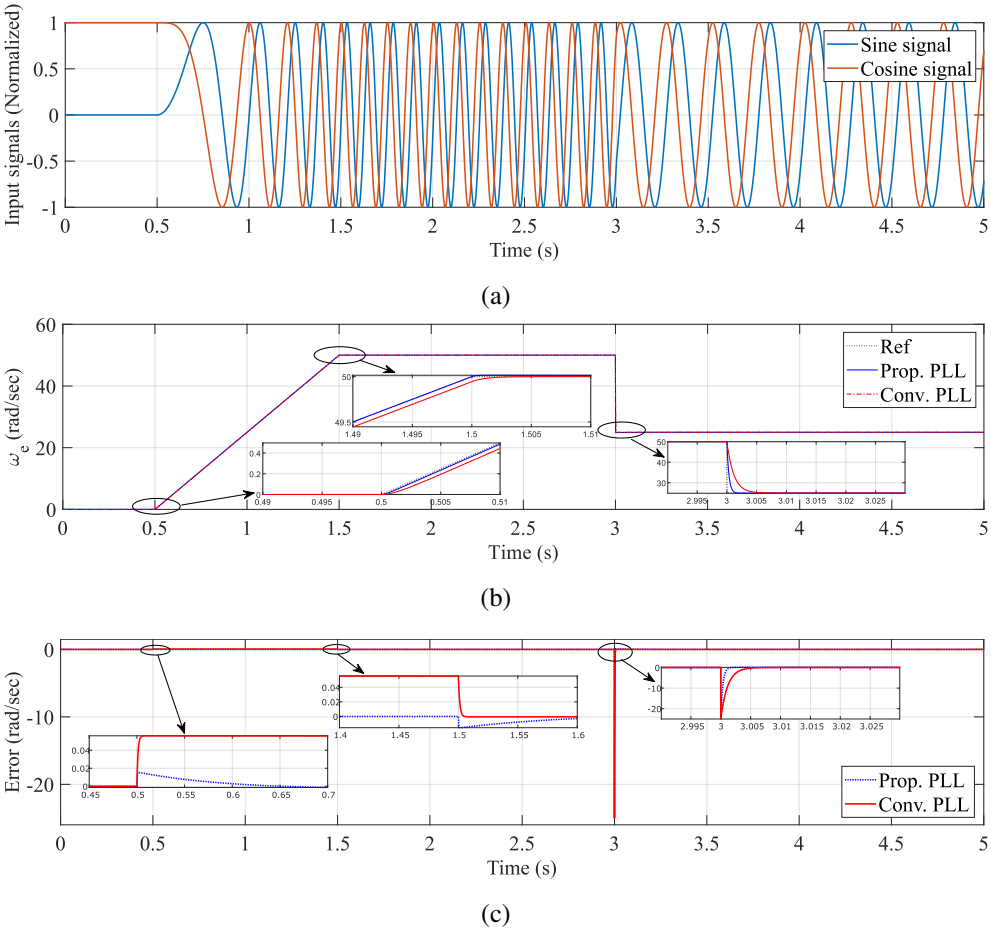

Figure 4.4: (a) PLL input signals, (b) Speed tracking comparison between the conventional and the proposed PLL in simulation, (c) Error between real and estimated speed using the conventional and the proposed PLL in simulation.

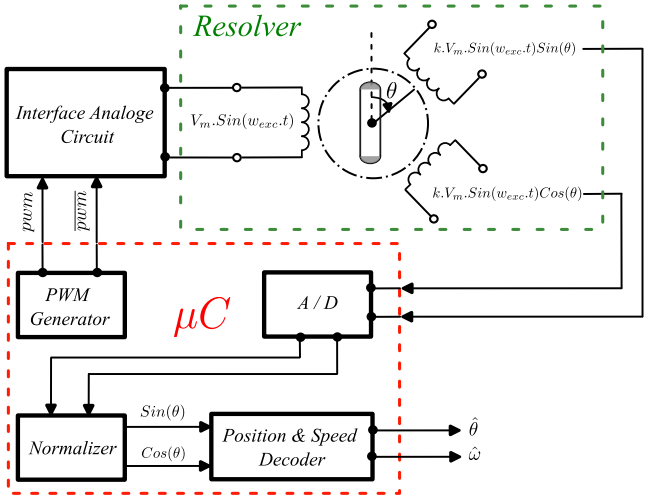

Figure 4.5: Resolver sensor typical topology. Reprinted from [82] with permission. © 2023 IEEE.

4.5 Experimental Result and Analysis

To thoroughly assess the performance of the proposed PLL, it was implemented within the closed-loop control system of a PMSM using a resolver sensor. Considering that the outputs of the resolver sensor are two orthogonal sinusoidal signals, as illustrated in Figure 4.5, it serves as a suitable reference for evaluating the proposed PLL. The same parameter set used during the simulation phase was adopted in the experimental setup to ensure consistency in the evaluation.

The experimental results, as presented in Figure 4.6, reveal that the estimated position derived from the proposed PLL accurately tracks the actual position measured by the resolver sensor. This alignment confirms the reliability of the PLL in real-world applications, demonstrating its capability to provide precise position estimation.

Additionally, Figure 4.7 illustrates the system's response under both acceleration and constant-speed conditions. The reference speed was applied in both scenarios, and the motor shaft exhibited excellent tracking of both speed and position. The sys-

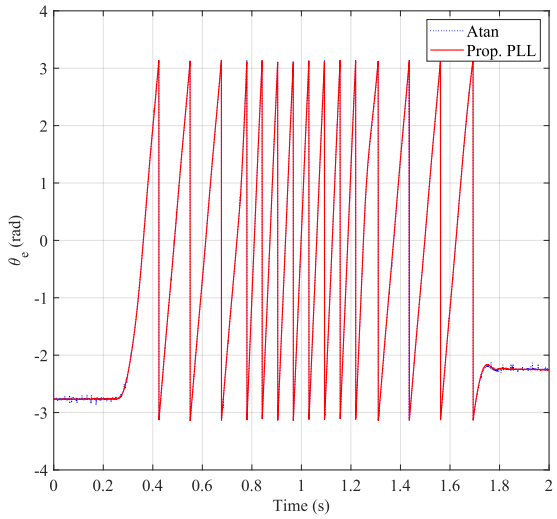

Figure 4.6: Estimated position from experimental results using the proposed PLL in closed-loop motor speed control. The blue dotted line represents the position calculated using the $atan2(x_\beta, x_\alpha)$ function, which determines the angle based on the ratio of two orthogonal components. The red solid line represents the position estimated using the proposed PLL method. Reprinted from [82] with permission. © 2023 IEEE.

tem achieved a rapid dynamic response, effectively adapting to changes in speed while maintaining a negligible steady-state error. These results validate the robustness and accuracy of the proposed PLL in achieving seamless integration and operation within an AC machine control framework, further highlighting its potential for high-performance motor drive applications.

4.6 Chapter Summary

This chapter highlighted the importance of combining observers with PLLs in sensorless motor control systems. Conventional PLL structures were reviewed, and their roles within observer frameworks for speed and position estimation in motor drives

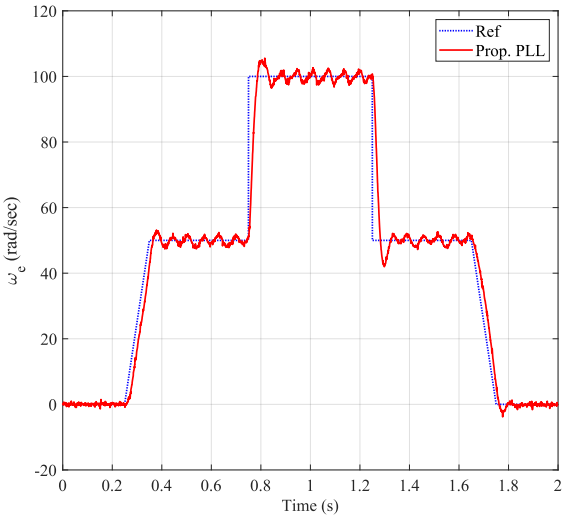

Figure 4.7: Estimated speed from experimental result using proposed PLL in closed-loop motor speed control. Reprinted from [82] with permission. © 2023 IEEE.

were discussed. A novel fast-dynamic PLL with compensation was proposed to enhance system performance. Simulations demonstrated its superiority over conventional designs in terms of dynamic response and accuracy. Finally, the proposed PLL was evaluated using orthogonal signals from a resolver sensor in a closed-loop PMSM control system, confirming its effectiveness in accurate speed and position estimation.

Chapter 5

Conclusion and Future Work

Conclusion

This research has conducted an in-depth investigation into the development of self-commissioning and estimation techniques for sustainable synchronous reluctance motor drives in industrial applications. The motivation for this research was the necessity of an energy-efficient and cost-effective solution in electric motor drives. By taking into account the SynRM technology as an alternative to IMs and PMSMs, we tried to bridge the gaps among energy efficiency, system robustness, and cost-effectiveness.

One of the primary achievements of this work is the development of robust self-commissioning algorithms appropriate for three-phase two-level inverters and SynRMs. These algorithms address critical challenges such as inverter nonlinearity, voltage drop compensation and SynRM parameter estimation. Another contribution is the integration of a phase-locked loop based observer, which provides precise sensorless operation by accurately estimating rotor position and flux. This capability is crucial for reducing dependency on mechanical sensors, thus enhancing the reliability and cost-effectiveness of the drive system.

The experimental results presented in this thesis demonstrate the practical applicability and performance of the proposed methodologies. The self-commissioning

techniques simplify the commissioning process, providing plug-and-play functionality, which is especially valuable in industrial environments where ease of deployment is essential. Moreover, the study highlights the synergy between the proposed algorithms and SynRM technology, demonstrating notable reductions in energy consumption and improvements in overall system efficiency. These achievements underscore the potential of SynRM drives as a viable alternative to traditional induction motors and permanent magnet synchronous motors.

Furthermore, this research deepens the understanding of inverter nonlinearities and their impact on drive performance, particularly in the context of SynRM systems. While inverter nonlinearity has been addressed in prior studies, this work provides a detailed and validated analytical model useful for self-commissioning at standstill. The developed framework enables more accurate compensation during commissioning, contributing to improved drive performance. The insights gained from this study can support further refinement of control and identification techniques, offering a practical foundation for future advancements in sensorless motor drive systems.

The contributions of this research are aligned with the broader goals of sustainable industrial development. By utilizing the advantages of SynRMs, such as their high efficiency, robustness, and lack of reliance on rare-earth materials, this work supports the transition towards greener and more sustainable industrial practices.

Future Work

While this research has addressed several critical challenges in SynRM drive technology, there remain opportunities for further exploration and improvement:

1. **Advanced Voltage Drop Model of Inverter**: Considering the fact that the output parasitic capacitance of the switching devices are not constant, but assumed fixed in this study, the investigation of a more advanced model based on physical characteristics remains an open research problem.

2. **Expansion of the Proposed SynRM Self-commissioning Method**: In the proposed self-commissioning method, the cross saturation has not been regarded. Improving the proposed method in a way that it could extract the flux and inductance

cross saturation could increase the accuracy and efficiency in machine control and it is an open topic for researchers.

3. **Integration with Emerging Technologies**: Investigating the integration of SynRM drives with renewable energy systems, such as wind and solar power, could provide new opportunities for sustainable energy solutions. Additionally, exploring hybrid systems that combine SynRMs with advanced energy storage technologies could lead to innovative applications.

4. **Scalability and High-Power Applications**: Extending the proposed methods to high-power and multi-level inverter topologies could expand the applicability of SynRM drives to more demanding industrial applications. Addressing challenges related to scalability and efficiency in these contexts would be a valuable direction for future work.

5. **Motor Design Optimization**: Collaborative research between motor design and control system experts could lead to optimized SynRM geometries that complement the proposed control strategies. This could result in even greater efficiency and performance improvements.

In conclusion, this thesis lays a strong foundation for advancing SynRM drive technology, addressing key challenges, and demonstrating the viability of these systems in industrial applications. Considering the methodologies developed in this study, future research can further enhance the efficiency, reliability, and sustainability of SynRM drives, contributing to a more energy-efficient and environmentally friendly industrial landscape.

Appendix A

Matlab Codes

- Function for inverter output voltage range in (2.13) to (2.17):

```
function [v_max,v_min] = range_v(Inr,SwH,SwL,ix)
vdc = Inr.Vdc;
if (ix>0)
    vd_on = SwL.vd_on;
    vt_on = SwH.vt_on;
    rd_on = SwL.rd_on;
    rt_on = SwH.rt_on;
    v_max = vdc - (vt_on + rt_on * abs(ix));
    v_min = - (vd_on + rd_on * abs(ix));
elseif (ix<0)
    vd_on = SwH.vd_on;
    vt_on = SwL.vt_on;
    rd_on = SwH.rd_on;
    rt_on = SwL.rt_on;
    v_max = vdc + (vd_on + rd_on * abs(ix));
    v_min = vt_on + rt_on * abs(ix);
else
    v_max = 0;
    v_min = 0;
end
```

- Function for inverter output capacitance charging time in (2.23) to (2.25):

```
function t_cap = cap_t(Inr,SwH,SwL,ix)
vdc = Inr.Vdc;
ch_out = SwH.Cout;
cl_out = SwL.Cout;
if (ix>0)
    vd_on = SwL.vd_on;
    vt_on = SwH.vt_on;
    rd_on = SwL.rd_on;
    rt_on = SwH.rt_on;
    t_cap = (ch_out + cl_out) * (rd_on - rt_on + ...
        (vdc - vt_on + vd_on)/abs(ix));
elseif (ix<0)
    vd_on = SwH.vd_on;
    vt_on = SwL.vt_on;
    rd_on = SwH.rd_on;
    rt_on = SwL.rt_on;
    t_cap = (ch_out + cl_out) * (rd_on - rt_on + ...
        (vdc + vd_on - vt_on)/abs(ix));
else
    t_cap = 0;
end
```

- Function for capacitance voltage drop region in (2.22) and (2.24):

```
function F = v_pn(Inr,v_mx,v_mn,tc,ix)
td = Inr.td;
ton = Inr.ton;
toff = Inr.toff;
if (ix > 0 )
    if(tc < td - toff)
    F = 0.5 * (v_mx - v_mn) * tc + v_mn * (td - toff);
    else
    F = 0.5 * (2 * (td - toff) * v_mx - (td - toff) ...
        * (td - toff) * (v_mx - v_mn)/tc);
```

```
10          end
11      elseif (ix < 0)
12      if(tc < td - ton)
13          F = -0.5 * (v_mx - v_mn) * tc + v_mx * (td - ton);
14          else
15          F = 0.5 * (2 * (td - ton) * v_mn + (td - ton) * ...
                (td - ton) * (v_mx - v_mn)/tc);
16          end
17      else
18      F = 0;
19      end
```

- Function for critical current calculation in (2.26):

```
1       function [I_cr_p , I_cr_n] = curr_cr(Inr,SwL,SwH)
2       vdc = Inr.Vdc;
3       td = Inr.td;
4       ton = Inr.ton;
5       toff = Inr.toff;
6       I_cr_p = ((vdc - SwH.vt_on + SwL.vd_on)*(SwH.Cout + ...
            SwL.Cout))/((td-toff)-(SwL.rd_on - ...
            SwH.rt_on)*(SwH.Cout + SwL.Cout));
7       I_cr_n = -((vdc - SwL.vt_on + SwH.vd_on)*(SwH.Cout + ...
            SwL.Cout))/((td-ton)-(SwH.rd_on - ...
            SwL.rt_on)*(SwH.Cout + SwL.Cout));
8       end
```

- Function for real output calculation in (2.20) and (2.21):

```
1       function v_real_xg = v_real(Inr,v_mx,v_mn,ix,F,D_on)
2       td = Inr.td;
3       tsw = Inr.Tsw;
4       ton = Inr.ton;
5       toff = Inr.toff;
6       T_on = D_on * tsw;
7       if (ix>0)
```

```
8           v_real_xg = ((T_on - td - ton + toff) * (v_mx - ...
                v_mn) + tsw * v_mn - (td - toff) * v_mn + ...
                F)/tsw;
9       elseif (ix<0)
10          v_real_xg = ((T_on + td - ton + toff) * (v_mx - ...
                v_mn) + tsw * v_mn - (td - ton) * v_mx + F)/tsw;
11      else
12          v_real_xg = 0;
13      end
14      end
```

- Goertzel algorithm:

```
1       function [R, L , v_amp, I_amp] = ...
            goertzel_RL(voltage_signal, current_signal, fs, ...
            freq)
2
3       V = goertzel_single_freq(voltage_signal, fs, freq)/fs;
4
5       v_amp = sqrt(real(V)^2 + imag(V)^2);
6
7       I = goertzel_single_freq(current_signal, fs, freq)/fs;
8
9       I_amp = sqrt(real(I)^2 + imag(I)^2);
10
11      Z = V / I;
12
13      omega = 2 * pi * freq;
14
15      R = real(Z);
16      L = imag(Z) / omega;
17      end
18
19      function X = goertzel_single_freq(signal, fs, freq)
20      N = length(signal);
21
22      k = round((N * freq) / fs);
```

```
23
24      w = 2 * pi * k / N;
25      coeff = 2 * cos(w);
26
27      s_prev = 0;
28      s_prev2 = 0;
29
30      for n = 1:N
31      s = signal(n) + coeff * s_prev - s_prev2;
32      s_prev2 = s_prev;
33      s_prev = s;
34      end
35
36      real_part = (s_prev - s_prev2 * cos(w));
37      imag_part = (s_prev2 * sin(w));
38
39      X = real_part + 1i * imag_part;
40
41      end
```

Bibliography

[1] ABB. Achieving the Paris Agreement: The Vital Role of High-Efficiency Motors and Drives in Reducing Energy Consumption. *ABB White Paper*, 2021. Available: https://new.abb.com/.

[2] Stephen J. Chapman. *Electric Machinery Fundamentals*. McGraw-Hill, New York, 5th edition, 2011.

[3] P. C. Krause, O. Wasynczuk, and S. D. Sudhoff. *Analysis of Electric Machinery and Drive Systems*. IEEE Press, Piscataway, NJ, 2nd edition, 2002.

[4] International Energy Agency. Energy efficiency report. *IEA Report*, 2021. Available: https://www.iea.org/reports/energy-efficiency-2021.

[5] Aldo Boglietti and Michele Pastorelli. Induction and synchronous reluctance motors comparison. In *2008 34th Annual Conference of IEEE Industrial Electronics*, pages 2041–2044, 2008. doi:10.1109/IECON.2008.4758270.

[6] Yang Yang, Qiang He, Chunyun Fu, Shuiping Liao, and Peng Tan. Efficiency improvement of permanent magnet synchronous motor for electric vehicles. *Energy*, 213:118859, 2020. URL: https://www.sciencedirect.com/science/article/pii/S0360544220319666, doi:10.1016/j.energy.2020.118859.

[7] Ayman M. EL-Refaie. Fractional-slot concentrated-windings synchronous permanent magnet machines: Opportunities and challenges. *IEEE Transactions on*

Industrial Electronics, 57(1):107–121, 2010. doi:10.1109/TIE.2009.2030211.

[8] Jin-Woo Ahn and Grace Firsta Lukman. Switched reluctance motor: Research trends and overview. *CES Transactions on Electrical Machines and Systems*, 2(4):339–347, 2018. doi:10.30941/CESTEMS.2018.00043.

[9] Christopher Donaghy-Spargo. Synchronous reluctance motor technology: industrial opportunities, challenges and future direction. *Engineering & Technology Reference*, 2016. doi:10.1049/etr.2015.0044.

[10] Gianmario Pellegrino, Thomas M. Jahns, Nicola Bianchi, Wen L. Soong, and Francesco Cupertino. *The Rediscovery of Synchronous Reluctance and Ferrite Permanent Magnet Motors: Tutorial Course Notes*. Springer, Cham, Switzerland, 2016. doi:10.1007/978-3-319-32202-5.

[11] Mukhammed Murataliyev, Michele Degano, Mauro Di Nardo, Nicola Bianchi, and Chris Gerada. Synchronous reluctance machines: A comprehensive review and technology comparison. *Proceedings of the IEEE*, 110(3):382–399, 2022. doi:10.1109/JPROC.2022.3145662.

[12] ABB Group. Improving end-to-end system efficiency with synchronous reluctance motors. Technical report, ABB, 2021. URL: https://www.energyefficiencymovement.com/wp-content/uploads/2021/09/ABB_WhitePaper_Improving-end-to-end-system-efficiency-2.pdf.

[13] International Energy Agency (IEA). Energy efficiency 2022. *IEA Energy Efficiency Reports*, 2022. URL: https://www.iea.org/reports/energy-efficiency-2022.

[14] A. Vagati, M. Pastorelli, and G. Franceschini. High performance control of synchronous reluctance motor. In *IAS '96. Conference Record of the 1996 IEEE Industry Applications Conference Thirty-First IAS Annual Meeting*, volume 1, pages 295–303 vol.1, 1996. doi:10.1109/IAS.1996.557035.

[15] Seyyed Mohammad Seyyedzadeh and Abbas Shoulaie. Accurate modeling of the nonlinear characteristic of a voltage source inverter for better performance in near zero currents. *IEEE Transactions on Industrial Electronics*, 66(1):71–78, 2019. doi:10.1109/TIE.2018.2823692.

[16] Eric Armando, Radu Iustin Bojoi, Paolo Guglielmi, Gianmario Pellegrino, and Michele Pastorelli. Experimental identification of the magnetic model of synchronous machines. *IEEE Transactions on Industry Applications*, 49(5):2116–2125, 2013. doi:10.1109/TIA.2013.2258876.

[17] Vasyl Varvolik, Shuo Wang, Dmytro Prystupa, Giampaolo Buticchi, Sergei Peresada, Michael Galea, and Serhiy Bozhko. Fast experimental magnetic model identification for synchronous reluctance motor drives. *Energies*, 15(6), 2022. URL: https://www.mdpi.com/1996-1073/15/6/2207, doi:10.3390/en15062207.

[18] Anantaram Varatharajan, Gianmario Pellegrino, and Eric Armando. Self-commissioning of synchronous reluctance motor drives: Magnetic model identification with online adaptation. In *2020 IEEE Energy Conversion Congress and Exposition (ECCE)*, pages 5353–5360, 2020. doi:10.1109/ECCE44975.2020.9236307.

[19] Mattia Morandin and Silverio Bolognani. Locked rotor characterization tests of ipm/rel synchronous machine for sensorless drives. In *8th IET International Conference on Power Electronics, Machines and Drives (PEMD 2016)*, pages 1–6, 2016. doi:10.1049/cp.2016.0352.

[20] Texas Instruments. *InstaSPIN-BLDC Sensorless Motor Control Solution*. Texas Instruments, 2013. Available at: https://www.ti.com/tool/INSTASPIN-BLDC.

[21] Massimiliano Biason, Sandro Calligaro, Mattia Iurich, Roberto Petrella, and Amir Shahdadi. Advances on analysis, modeling and accurate self-commissioning compensation of inverter dead-time distortion based on a physi-

cal model. In *2021 IEEE Energy Conversion Congress and Exposition (ECCE)*, pages 4788–4795, 2021. doi:10.1109/ECCE47101.2021.9594922.

[22] Gendrin Martin and Serhan Kantay. Dead-time compensation based on a physical model with online self-commissioning procedure based on an extended kalman filter. In *2024 Energy Conversion Congress & Expo Europe (ECCE Europe)*, pages 1–7, 2024. doi:10.1109/ECCEEurope62508.2024.10752030.

[23] Shafiq Odhano, Mi Tang, Andrea Formentini, Pericle Zanchetta, and Radu Bojoi. Identification of linear permanent magnet synchronous motor parameters and inverter non-linearity effects. In *2018 International Symposium on Power Electronics, Electrical Drives, Automation and Motion (SPEEDAM)*, pages 26–32, 2018. doi:10.1109/SPEEDAM.2018.8445214.

[24] S. Bolognani and M. Zigliotto. Self-commissioning compensation of inverter non-idealities for sensorless ac drives applications. In *2002 International Conference on Power Electronics, Machines and Drives (Conf. Publ. No. 487)*, pages 30–37, 2002. doi:10.1049/cp:20020085.

[25] Vincenzo Barba, Salvatore Musumeci, Fausto Stella, Fabio Mandrile, and Marco Palma. Investigation of dead time losses in inverter switching leg operation: Gan fet vs. mosfet comparison. *Energies*, 17(15), 2024. URL: https://www.mdpi.com/1996-1073/17/15/3855, doi:10.3390/en17153855.

[26] Zhendong Zhang and Longya Xu. Dead-time compensation of inverters considering snubber and parasitic capacitance. *IEEE Transactions on Power Electronics*, 29(6):3179–3187, 2014. doi:10.1109/TPEL.2013.2275551.

[27] Paisak Poolphaka, Ehsan Jamshidpour, Thierry Lubin, Lotfi Baghli, and Noureddine Takorabet. Comparative study of igbt and sic mosfet three-phase inverter: Impact of parasitic capacitance on the output voltage distortion. *Ac-*

tuators, 12(9), 2023. URL: https://www.mdpi.com/2076-0825/12/9/355, doi:10.3390/act12090355.

[28] I. R. Bojoi, E. Armando, G. Pellegrino, and S. G. Rosu. Self-commissioning of inverter nonlinear effects in ac drives. In *2012 IEEE International Energy Conference and Exhibition (ENERGYCON)*, pages 213–218, 2012. doi:10.1109/EnergyCon.2012.6347755.

[29] Guoxiang Zhou, Bangji Wang, Kunhui Xu, and Qingxiang Liu. An inverter nonlinearity compensation method for pmsm drives based on dead-time elimination. In *2023 26th International Conference on Electrical Machines and Systems (ICEMS)*, pages 662–667, 2023. doi:10.1109/ICEMS59686.2023.10345223.

[30] Hyeon-Sik Kim, Yong-Cheol Kwon, Seung-Jun Chee, and Seung-Ki Sul. Analysis and compensation of inverter nonlinearity for three-level t-type inverters. *IEEE Transactions on Power Electronics*, 32(6):4970–4980, 2017. doi:10.1109/TPEL.2016.2607226.

[31] Tian Yang, Yongting Deng, Hongwen Li, and Jianli Wang. Super-twisting resonant controller-based inverter nonlinearity compensation for permanent magnet synchronous motor drive system. *Control Engineering Practice*, 140:105665, 2023. doi:10.1016/j.conengprac.2023.105665.

[32] Vasyl Varvolik, Dmytro Prystupa, Giampaolo Buticchi, Sergei Peresada, Michael Galea, and Serhiy Bozhko. Inverter nonlinearity effects on self-commissioning of synchronous reluctance drives. In *2021 24th International Conference on Electrical Machines and Systems (ICEMS)*, pages 1792–1797, 2021. doi:10.23919/ICEMS52562.2021.9634484.

[33] Nicola Bedetti, Sandro Calligaro, and Roberto Petrella. Self-commissioning of inverter dead-time compensation by multiple linear regression based on a physical model. In *2014 IEEE Energy Conversion Congress and Exposition (ECCE)*, pages 242–249, 2014. doi:10.1109/ECCE.2014.6953400.

[34] Gianmario Pellegrino, Paolo Guglielmi, Eric Armando, and Radu Iustin Bojoi. Self-commissioning algorithm for inverter nonlinearity compensation in sensorless induction motor drives. *IEEE Transactions on Industry Applications*, 46(4):1416–1424, 2010. doi:10.1109/TIA.2010.2049554.

[35] Gianmario Pellegrino, Radu Iustin Bojoi, Paolo Guglielmi, and Francesco Cupertino. Accurate inverter error compensation and related self-commissioning scheme in sensorless induction motor drives. *IEEE Transactions on Industry Applications*, 46(5):1970–1978, 2010. doi:10.1109/TIA.2010.2057395.

[36] Silverio Bolognani, Luca Peretti, and Mauro Zigliotto. Repetitive-control-based self-commissioning procedure for inverter nonidealities compensation. *IEEE Transactions on Industry Applications*, 44(5):1587–1596, 2008. doi:10.1109/TIA.2008.2002280.

[37] Simon Wiedemann and Christoph Michael Hackl. Simultaneous identification of inverter and machine nonlinearities for self-commissioning of electrical synchronous machine drives. *IEEE Transactions on Energy Conversion*, 38(3):1767–1780, 2023. doi:10.1109/TEC.2023.3263353.

[38] Zhiwei Chen, Tingna Shi, Yanfei Cao, Chen Li, and Yan Yan. An accurate inverter nonlinearity compensation method for ipmsm torque estimation based on numerical fitting. *IEEE Journal of Emerging and Selected Topics in Power Electronics*, 11(2):2126–2138, 2023. doi:10.1109/JESTPE.2022.3227939.

[39] Guangxu Lu, Guijie Yang, Jianyong Su, and Fengyang Liu. Current injection-based vsi nonlinearity self-learning method for dual three-phase pmsm drives considering the effect of zero-axis voltage. In *2023 IEEE Energy Conversion Congress and Exposition (ECCE)*, pages 5297–5302, 2023. doi:10.1109/ECCE53617.2023.10362368.

[40] Anton Dianov and Alecksey Anuchin. Offline measurement of stator resistance and inverter voltage drop using least squares. *IEEE Access*, 11:17053–17065, 2023. doi:10.1109/ACCESS.2023.3245663.

[41] Seyyed Mohammad Seyyedzadeh, Sobhan Mohamadian, Mohsen Siami, and Abbas Shoulaie. Modeling of the nonlinear characteristics of voltage source inverters for motor self-commissioning. *IEEE Transactions on Power Electronics*, 34(12):12154–12164, 2019. doi:10.1109/TPEL.2019.2909141.

[42] Marko Hinkkanen, Paolo Pescetto, Eemeli Mölsä, Seppo E. Saarakkala, Gianmario Pellegrino, and Radu Bojoi. Sensorless self-commissioning of synchronous reluctance motors at standstill without rotor locking. *IEEE Transactions on Industry Applications*, 53(3):2120–2129, 2017. doi:10.1109/TIA.2016.2644624.

[43] Marko Hinkkanen, Paolo Pescetto, Eemeli Mölsä, Seppo E. Saarakkala, Gianmario Pellegrino, and Radu Bojoi. Sensorless self-commissioning of synchronous reluctance motors at standstill. In *2016 XXII International Conference on Electrical Machines (ICEM)*, pages 1174–1180, 2016. doi:10.1109/ICELMACH.2016.7732673.

[44] Luca Peretti, Paul Sandulescu, and Giovanni Zanuso. Self-commissioning of flux linkage curves of synchronous reluctance machines in quasi-standstill condition. *IET Electric Power Applications*, 9(9):642–651, 2015. doi:10.1049/iet-epa.2015.0070.

[45] Ludovico Ortombina, Nicola Bianchi, and Luigi Alberti. Standstill self-commissioning procedure for synchronous reluctance motors based on coenergy model. In *2023 IEEE International Electric Machines and Drives Conference (IEMDC)*, pages 1–6, 2023. doi:10.1109/IEMDC55163.2023.10238999.

[46] Kaiwen Tan, Jianyong Su, Guijie Yang, and Bencheng Zhong. Current injection-based self-commissioning of synchronous reluctance motor consid-

ering cross-saturation effect. In *IECON 2023- 49th Annual Conference of the IEEE Industrial Electronics Society*, pages 1–6, 2023. doi:10.1109/IECON51785.2023.10311800.

[47] Simon Wiedemann and Ralph M. Kennel. Encoderless self-commissioning and identification of synchronous reluctance machines at standstill. In *2017 IEEE 26th International Symposium on Industrial Electronics (ISIE)*, pages 296–302, 2017. doi:10.1109/ISIE.2017.8001263.

[48] Paolo Pescetto and Gianmario Pellegrino. Sensorless standstill commissioning of synchronous reluctance machines with automatic tuning. In *2017 IEEE International Electric Machines and Drives Conference (IEMDC)*, pages 1–8, 2017. doi:10.1109/IEMDC.2017.8002302.

[49] Anantaram Varatharajan, Gianmario Pellegrino, and Eric Armando. Self-commissioning of synchronous reluctance motor drives: Magnetic model identification with online adaptation. In *2020 IEEE Energy Conversion Congress and Exposition (ECCE)*, pages 5353–5360, 2020. doi:10.1109/ECCE44975.2020.9236307.

[50] Anantaram Varatharajan, Gianmario Pellegrino, and Eric Armando. Kinetic-rotor self-commissioning of synchronous machines for magnetic model identification with online adaptation. *IEEE Transactions on Industry Applications*, 58(3):3578–3588, 2022. doi:10.1109/TIA.2022.3151039.

[51] Phuoc Hoa Truong, Damien Flieller, Ngac Ky Nguyen, Nguyen Bao Anh, and Nguyen Duc Hung. Inductance identification of synchronous reluctance motors using capacitor discharge method. In *2019 International Symposium on Electrical and Electronics Engineering (ISEE)*, pages 1–4, 2019. doi:10.1109/ISEE2.2019.8920947.

[52] Chong Bao, Haodong Chen, Chenyi Yang, Jixi Zhong, Haotian Gao, and Shoujun Song. Synchronous reluctance motor flux linkage saturation modeling based

on stationary identification and neural networks. In *IECON 2022 – 48th Annual Conference of the IEEE Industrial Electronics Society*, pages 1–6, 2022. doi:10.1109/IECON49645.2022.9968452.

[53] Ludovico Ortombina, Dario Pasqualotto, Fabio Tinazzi, and Mauro Zigliotto. Magnetic model identification of synchronous motors considering speed and load transients. *IEEE Transactions on Industry Applications*, 56(5):4945–4954, 2020. doi:10.1109/TIA.2020.3003555.

[54] Vasyl Varvolik, Shuo Wang, Dmytro Prystupa, Giampaolo Buticchi, Sergei Peresada, Michael Galea, and Serhiy Bozhko. Fast experimental magnetic model identification for synchronous reluctance motor drives. *Energies*, 15(6), 2022. URL: https://www.mdpi.com/1996-1073/15/6/2207, doi:10.3390/en15062207.

[55] Bencheng Zhong, Jianyong Su, Guangxu Lu, Kaiwen Tan, and Guijie Yang. Self-commissioning of synchronous reluctance motor at standstill with inverter nonlinearity and resistance error compensation. *IEEE Transactions on Energy Conversion*, 39(3):1828–1839, 2024. doi:10.1109/TEC.2024.3376803.

[56] Andrea Credo, Francesco Parasiliti Collazzo, Marco Tursini, and Marco Villani. A unified approach for the commissioning of synchronous reluctance motor drives. *IEEE Transactions on Industry Applications*, 60(1):68–79, 2024. doi:10.1109/TIA.2023.3289789.

[57] Shafiq Ahmed Odhano, Radu Bojoi, Stefan George Rosu, and Alberto Tenconi. Identification of the magnetic model of permanent-magnet synchronous machines using dc-biased low-frequency ac signal injection. *IEEE Transactions on Industry Applications*, 51(4):3208–3215, 2015. doi:10.1109/TIA.2015.2413383.

[58] L. Peretti and M. Zigliotto. Automatic procedure for induction motor parameter estimation at standstill. *IET Electric Power Applica-*

tions, 6:214–224, 2012. URL: https://digital-library.theiet.org/doi/abs/10.1049/iet-epa.2010.0262, arXiv:https://digital-library.theiet.org/doi/pdf/10.1049/iet-epa.2010.0262, doi:10.1049/iet-epa.2010.0262.

[59] Nicola Bedetti, Sandro Calligaro, and Roberto Petrella. Stand-still self identification of flux characteristics for synrm using novel saturation approximating function and multiple linear regression. In *2015 IEEE Energy Conversion Congress and Exposition (ECCE)*, pages 2995–3002, 2015. doi:10.1109/ECCE.2015.7310079.

[60] Yong-Chao Liu, Salah Laghrouche, Abdoul N'Diaye, and Maurizio Cirrincione. Active-flux-based super-twisting sliding mode observer for sensorless vector control of synchronous reluctance motor drives. In *2018 7th International Conference on Renewable Energy Research and Applications (ICRERA)*, pages 1–7, 2018. doi:10.1109/ICRERA.2018.8566751.

[61] Jiaiun Lou, Gaolin Wang, Song Liang, Guoqiang Zhang, Yihua Hu, and Dianguo Xu. An improved sliding mode observer for position sensorless synchronous reluctance motor drives. In *2021 24th International Conference on Electrical Machines and Systems (ICEMS)*, pages 844–849, 2021. doi:10.23919/ICEMS52562.2021.9634580.

[62] Ertugrul Ates, Burak Tekgun, Gunyaz Ablay, and Murat Barut. Design and real-time implementation of a sliding mode observer utilizing voltage signal injection and pll for sensorless control of ipmsms. *Engineering Science and Technology, an International Journal*, 59:101873, 2024. URL: https://www.sciencedirect.com/science/article/pii/S2215098624002593, doi:10.1016/j.jestch.2024.101873.

[63] Jian Huang and Zhixun Ma. Sensorless control of synchronous reluctance machines based on improved kalman filter-phase locked loop. In *2023 26th International Conference on Electrical Machines and Systems (ICEMS)*, pages 4602–4605, 2023. doi:10.1109/ICEMS59686.2023.10344934.

[64] Ke Yu, Shihua Li, Wenwu Zhu, and Zuo Wang. Sensorless control scheme for pmsm drive via generalized proportional integral observers and kalman filter. *IEEE Transactions on Power Electronics*, pages 1–14, 2024. doi:10.1109/TPEL.2024.3502396.

[65] Cristian Lascu and Gheorghe-Daniel Andreescu. Pll position and speed observer with integrated current observer for sensorless pmsm drives. *IEEE Transactions on Industrial Electronics*, 67(7):5990–5999, 2020. doi:10.1109/TIE.2020.2972434.

[66] Lucas Rossato Rocha, Marcelo Back de Araujo, Eduardo Cattani Silva, Luis Henrique Ost Scher, César José Volpato Filho, and Rodrigo Padilha Vieira. Speed and position observer for non-sinusoidal pmsm based on a psd+pll structure. *Journal of Control, Automation and Electrical Systems*, 33(1):304–314, Feb 2022. doi:10.1007/s40313-021-00811-z.

[67] Anantaram Varatharajan and Gianmario Pellegrino. Sensorless synchronous reluctance motor drives: A general adaptive projection vector approach for position estimation. *IEEE Transactions on Industry Applications*, 56(2):1495–1504, 2020. doi:10.1109/TIA.2019.2961986.

[68] Ahmed Farhan, Mohamed Abdelrahem, Amr Saleh, Adel Shaltout, and Ralph Kennel. High-performance position sensorless control of reluctance synchronous motor using high-frequency injection. In *2019 IEEE 13th International Conference on Power Electronics and Drive Systems (PEDS)*, pages 1–6, 2019. doi:10.1109/PEDS44367.2019.8998897.

[69] Ludovico Ortombina, Fabio Bernardi, Luigi Alberti, and Davide Barater. Injectionless full range speed sensorless control for synchronous reluctance motors based on pwm current ripple. In *2023 IEEE Workshop on Electrical Machines Design, Control and Diagnosis (WEMDCD)*, pages 1–6, 2023. doi:10.1109/WEMDCD55819.2023.10110945.

[70] Jun-Di Sun, Guang-Zhong Cao, Su-Dan Huang, and Hong Qiu. Software-based resolver-to-digital converter using the pll tracking algorithm. In *2016 13th International Conference on Ubiquitous Robots and Ambient Intelligence (URAI)*, pages 719–723, 2016. doi:10.1109/URAI.2016.7734100.

[71] Lazhar Ben-Brahim and Mohieddine Benammar. A new PLL method for resolvers. In *The 2010 International Power Electronics Conference - ECCE ASIA*, pages 299–305, 2010. doi:10.1109/IPEC.2010.5542263.

[72] Huan Liu and Zhong Wu. Demodulation of Angular Position and Velocity from Resolver Signals via Chebyshev Filter-Based Type III Phase Locked Loop. *Electronics*, 7(12), 2018. doi:10.3390/electronics7120354.

[73] Moon Seok-Hwan, Kim Ji-Won, and Park Byung-Gun. Adaptive pll method using recursive least square algorithm. In *2015 IEEE International Conference on Industrial Technology (ICIT)*, pages 896–901, 2015. doi:10.1109/ICIT.2015.7125211.

[74] Haoye Qin and Zhong Wu. Angle Tracking Observer with Improved Accuracy for Resolver-to-Digital Conversion. *Symmetry*, 11(11), 2019. doi:10.3390/sym11111347.

[75] Georges el Murr, Damian Giaouris, and J. W. Finch. Universal pll strategy for sensorless speed and position estimation of pmsm. In *2008 IEEE Region 10 and the Third international Conference on Industrial and Information Systems*, pages 1–6, 2008. doi:10.1109/ICIINFS.2008.4798473.

[76] Shuo Chen, Xiang Wu, Junlei Chen, Guojun Tan, and Yifei Wang. Second-order lead compensator-based quadrature pll for sensorless interior permanent magnet synchronous motor control. *IET Power Electronics*, 13(3):568–575, 2020. doi:10.1049/iet-pel.2019.0822.

[77] C. Olivieri and M. Tursini. A novel pll scheme for a sensorless PMSM drive overcoming common speed reversal problems. In *International Symposium on*

Power Electronics Power Electronics, Electrical Drives, Automation and Motion, pages 1051–1056, 2012. doi:10.1109/SPEEDAM.2012.6264468.

[78] Yituo Li, Haifeng Lu, Wenlong Qu, and Shuang Sheng. A novel sensorless control method of ipmsm using dual pll structure. In *Proceedings of The 7th International Power Electronics and Motion Control Conference*, volume 2, pages 1216–1220, 2012. doi:10.1109/IPEMC.2012.6259009.

[79] Zhonggang Yin, Yanping Zhang, Xinping Cao, Dongsheng Yuan, and Jing Liu. Estimated position error suppression using novel pll for ipmsm sensorless drives based on full-order smo. *IEEE Transactions on Power Electronics*, 37(4):4463–4474, 2022. doi:10.1109/TPEL.2021.3125024.

[80] Yuhan Chen, John Xu, Jing Li, and Dunant Halim. An enhanced pll based sensorless control strategy for ipmsm with cross coupling factor estimation in low speed range. In *2023 26th International Conference on Electrical Machines and Systems (ICEMS)*, pages 4914–4919, 2023. doi:10.1109/ICEMS59686.2023.10344809.

[81] Prasun Mishra, Cristian Lascu, Michael Møller Bech, Bjørn Rannestad, and Stig Munk-Neilsen. Design and analysis of pll speed estimator for sensorless rotor-flux oriented control of induction motor drives. In *2021 IEEE Energy Conversion Congress and Exposition (ECCE)*, pages 4743–4747, 2021. doi:10.1109/ECCE47101.2021.9595316.

[82] Alex Musetti, Enrico Panciroli, Hossein Sadegh Lafmejani, and Alessandro Soldati. A high-efficiency resonant driver and soft decoder interface with fast-dynamics pll-type angle and speed tracking observer for resolvers. In *2023 IEEE Energy Conversion Congress and Exposition (ECCE)*, pages 5087–5092, 2023. doi:10.1109/ECCE53617.2023.10362295.

[83] Pascal Combes, François Malrait, Philippe Martin, and Pierre Rouchon. An analysis of the benefits of signal injection for low-speed sensorless control of induction motors. In *2016 International Symposium on Power Electronics,*

Electrical Drives, Automation and Motion (SPEEDAM), pages 721–727, 2016. doi:10.1109/SPEEDAM.2016.7525835.

[84] Al Kassem Jebai, Franois Malrait, Philippe Martin, and Pierre Rouchon. Signal injection and averaging for position estimation of permanent-magnet synchronous motors. In *2012 IEEE 51st IEEE Conference on Decision and Control (CDC)*, pages 7608–7613, 2012. doi:10.1109/CDC.2012.6426887.

Acknowledgements

First and foremost, I am deeply grateful to my wife for her unwavering love, patience, and encouragement throughout this journey. Her belief in my abilities has been a constant source of strength and inspiration. I also extend my heartfelt gratitude to my family, whose support and sacrifices have been pivotal in helping me achieve this milestone. Their confidence in my pursuits has been a cornerstone of my success.

I would like to sincerely thank the University of Parma, for providing the academic foundation and resources necessary to undertake this research. I am particularly indebted to my supervisor, Professor Alessandro Soldati, whose guidance, expertise, and mentorship have been invaluable throughout this project. I am also grateful to Aalto University, my hosting institution during my study abroad experience, and to my advisor there, Professor Marko Hinkkanen, for their hospitality and academic support, which enriched my learning and broadened my perspectives. Finally, I extend my thanks to the hosting company, Startec S.r.l., for offering practical insights and exposure that greatly contributed to the application-oriented aspects of this work.

La borsa di dottorato è stata cofinanziata con risorse del
Programma Operativo Nazionale Ricerca e Innovazione 2014-2020, risorse FSE REACT-EU
Azione IV.4 “Dottorati e contratti di ricerca su tematiche dell’innovazione”
e Azione IV.5 “Dottorati su tematiche Green”